CELAL BAYAR ÜNİVERSİTESİ
FEN BİLİMLERİ DERGİSİ

CELAL BAYAR UNIVERSITY
JOURNAL OF SCIENCE

CELAL BAYAR
ÜNİVERSİTESİ

Journal of Science

Volume: 16, Issue: 4, Year: 2020

"CBU Journal of Science is indexed by ULAKBIM-TUBITAK TR-DIZIN"

CBUJOS is published quarterly at Manisa Celal Bayar University Printing House

"CBU Journal of Science is a refereed scientific journal"

Celal Bayar University Journal of Science

CBU Journal of Science

Celal Bayar University Journal of Science (CBUJOS) covers scientific studies in the fields of Engineering and Science and publishes accounts of original research articles concerned with all aspects of experimental and theoretical studies. CBU Journal of Science is a refereed scientific journal published four times annually (March, June, September and December) by Institute of Natural and Applied Sciences of Manisa Celal Bayar University. CBU Journal of Science considers the original research articles written in English for evaluation.

CBU Journal of Science is indexed by TUBİTAK ULAKBIM TR-DIZIN, and also is included in DOAJ, Cite Factor, Journal TOCS, Advanced Science Index and OAJI databases. Digital Object Identifier (DOI) number will be assigned for all the articles being published in CBU Journal of Science.

Instructions for Authors and Article Template can be found on the main page of MCBU Institute of Natural and Applied Sciences (http://fbe.cbu.edu.tr)

Vol: 16, Issue: 4, Year: 2020

Contents

Celal Bayar University Journal of Science

High Isolation Wideband Multiple-Input Multiple-Output Antennas for Millimeter Wave Applications

Tayfun Okan[1]* iD

[1] Electrical and Electronics Engineering, University of Turkish Aeronautical Association, Ankara, Turkey
*tokan@thk.edu.tr
*Orcid: 0000-0002-9913-0803

Abstract

A planar 2×2 and 4×4 multiple-input multiple-output (MIMO) antennas are designed and analyzed in this study. The individual antenna elements that form the MIMO structure are located perpendicular to each other in order to facilitate polarization diversity. Except a notch band at 4.3 GHz, the 2×2 antenna nearly covers the entire 2.41-31.4 GHz frequency band. It is similar for the 4×4 antenna that has tri-band characteristic, where the impedance bandwidth ($|S_{11}| \leq -10$ dB) values are determined as 1.4, 10.05 and 16.26 GHz. Beside these high bandwidth results, both MIMO antennas have perfect isolation characteristic which is important to prevent coupling in MIMO systems. The proposed MIMO antennas are convenient to be used in all S (2-4 GHz), C (4-8 GHz), X (8-12 GHz), Ku (12-18 GHz) and K-bands (18-27 GHz). Furthermore, omnidirectional radiation patterns are observed at the resonance frequencies, and the reported 2×2 and 4×4 antennas have compact sizes of 80×40×1 mm^3 (64.5λ×32.25λ ×0.8λ) and 80×80×1 mm^3 (64.5λ×64.5λ ×0.8λ), respectively.

Keywords: Millimeter wave, monopole antenna, multiple-input multiple-output (MIMO).

1. Introduction

With the continuously developing technology, there is a high demand to monopole antennas because of their ease of fabrication, small size and wide bandwidth. Therefore, monopole antennas are used frequently in a variety of millimeter wave applications. For instance, they are used inside human body as a biocompatible implanted antenna operating at industrial, scientific and medical (ISM) band [1, 2]. They are also used with many wireless communication systems like 5G technology [3, 4], wireless local area network (WLAN) [5], wireless fidelity (wi-fi) applications [6, 7], vehicular applications [8], satellite communication systems and even with wearable antennas [9, 10]. Furthermore; when the need to a wide impedance bandwidth arises, monopole antennas are still considered to be implemented in ultra-wideband (UWB) [11, 12] and super wideband (SWB) [13] antenna designs. In [14], a nona-band loop monopole antenna is reported to be used for mobile handset. The bandwidth and directivity of a monopole antenna is enhanced with the help of a magnetic metamaterial slab used over the ground plane in [15]; whereas, the directivity is improved with a left-handed medium metamaterial unit cell in [16]. Another monopole antenna is presented in [17], where signal

interference technique and circular disk designed antenna are employed to form a filtering antenna structure.

Multiple-input multiple-output (MIMO) antennas have many advantages like offering a high data rate and high quality of service (QoS), reducing bit error rate (BER) and supporting large number of subscribers. Therefore, combining MIMO technology with UWB or SWB antenna designs ensure a further improvement in the quality and performance [18]. A wideband MIMO antenna is designed in [4] to be used for the future mobile devices operating in the 5G technology. MIMO antennas are used for base station applications as well [19], where the presented tri-band multi polarized MIMO antenna is reported to have a resonance at 28/38/48 GHz frequencies. It is important to note that in most of the former MIMO antenna studies, the MIMO design is generally created by positioning the individual antennas perpendicular to each other to facilitate polarization diversity. In [20], MIMO antennas are compared with directional slot and conventional slot antenna designs. The MIMO antennas proposed in [21, 22] operate at around 3.5 GHz and 5.5 GHz wireless communication systems, respectively. A 2×2 MIMO antenna is developed in [23] with coplanar waveguide

technique, where the antenna is designed to operate at both 3.5 and 5.5 GHz frequencies. As seen from the abovementioned studies, MIMO antennas are frequently employed for wireless communication systems [24, 25] thanks to their high data rate feature.

In our previous study [13], a SWB antenna that operates between 2.59 to 31.14 GHz frequency band with a reflection coefficient of $|S_{11}| \leq -10$ dB was designed. The reported antenna had a bandwidth of 28.55 GHz and fractal bandwidth of 169%. Moreover, it had a compact size with the dimensions of $40 \times 40 \times 1$ mm^3. The single element radiation characteristics were proposed by analyzing the parameters like return loss, realized gain, radiation efficiency, far-field radiation pattern and surface current distribution. Successful results were obtained when compared with other state-of-arts for the designed SWB antenna.

Using MIMO technology with wideband monopole antennas yields further enhancements in the speed of data transfer. Hence, the reported SWB antenna in our previous study is combined with MIMO technology in this study. A 2×2 and a 4×4 MIMO versions of the design are tested with CST Microwave Studio, a computer-based simulation program; where the reflection coefficient, isolation, diversity gain (DG) and envelope correlation coefficient (ECC) parameters of the proposed MIMO antennas are analyzed. It is observed that in the frequency range from 2.41 GHz to 31.4 GHz, the 2×2 and 4×4 MIMO antennas have dual-band and tri-band characteristics, respectively. Besides that, the wide bandwidth feature of the antenna is well maintained and both of the proposed MIMO antenna designs exhibit high isolation performance. Another importance of this study is that, an improvement is achieved in data rate and QoS, thanks to multipath property of the MIMO structure.

2. Antenna Design

A 2×2 and 4×4 MIMO antennas are analyzed in this study that consist of 2 layers as seen in Fig. 1. An octagonal shaped radiator is used for wide bandwidth. The radiator and microstrip transmission line are shifted to the left from the center part, in order to increase the impedance bandwidth. The width and length of the feeding line is determined to match the 50 Ω characteristic impedance. A stub is inserted to the right top of the radiator, and a small sized notch is introduced to the ground plane to further improve the bandwidth. The location of the notch is determined as to be on the projection of the transmission line. Rogers RT5880 substrate with a loss tangent of 0.0009 and a permittivity of 2.2 is used with a thickness of 1 mm. The bright and dark parts seen in Fig. 1, represents the substrate and copper parts of the antenna, respectively. MIMO designs are formed by positioning the antenna elements orthogonal to each other. Moreover, copper

thickness is used as 0.035 mm and the parameters of the proposed antenna is given in Table 1. The overall dimensions of the proposed 2×2 and 4×4 MIMO antenna designs are $80 \times 40 \times 1$ mm^3 ($64.5\lambda \times 32.25\lambda \times 0.8\lambda$) and $80 \times 80 \times 1$ mm^3 ($64.5\lambda \times 64.5\lambda \times 0.8\lambda$) respectively, where λ is the wavelength for the smallest operating frequency. Therefore, W_1, W_2 and L_1 are 80 mm, L_1 has a value of 40 mm.
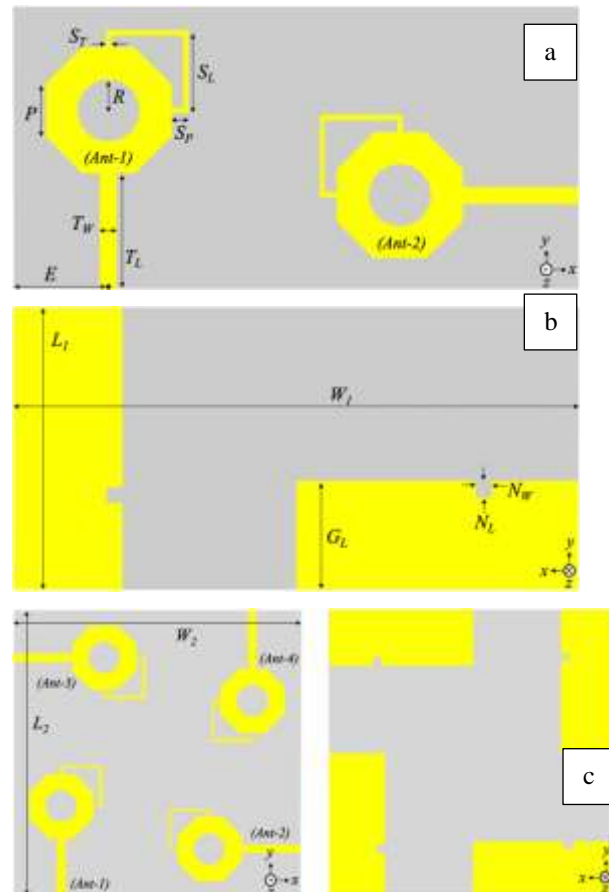
Figure 1. The geometry of the proposed MIMO antenna (a) top view of the 2×2 version (b) bottom view of the 2×2 version (c) top and bottom view of the 4×4 version.

Table 1. Parameters of the proposed MIMO antennas.

Parameters	S_L	S_T	S_P	P
Value (mm)	11.65	0.65	2.38	7.35
Parameters	G_L	N_L	N_W	T_L
Value (mm)	15.42	2.34	2.27	16.41
Parameters	T_W	R	E	
Value (mm)	2.37	4.43	13.34	

3. Results and Discussion

The performance of 2×2 and 4×4 antenna structures are analyzed and interpreted under this title by using the results obtained from CST Microwave Studio. S-parameters versus frequency graph of the 2×2 antenna is

depicted in Fig.2(a), whereas the VSWR graph is plotted in Fig.2(b). As seen from Fig.2(a), the simulated return loss results of both of the antenna elements (S_{11}, S_{22}) in 2×2 design align well with each other. As the return loss curves rise above the -10 dB at 4.3 GHz, the antenna elements have dual band between 2.41-31.4 GHz interval. The impedance bandwidth ($|S_{11}| \leq -10$ dB) of 2×2 antenna is 1.69 GHz (2.41-4.1 GHz) and 26.85 GHz (4.55-31.4 GHz), respectively. It is also possible to say that the 2×2 MIMO antenna has an operating bandwidth from 2.41 GHz to 31.4 GHz excluding 4.3 GHz notch band. When the insertion loss (S_{12}, S_{21}) analysis is performed, it is seen that the values are kept below -25 dB through the operating frequency range. This means that, the isolation between the antenna elements are successfully provided. The success in providing a good impedance matching for the designed antenna is also measured by analyzing VSWR values; since VSWR is dependent on the reflection coefficient (Γ) with the formula of $VSWR = \frac{1+|\Gamma|}{1-|\Gamma|}$. As seen from Fig. 2(b), VSWR values are kept below 2 in the entire simulated frequency range.

Same analyses are made for the 4×4 design, as seen from Fig. 3. The four return loss and VSWR curves of each antenna element are overlapping, which proves that each element performs the same characteristic. This design has three separate bands in the operating frequency range, the bandwidths of which are determined as 1.4 GHz (2.41-3.81 GHz), 10.05 GHz (4.78-14.83 GHz) and 16.26 GHz (15.24-31.5 GHz), respectively. Furthermore, the insertion loss values are almost always below -20 dB. As this design has multiple bands, the VSWR value at 4.3 GHz rises above 2 as seen in Fig. 3(b). The bandwidth values of 2×2 and 4×4 antennas are given in Table 2, where they are compared with our previous single element antenna design [13]. One can say that, as the number of antenna elements increases in the MIMO structure, the bandwidth of the antennas decreases and the number of bands appearing in the operating range increases. On the other hand, the isolation between the antenna elements are well maintained in both 2×2 and 4×4 MIMO antenna designs.

(a)

(a)

(b)

(b)

Figure 2. (a) The return loss and insertion loss graph, (b) VSWR graph of 2×2 MIMO antenna.
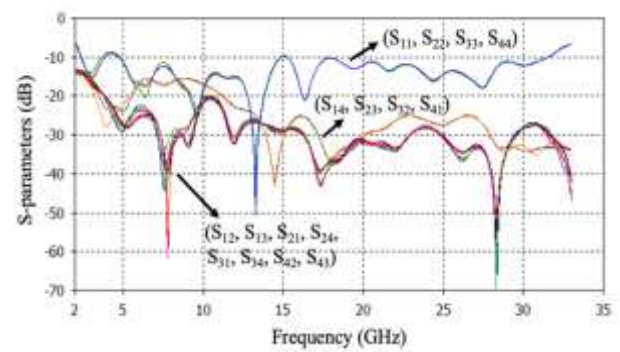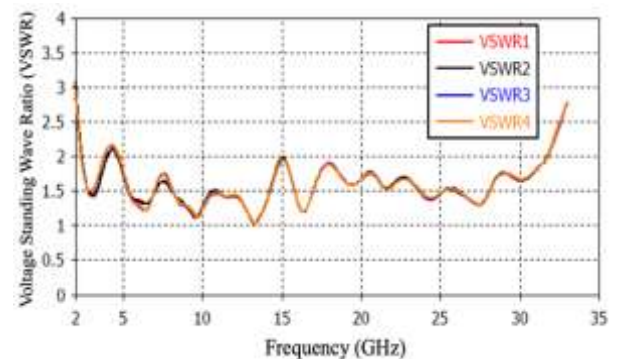
Figure 3. (a) The return loss and insertion loss graph, (b) VSWR graph of 4×4 MIMO antenna.

Table 2. Parameters of the proposed MIMO antennas.

Design	BW-1	BW-2	BW-3
Single antenna element [13]	28.55 GHz (2.59-31.14 GHz)	-	-
2×2	1.69 GHz (2.41-4.1 GHz)	26.85 GHz (4.55-31.4 GHz)	-
4×4	1.4 GHz (2.41-3.81 GHz)	10.05 GHz (4.78-14.83 GHz)	16.26 GHz (15.24-31.5 GHz)

* BW-i: i*th* bandwidth.

The vectoral surface current distribution of the MIMO antennas are shown in Fig. 4. As seen from the figure, Ant-1 is the excited element for both 2×2 and 4×4 structures. The simulations are performed at 13.3 GHz, since both structures have a resonance frequency at 13.3 GHz. The surface currents are concentrated mainly at the edge of the feeding line and they also seem to be denser at the stub located on the top right corner of the radiator patch. Both 2×2 and 4×4 structures are nearly in the same current distribution form, as they are both measured at 13.3 GHz.

Radiation pattern is another important antenna property that defines the radiation behavior of the antenna [26]. The far field radiation patterns of 2×2 and 4×4 structures are depicted in polar form in Fig. 5. The simulations for *E* (xz-plane) and *H* (yz-plane) planes are performed at 13.3 GHz resonance frequency and it is observed that both MIMO antennas have omni-directional radiation characteristic.

Diversity gain (DG) and envelope correlation coefficient (ECC) are other parameters that need to be examined to analyze the performance of MIMO antennas. The numerical expressions of ECC and CG are given in Eq. (3.1) and (3.2), respectively. As seen from Eq. (3.1), the ECC value at a certain frequency is dependent on the return loss and insertion loss values at that frequency. The ideal value of ECC is expected to be 0.1 or less and it is expected to be higher than 9.5 for DG. As seen from Fig. 6(a), both MIMO antennas have an ECC value below 0.01; and even between 4.5 GHz to 31 GHz it is below 0.001, which is a very successful result. This shows that the antennas that form the MIMO structure are independent of each other. It is important to emphasize that positioning the antenna elements perpendicular to each other has an effect on this low ECC value. Same successful results are obtained for DG as seen in Fig. 6(b), which is higher than 9.995 in the operating frequency range.

$$ECC = \frac{|S_{11}^* S_{12} + S_{21}^* S_{22}|^2}{(1-(|S_{11}|^2+|S_{21}|^2))(1-(|S_{22}|^2+|S_{12}|^2))} \quad \textbf{(3.1)}$$
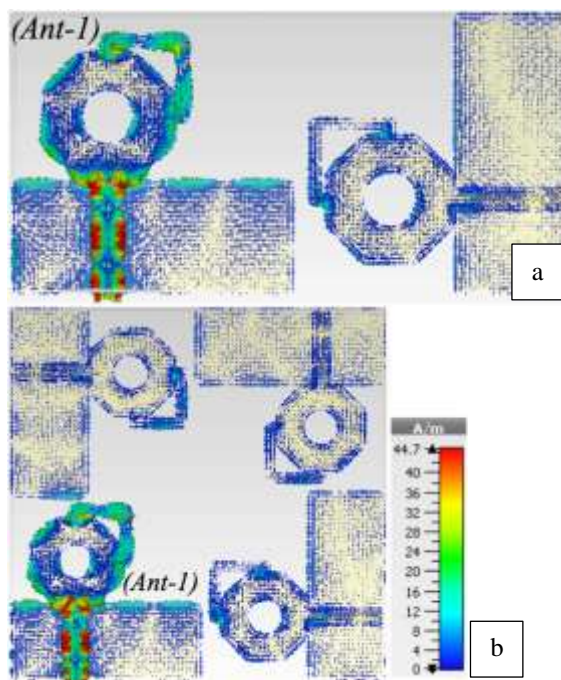
$$DG = \sqrt{100 - 100ECC)} \quad \textbf{(3.2)}$$

Figure 4. Vectoral surface current distribution of the proposed (a) 2×2 and (b) 4×4 MIMO antennas at 13.3 GHz, when Ant-1 is excited.
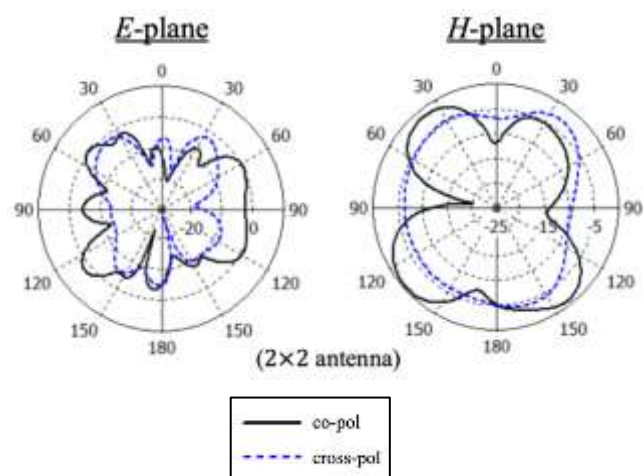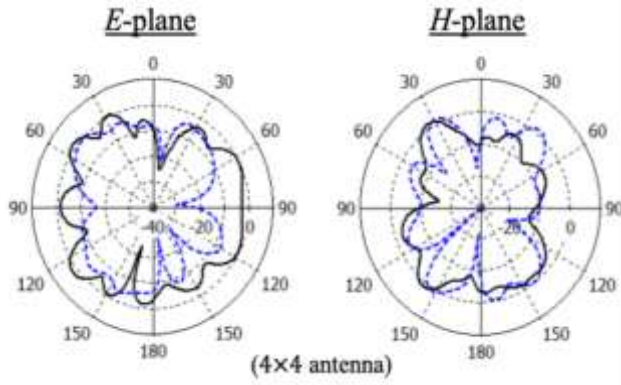
Figure 5. Far field radiation patterns of Ant-1 at 13.3 GHz for the MIMO antennas.

In Table 3, the proposed MIMO antennas are compared with other MIMO antennas that are most recently reported in literature. As seen from the comparison table, both of the presented MIMO antennas have the highest impedance bandwidth of all. Apart from the one reported in [27], the proposed antennas in this study have better isolation and ECC value. On the other hand, except the antenna in [28], the proposed 2×2 and 4×4 MIMO designs have larger sizes than the antennas reported in [27, 29, 30].
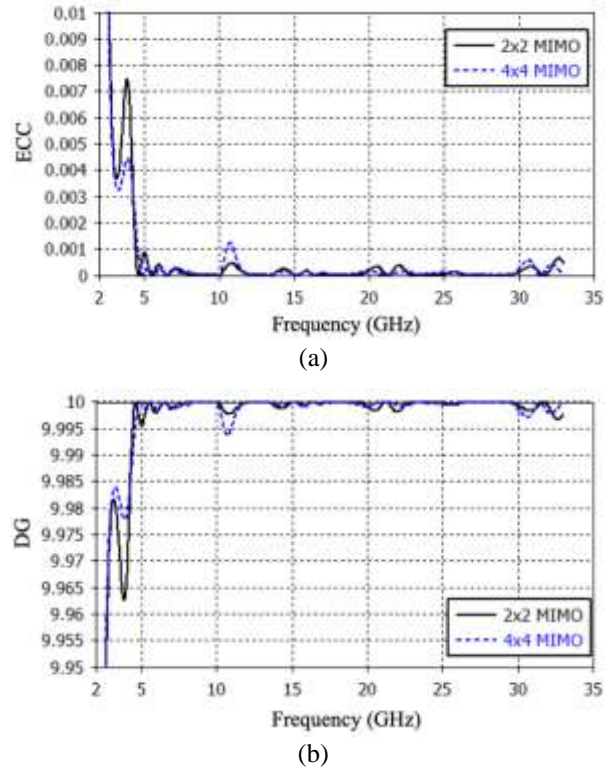
Figure 6. The simulated (a) envelope correction coefficient and (b) diversity gain results of the proposed 2×2 and 4×4 antennas.

Table 3. Comparison with other studies available on literature.

Reference	Structure	Size (mm^2)	No. of Bands	Operating Bands (GHz)	Bandwidth	Isolation (dB)	ECC
[29]	4×4	45×45	3	3-5 6-8.5 9.3-10.6	2 2.5 1.3	<-17	<0.08
[30]	4×4	40×40	1	3-11	8	<-15	<0.006
[27]	2×2	50×30	1	2.5-15	12.5	<-20	0.04
[28]	-	60×60	1	2.35-2.45	0.1	<-18	<0.002
Proposed	2×2	80×40	2	2.41-4.1 4.55-31.4	1.69 26.85	<-25	<0.0005
Proposed	4×4	80×80	3	2.41-3.81 4.78-14.83 15.24-31.5	1.4 10.05 16.26	<-20	<0.0005

4. Conclusion

The 2×2 and 4×4 versions of the previously reported planar SWB monopole antenna are developed and analyzed in this study. MIMO antenna structures are formed by positioning the single antenna elements perpendicular, which facilitates polarization diversity. The 2×2 antenna has an impedance bandwidth ($|S_{11}| \leq -10$ dB) of 1.69 and 26.85 GHz; whereas the 4×4 antenna's bandwidth values are calculated as 1.4, 10.05 and 16.26 GHz. Therefore, the presented MIMO antennas are suitable to be used with millimeter wave applications. Successful results are obtained from the simulated insertion loss and ECC values. The 2×2 and 4×4 antennas have dimensions of 80×40×1 and 80×80×1 mm^3 respectively, so they can be implemented easily in portable devices. Owing to all these aforementioned features the proposed MIMO antennas are appropriate to be used in many different applications operating at many different frequency bands.

Author's Contributions

Tayfun Okan: Drafted and wrote the manuscript, performed the experiment and result analysis.

Ethics

There are no ethical issues after the publication of this manuscript.

References

1. Isaac, AA, Al-Rizzo, H, Yahya, S, Al-Wahhamy, A, Tariq, SZ. 2020. Miniaturized MIMO antenna array of two vertical monopoles embedded inside a planar decoupling network for the 2.4 GHz ISM band. *IET Microwaves, Antennas & Propagation;* 14(1): 132-140.

2. Li, PK, You, CJ, Yu, HF, Cheng, YJ, Yang, YW, Deng, JH. 2018. A high frequency ratio quadri-band frequency independently tunable antenna with spurious-mode suppression. *Microwave and Optical Technology Letters;* 60: 1445–1452.

3. Okan, T. 2020. Design and analysis of a quad-band substrate-integrated- waveguide cavity backed slot antenna for 5G applications. *International Journal of RF and Microwave Computer Aided Engineering;* 30(7): e22236.

4. Cui, L, Guo, J, Liu, Y, Sim, C. 2019. An 8-Element Dual-Band MIMO Antenna with Decoupling Stub for 5G Smartphone Applications. *IEEE Antennas and Wireless Propagation Letters;* 18(10): 2095-2099.

5. Hatami, N, Nourinia, J, Ghobadi, C, Majidzadeh, M, Azarm, B. 2019. High Inter-Element Isolation and WLAN Filtering Mechanism: A Compact MIMO Antenna Scheme. *AEU - International Journal of Electronics and Communications;* 109: 43-54.

6. Mondal, K, Sarkar, PP. 2017. Dual band compact monopole antenna for ISM 2.4/5.8 frequency bands with bluetooth, Wi-Fi, and mobile applications. *Microwave and Optical Technology Letters;* 59(5): 1061–1065.

7. Pazin, L, Kogan, I, Leviatan, Y. 2008. Flat-plate triangular monopole antenna for Wi-Fi/WiMAX/DVB-H applications. *Microwave and Optical Technology Letters;* 50(11): 2922-2925.

8. Werner, PL, Werner, DH. 2005. Design synthesis of miniature multiband monopole antennas with application to ground-based and vehicular communication systems. *IEEE Antennas and Wireless Propagation Letters;* 4: 104-106.

9. Tetik, E, Tetik, GD. 2018. The effect of a metamaterial based wearable monopole antenna on the human body. *Celal Bayar University Journal of Science;* 14(1): 97-93.

10. Gupta, A, Kansal, A, Chawla, P. 2019. Design of a patch antenna with square ring-shaped-coupled ground for on-/off body communication. *International Journal of Electronics;* 106(12): 1814-1828.

11. Toktaş, A, Yerlikaya, M, Yiğit, E. 2016. Microstrip-fed Triangular UWB Microstrip Antenna Based on DGS. *International Journal of Applied Mathematics Electronics and Computers;* (Special Issue-1): 43-47.

12. Biçer, M, Akdağlı, A. 2017. Designing a compact monopole microstrip antenna operating at ultra-wide band for microwave imaging applications. *Turkish Journal of Engineering;* 1(2): 69-66.

13. Okan, T. 2020. A compact octagonal-ring monopole antenna for super wideband applications. *Microwave and Optical Technology Letters;* 62(3): 1237-1244.

14. Liu, Y, Liu, P, Meng, Z, Wang, L, Li, Y. 2018. A Planar Printed Nona-Band Loop-Monopole Reconfigurable Antenna for Mobile Handsets. *IEEE Antennas and Wireless Propagation Letters;* 17(8): 1575-1579.

15. Das, GK, Shaw, T, Mitra, D, Mitra, M. 2019. Directivity enhancement of wire monopole antenna using magnetic metamaterials. *International Journal of RF and Microwave Computer-Aided Engineering;* 29(8): e21778.

16. Tütüncü, B, Urul, B. 2019. LHM Superstrate for High Directivity Microstrip Antenna. *Celal Bayar Üniversitesi Fen Bilimleri Dergisi;* 15(1): 71-74.

17. Li, D, Chen, Z, Liu, Y, Wang, J, Wu, H. 2020. Signal interference-based selectivity-enhancement technique for omnidirectional monopole antenna. *Microwave and Optical Technology Letters;* 62(10): 3203-3208.

18. Kuzu, S, Akçam, N. 2017. Array antenna using defected ground structure shaped with fractal form generated by Apollonius circle. *IEEE Antennas and Wireless Propagation Letters;* 16: 1020-1023.

19. Mahmoud, KR, Montaser, AM. 2018. Performance of tri-band multi-polarized array antenna for 5G mobile base station adopting polarization and directivity control. *IEEE Access;* 6: 8682-8694.

20. Bactavatchalame, P, Rajakani, K. 2020. Compact broadband slot-based MIMO antenna array for vehicular environment. *Microwave and Optical Technology Letters;* 62(5): 2024-2032.

21. Ren, Z, Zhao, A, Wu, S. 2019. MIMO Antenna with Compact Decoupled Antenna Pairs for 5G Mobile Terminals. *IEEE Antennas and Wireless Propagation Letters;* 18(7): 1367-1371.

22. Cheng, Y, Liu, H, Sheng, BQ, Zhu, L. 2020. A compact 4-element MIMO antenna for terminal devices. *Microwave and Optical Technology Letters;* 62(9): 2930-2937.

23. Taghizadeh, H, Ghobadi, CH, Azarm, B, Majidzadeh, M. 2019. Grounded Coplanar Waveguide-fed Compact MIMO Antenna for Wireless Portable Applications. *Radioengineering;* 28(3): 528-534.

24. Cihangir, A, Ferrero, F, Jacquemod, G, Brachat, P, Luxey, C. 2014. Neutralized Coupling Elements for MIMO Operation in 4G Mobile Terminals. *IEEE Antennas and Wireless Propagation Letters;* 13: 141-144.

25. Aslan, B, Dikmen, O, Kulac, S, Elbir, AM. 2018. Evaluation of Reconfigurable Multiple and Compact Micro-Strip Antennas for MIMO Systems. *Balkan Journal of Electrical and Computer Engineering;* 6: 46-50.

26. Okan, T, Akçam N. 2018. Analysis of antennas around NURBS surfaces by using a hybrid method. *Radioengineering;* 27(3): 703-710.

27. Tripathi, S, Mohan, A, Yadav, S. 2015. A compact koch fractal UWB MIMO antenna with WLAN band-rejection. *IEEE Antennas and Wireless Propagation Letters;* 14 (4): 1565–1568.

28. Ali, WAE, Ibrahim, AA. 2017. A compact double-sided MIMO antenna with an improved isolation for UWB applications. *AEU - International Journal of Electronics and Communications;* 82: 7–13.

29. Iqbal, A, Saraereh, OA, Ahmad, AW, Bashir, S. 2018. Mutual coupling reduction using F- shaped stubs in UWB MIMO antenna. *IEEE Access;* 6: 2755–2759.

30. Yu, K, Li, Y, Liu, X. 2018. Mutual coupling reduction of a MIMO antenna array using 3-D novel meta-material structures. *ACES Journal;* 33(7): 758-763.

Celal Bayar University Journal of Science

Hybrid of Thevenin and Norton Equivalent Circuits Analogous to a Source Equivalence Theorem in Electromagnetics

Ömer Işık[1][*] (iD), Lokman Erzen[2] (iD), Ali Uzer[3] (iD)

[1]Department of Electrical and Electronics Engineering, Beykent University, Istanbul, Turkey
[2]Applied Electronics and Systems Engineering, Regent University College of Science and Technology, Accra, Ghana
[3]Vocational School, Program of Electricity, Beykent University, Istanbul, Turkey
* omeri@beykent.edu.tr
*Orcid: 0000-0002-0726-9446

Abstract

According to the conventional perception among engineers, once a circuit is reduced to its Thevenin or Norton equivalent, the voltage and current may be determined only at the load, but not in the remaining parts. The other voltages and currents that exist in the remaining parts of circuit should be determined by returning to the original circuit; substituting the solutions obtained at the load location; and then employing the rules of circuit theory. In this paper, we presented a source equivalence theorem wherein such a back-substitution is never need. It splits an original circuit into two sub-circuits that can be solved separately by using different techniques. Then the voltages and currents everywhere in the circuit can be obtained as a sum of the solutions of those two sub-circuits without making any back-substitution.

Keywords: Nonlinear circuits, Source equivalence, Thevenin theorem, Norton theorem, Equivalent circuits, Integrated circuit interconnections.

1. Introduction

The Thevenin and Norton theorems were developed by Hermann Von Helmholtz, Léon Charles Thévenin, Edward Lawry Norton, and Hans Ferdinand Mayer in the period 1853-1926, [1, 2]. These theorems are described in a lot of books and papers such as [3- 7] and also used in the analysis of practical problems as in [8-10].

The Thevenin and Norton theorems can be used for determining the responses across a load in a circuit. The voltages and currents in the remaining parts should be determined by making back substitutions. Consider a circuit as seen in Figure 1, where N_{ext} stands for a linear network, N_{load} stands for a (possibly) nonlinear network, and S means a surface enclosing N_{load}. Its Thevenin or Norton equivalents will be as shown in Figure 2 or Figure 3 respectively. The sources $v_T(t)$ and $i_N(t)$ are determined conventionally by replacing N_{load} in the original circuit by an open-circuit or a short-circuit. Note that all sources within N_{ext} in the equivalent circuit are deactivated (switched off), therefore, N_{ext} may be

reduced to a single impedance $Z_{eq}(\omega)$ since it is a linear network.

In case N_{load} is nonlinear, the analysis cannot be carried out in the frequency domain but an impulse response $z_{eq}(t)$ should be used instead of $Z_{eq}(\omega)$. That may be written as $z_{eq}(t) = F^{-1}\left\{Z_{eq}(\omega)\right\}$, where F^{-1} means the inverse Fourier transform operator.
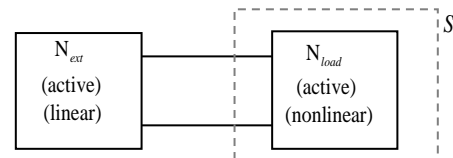
Figure 1. The original circuit. It is made up of linear components except some components inside S, which may be nonlinear.
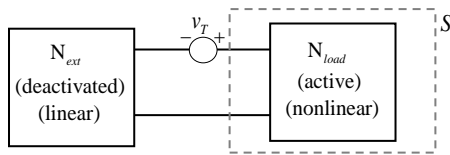
Figure 2. The Thevenin equivalent of the original circuit.
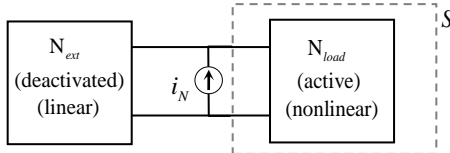
Figure 3. The Norton equivalent of the original circuit.

After that the equivalent circuit may be solved by employing a suitable technique such as finite difference time domain method. But in this manner, one can obtain solutions for voltages and currents only within N$_{load}$. For determining voltages and currents in the remaining parts, i.e., within N$_{ext}$, one should substitute the results into the original circuit in Figure 1 and then proceed to calculate the voltages and currents in N$_{ext}$. The overall procedure will be lengthy due to this back substitution procedure.

On the other hand, such back-substitutions will not be needed according to a new theorem that will be given in the next section. It was postulated during an investigation of electromagnetic source equivalence principles in [11]. In that paper, a newly given electromagnetic source equivalence theorem was shown to be analogous to a hybrid form of Thevenin and Norton theorems of circuit theory.

2. The New Equivalence Theorem

Theorem: Assume a circuit, called Circuit A, is made up of linear components except for one or more nonlinear components located inside a closed surface S as seen in Figure 4. Any voltage or current in this circuit can be written as

$$v_A(t) = v_B(t) + v_C(t) \\ i_A(t) = i_B(t) + i_C(t) \text{, outside } S, \quad \textbf{(2.1)}$$

$$v_A(t) = v_C(t) \\ i_A(t) = i_C(t) \text{, within } S, \quad \textbf{(2.2)}$$

where $v_B(t)$ and $i_B(t)$ denote responses in Circuit B and $v_C(t)$ and $i_C(t)$ denote responses in Circuit C; which are described below.

Circuit B: It is the same as Circuit A except for N$_{load}$ is replaced by an arbitrarily chosen network N$_{test}$ as seen in Figure 5.

Circuit C: It is the same as Circuit A except for: all sources in N$_{ext}$ are switched off; a Thevenin source $v_T(t)$ is inserted across terminals at the interface; and a Norton source $i_N(t)$ is connected in parallel across terminals at the interface as seen in Figure 6. The sources $v_T(t)$ and $i_N(t)$, respectively, are equal to the voltage and current observed at the indicated location in Figure 5.

3. Comments

i. The proof of theorem (with a slightly different notation) can be found in an appendix in [11] and so we do not repeat it.

ii. Note that the expressions are given in the time domain since the circuits are nonlinear in the most general sense. The expressions will be literally valid in the phasor domain in the case where N$_{load}$ is also a linear network.

iii. The solution in a nonlinear circuit may not be unique. For instance, when a nonlinear resistor is connected to a DC source, there may be multiple solutions for the current depending on the current-voltage characteristic of the resistor. In case Circuit A has multiple solutions, then each solution can still be written as in (2.1) and (2.2) since Circuit C in that case will also have multiple solutions.

Circuit B and Circuit C are standalone circuits. They can be analyzed using different methods. For instance, Circuit B may be solved in the phasor domain (provided N$_{test}$ is linear) by using analytical methods, whereas Circuit C may be solved in the time domain by using finite differences methods.

The analysis can be simplified greatly if the test network N$_{test}$ in Circuit B is chosen intuitively. For example, the terminals may be short-circuited or open-circuited for simplifying the analysis. In both cases Circuit B may be solved in the phasor domain by using analytical methods. But in the general case, N$_{test}$ may be a linear or nonlinear resistor, capacitor, inductor, a voltage source, current source e.t.c., or even an interconnection of a number of such components as demonstrated in an example in the following section.
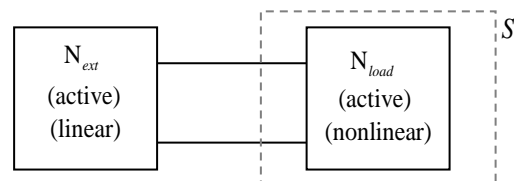
Figure 4. Circuit A (the original circuit). *S* stands for a closed surface enclosing a network N$_{load}$, which may be nonlinear; whereas a network N$_{ext}$ outside *S* is linear.
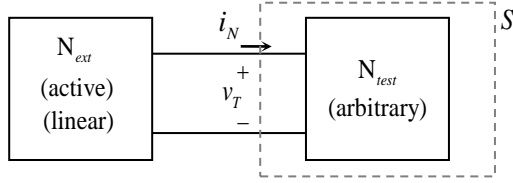
Figure 5. Circuit B (a test setup). It is for determining the sources $v_T(t)$ and $i_N(t)$. The network N$_{load}$ has been replaced by an arbitrarily chosen N$_{test}$.
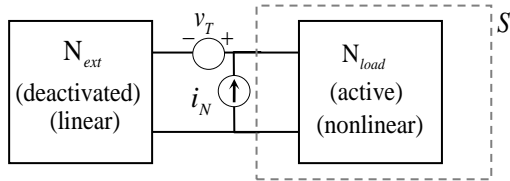
Figure 6. Circuit C (a hybrid equivalent circuit). All sources outside *S* are switched off, while the Thevenin and Norton sources $v_T(t)$ and $i_N(t)$ are placed in the terminals. The time variables are dropped for simplicity.

4. Numerical Example

We consider a circuit as shown in Figure 7, which is used in practice for suppressing multiple reflections of logic signals in interconnected digital systems. It is the same circuit analyzed in [12] (in Example 3.2) and we have chosen it for validating accuracy of our results. The given circuit involves a 5V step source with a 1ns rise time as shown in the inset. The is an air filled transmission line connecting the source to two identical diodes each of which is equivalent to a 3Ω resistor plus a nonlinear capacitor and nonlinear resistor as shown in the inset. The capacitance of nonlinear capacitor is defined by an equation

$$C(v_d) = 38.8 \times 10^{-12} / \sqrt{1 - v_d / 0.7531} \text{ Farad} \quad \textbf{(4.1)}$$

so that the charge of capacitor is to be written as

$$Q_C = v_d C(v_d) \quad \textbf{(4.2)}$$

and the current of capacitor is to be calculated from

$$i_C = \frac{d}{dt}\{Cv_d\} = C\frac{dv_d}{dt} + v_d \frac{dC}{dv_d}\frac{dv_d}{dt} \quad \textbf{(4.3)}$$

The terminal equation of nonlinear resistor is given by

$$i_d = 2.58327 \times 10^{-14} \left(e^{v_d/0.026} - 1\right) \text{Amper} \quad \textbf{(4.4)}$$

We employ the theorem in calculation of a current $i_{A,ext}(t)$ as indicated in the figure. Let the given circuit be Circuit A. It is possible to split Circuit A into a subcircuit as seen in Figure 8. containing an arbitrarily

selected resistor R_{test} inside a surface *S* and another subcircuit containing equivalent sources placed across the surface *S* as seen in Figure 9. The theorem says that $i_{A,ext}(t)$ can be written as a sum $i_{B,ext}(t) + i_{C,ext}(t)$ of currents indicated in the figures.

Consider the resistor R_{test} seen in Figure 8. It can be chosen arbitrarily and the choice affects the strengths of Thevenin and Norton sources $v_T(t)$ and $i_N(t)$. If we use an open circuit, $R_{test} = \infty$, then $i_N(t)$ will be zero and the voltage $v_T(t)$ can be determined simply by employing a conventional bouncing diagram method. Alternatively, if we use $R_{test} = 0$ then $v_T(t)$ will be zero and the current $i_N(t)$ can be determined by employing bouncing diagram method. On the other hand, if we use $R_{test} = 45\Omega$, that is a matched-load according to the transmission line in the problem, the reflections will not occur along the transmission line. The voltage and current at the end of transmission line, $v_T(t)$ and $i_N(t)$, simply equal to

$$v_T(t) = \frac{45}{55} v_{ext}(t - t_0) \quad \textbf{(4.5)}$$

$$i_N(t) = \frac{1}{55} v_{ext}(t - t_0) \quad \textbf{(4.6)}$$

where t_0 stands for the time delay, that is, the ratio of the line length and the speed of light

$$t_0 = \frac{1.5}{3 \times 10^8} = 5 \times 10^{-9} = 5\text{ns} \quad \textbf{(4.7)}$$

Any choice (open-circuit, short-circuit, or matched-load) for R_{test} affects only $i_{B,ext}(t)$ and $i_{C,ext}(t)$. But the sum $i_{B,ext}(t) + i_{C,ext}(t)$ always equals to $i_{A,ext}(t)$ according to the theorem. The same is true for any voltage or current anywhere along the transmission line.
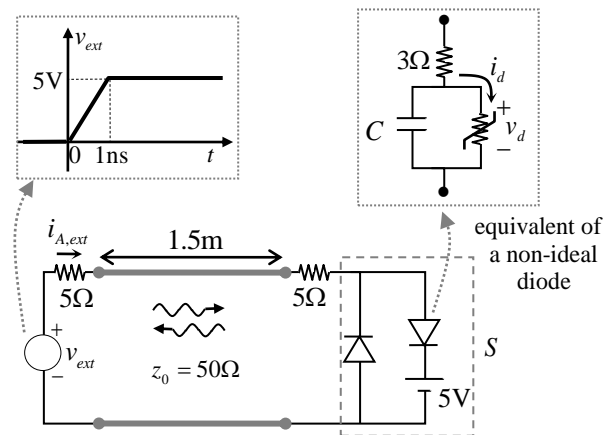
Figure 7. Circuit A: a voltage source as shown in the inset is feeding a nonlinear load, which is made up of two diodes and a DC source, via an air filled

transmission line. The diodes are identical and each has an equivalent as indicated.
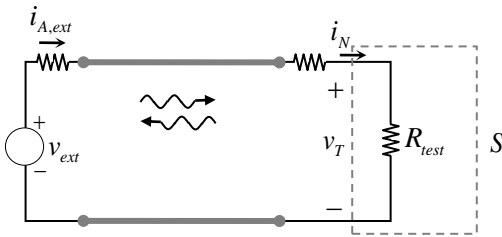
Figure 8. Circuit B: a resistor R_{test} is used to determine $v_T(t)$ and $i_N(t)$, which are to become equivalent sources in an equivalent circuit.
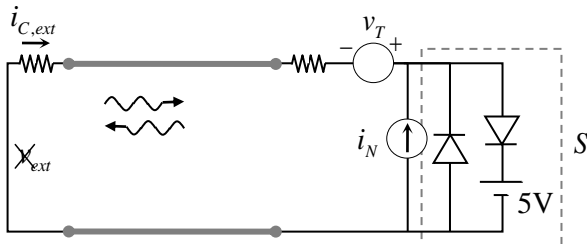
Figure 9. Circuit C: the equivalent circuit with the sources $v_T(t)$ and $i_N(t)$ at the interface.

According to the given theorem, we don't need to place a resistor R_{test} inside S in Circuit B but any number of linear and nonlinear components as well as sources may be placed inside S. For example, we may place some capacitors, voltage sources, and diodes inside S as seen in Figure 10. There is no restriction in selection of the types and connections of components. We make solution of this circuit to demonstrate the validity of our theorem and arbitrariness in its utilization. Otherwise the capacitors, voltage sources, and diodes placed inside S as seen in Figure 10. are not for simplifying the solution of problem. We employ a finite difference time domain scheme as described in [13] for the numerical solution of circuit in Figure 10. We use a time step $\Delta t = 10\text{ps}$ up to 100nS and a segment size $\Delta z = 3\text{mm}$ along the transmission line of length 1.5m. The selected values satisfy the criteria

$$\frac{\Delta z}{\Delta t} \geq 3 \times 10^8 \, \text{m/s} \qquad (4.8)$$

for the stability of solutions along the air filled transmission line.
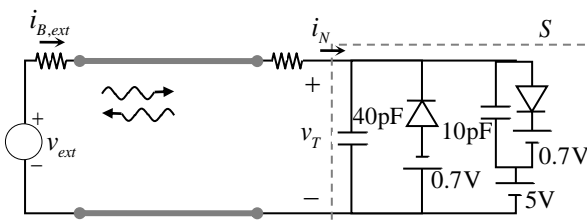
Figure 10. Circuit B: some arbitrarily chosen capacitors, sources, and diodes are placed inside S.

We calculate $v_T(t)$ and $i_N(t)$ as shown in Figure 11. They are calculated and saved into a memory for a later use in each time step. Then the saved values are substituted into Circuit C as independent sources in shown Figure 9. Circuit C, in turn, is solved by employing the same computational scheme and the same parameters (Δt and Δz) that were used when solving Circuit B. We also exploit Newton-Raphson iteration method in each time step for solving nonlinear equations of diodes. The iterations are carried out until the changes in diode voltages become less than 10^{-7}V.

The original problem, Circuit A, is also solved using the same computational scheme and parameters (Δt and Δz) mentioned above. Specifically the current $i_{A,ext}(t)$ is calculated for making comparisons with other calculated values. Calculations have shown that the sum $i_{B,ext}(t) + i_{C,ext}(t)$ exactly equals to $i_{A,ext}(t)$ for all $t \geq 0$ and attests the statement of theorem in (2.1). It is also obvious from the separate plots of $i_{A,ext}(t)$, $i_{B,ext}(t)$, and $i_{C,ext}(t)$ shown Figure 12. Hence the plots also validate visually the validity of theorem. Meanwhile the curve of $i_{A,ext}(t)$ given in this paper matches with the previously calculated results given in [12].
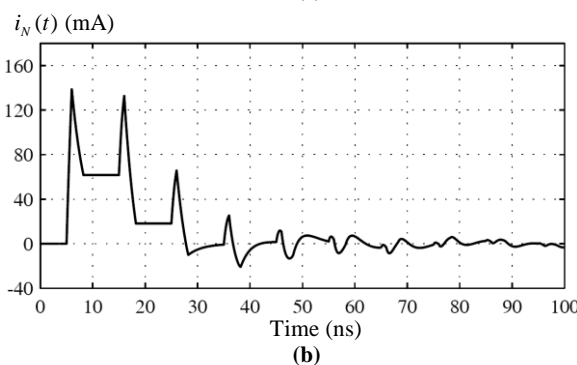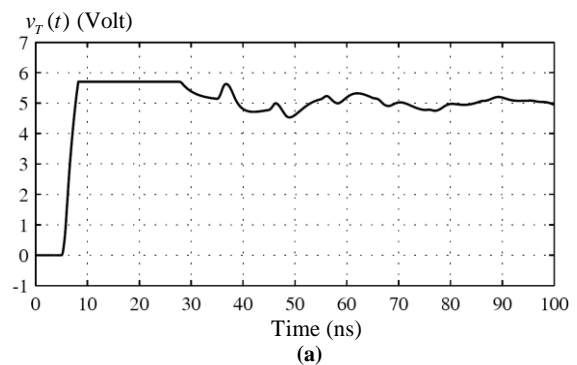
Figure 11. (a) The Thevenin voltage $v_T(t)$ versus t according to the case inside S in Figure 10. **(b)** The Norton current $i_N(t)$ versus t according to the case inside S in Figure 10.
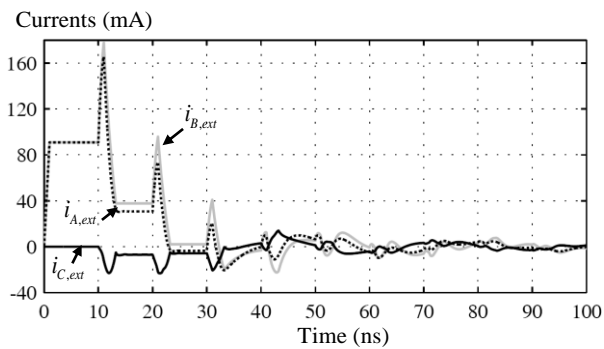
Figure 12. The numerical results for the individual currents $i_{A,ext}(t)$, $i_{B,ext}(t)$, and $i_{C,ext}(t)$ in circuits in Figure 7, Figure 10, and Figure 9, respectively. It displays the sum $i_{B,ext}(t) + i_{C,ext}(t)$ is equal to $i_{A,ext}(t)$ as claimed by the theorem.

5. Conclusion

In circuit theory, the Thevenin and Norton theorems are two of the important theorems that may be used to simplify analysis of complex circuits. It is believed that these source equivalence theorems can be used to calculate voltages and currents only across a specific component called the load in a circuit, but those in the remaining parts should be calculated via back substitutions. Sometimes, this back substitution procedure can be very lengthy.

We proposed a new circuit equivalence theorem, which eliminates necessity of any back-substitution procedure. The theorem splits any bulky circuit into two sub-circuits each of which can be solved by using a different method. Then the solutions of sub-circuits can be added simply to obtain the overall solution. The theorem is applied to a practical problem involving a transmission line and nonlinear components.

Author's Contributions

Ömer Işık: Made literature search, prepared computer codes for numerical solutions of the sample problem, made simulations, and wrote the manuscript.

Lokman Erzen: Made literature search, decided for a sample problem for testing the given theorem, supervised the simulation process, and made comparisons.

Ali Uzer: Extended an electromagnetic equivalence theorem in [11] into the circuit theory and also helped in manuscript preparation.

Ethics

There are no ethical issues after the publication of this manuscript.

References

1. Johnson, DH. 2002. Origins of the equivalent circuit concept: the voltage-source equivalent. *Proceedings of the IEEE*, 91(4): 636-640.

2. Johnson, DH. 2002. Origins of the equivalent circuit concept: the current-source equivalent. *Proceedings of the IEEE*, 91(5): 817-821.

3. Haus, HA, Adler RB. Circuit theory of linear noisy circuits; Cambridge, Massachusetts, New York, Wiley, 1959.

4. Carlin, HJ, Giordano, AB. Circuit theory-An introduction to reciprocal and nonreciprocal circuits; Englewood Cliffs, New Jersey, Prentice-Hall, 1964.

5. Corazza, GC, Someda, CG, Longo, G. 1969. Generalized Thevenin's theorem for linear n-port circuits. *IEEE Transactions on Circuit Theory*, 16(4): 564-566.

6. Hashemian, R. Hybrid equivalent circuit, an alternative to Thevenin and Norton equivalents, its properties and applications. *Midwest Symposium on Circuits and Systems (MWSCAS 2009)*, Mexico, 2009, pp 800-803.

7. Rathore, TS. 2017. Generalized Maximum Power Transfer Theorem. *IETE Journal of Education*, 58(1): 39-41.

8. Femia, N. 1996. A fast method to find the state of switches after forced commutations in switching converters. *Proceedings of IEEE Power Electronics Specialists Conference (ESC'96)*, Atlanta, (2): 1356-1362.

9. Femia, N. 2003. Understanding commutations in switching converters-Part I: Basic theory and application of the compensation theorem. *IEEE Transactions on Aerospace and Electronic Systems*, 39(1): 282-297.

10. Heydt, GT. 2017. G Thevenin's Theorem applied to the analysis of polyphase transmission circuits. *EEE Transactions on Power Delivery*, 32(1): 72-77.

11. Uzer, A. 2012. Some electromagnetic equivalence theorems unified by a single theorem and generalized to a nonlinear case. *IEEE Antennas and Propagation Magazine*, 54(3): 86-99.

12. Chang, FY. 1996. Transient analysis of diode switching circuits including charge storage effect. *IEEE Transactions on Circuits and Systems-I: Fundamental Theory and Applications*, 43(3): 177-190.

13. Dommel, HW. 1969. Digital computer solution of electromagnetic transients in single and multiphase circuits. *IEEE Trans. Power Apparatus and Systems*, 88(4): 388-399.

Celal Bayar University Journal of Science

Synthesis of Palladium Phthalocyanine and Investigation of Sono-Photodynamic Therapy Properties

Göknur Yaşa Atmaca[1]* (iD)

Department of Chemistry, Yildiz Technical University, 34210 Esenler, Istanbul, Turkey
*goknuryasa@gmail.com
*Orcid: 0000-0002-5264-7100

Abstract

In this study, it is desired to apply the Sono-Photodynamic Therapy (SPDT) method to create a more effective therapeutic outcome. There are cell applications of SPDT in the literature, but the sonophotochemical studies are very limited. For this purpose, a new palladium phthalocyanine (PdPc) (**2**) was synthesized and characterized by standard spectroscopy methods. Then its photochemical and photophysical properties were determined in DMSO. Singlet oxygen quantum yield of the complex (**2**) was calculated by both photochemical and sono-photochemical methods. The SPDT method (Φ_Δ =0.90) was found to be more effective than the PDT method (Φ_Δ =0.74), to obtain a high singlet oxygen quantum yield. All the results show that, SPDT improves the therapeutic effects and the synthesized PdPc can be an effective sono/photosensitizer in PDT / or SPDT.

Keywords: Palladium Phthalocyanine, Sonodynamic Therapy, Photodynamic Therapy

1. Introduction

Photodynamic therapy (PDT) is one of the most noticeable applications for cancer treatment. PDT method is dependent on a light-sensitive agent (photosensitizer) injected into the patient. Then the photosensitizer accumulates in the tumor tissue by the addressing method to produce reactive singlet oxygen [1, 2]. PDT is a successful method of producing singlet oxygen. However, the penetration problem of PDT studies limited its applications. Because the depth of penetration of the laser light is more suitable for superficial lesions [3, 4]. To overcome this problem, the sonodynamic therapy (SDT) method has been developed by using ultrasound activated sensitizers inspired by PDT [5, 6]. The ultrasound is preferred in the SDT method because of the deeper penetrating and during the application, the free radicals are formed by the breakdown of water molecules as a result of acoustic cavitations. Afterward, these reactive radicals cause the death of the targeted cell [7]. With these properties, sonodynamic therapy method has developed the disadvantage of photodynamic therapy method, but the sonosensitizers in SDT have not been confirmed for clinical experiments [8, 9]. Because sonophotodynamic studies were required high concentration and this was increased the potential phototoxicity [10, 11]. All of the

problems are required the Sono-photodynamic Therapy (SPDT), a combination of SDT and PDT [3, 12]. In the SPDT method, the sensitizer is activated by both light and ultrasound to obtain sono-photo chemical reactions [13, 14]. Previous studies about the sono-photochemical applications have shown that the sono-photochemical study has a more powerful therapeutic effect than the other therapy methods [14, 15]. SPDT bases on some parameters as the properties of used ultrasound and light, sono/photosensitizers, tumor response to the sensitizer, and light/sound irradiation time [3, 12]. Especially sensitizer selection is the most important issue in this method. The synthesized sono/photo sensitizers should have some properties like a stable chemical composition, high sono-photo sensitivity, high cleaning properties from healthy tissues, and should not be toxic [8, 16].

Singlet oxygen as a reactive oxygen species can kill a cancer cell due to its cytotoxicity if produced in sufficient quantity. The our previous studies show that the obtained singlet oxygen yield is quite affected by the used chemical method [17-19]. That's why, the purpose of this paper is to present that the heavy center metal atom and the sono-photochemical method increase singlet oxygen efficiency. In this way, the new palladium phthalocyanine was synthesized and

investigated its photophysicochemical properties and also compared with the zinc and indium derivatives reported before [18, 20]. The singlet oxygen activity of the synthesized phthalocyanine was analyzed by both SDT, PDT and SPDT methods and presented by comparison.

2. Experimental
2.1. Materials and equipment

Details about the materials and equipment can be found in the supplementary material.

2.2. Synthesis

The synthesis of compound (1) was prepared according to the our previous study [20]. New palladium phthalocyanine (2) was synthesized in this study for SPDT studies. The synthesized complex was characterized by performing different techniques such as ^{1}H NMR, MALDI-TOF, FT-IR, UV-Vis spectroscopy, elemental analysis and then investigated photodynamic and sono-photodynamic therapy properties.

2.2.1. 4-[4-(Bromophenoxy) phenoxy] phthalonitrile (1)

Compound **1** was synthesized as given in the literature [20].

2.2.4. Palladium (II) chloride phthalocyanine (2)

A mixture of compound (1) (100 mg, 0.25 mmol), PdCl$_2$ (13.27 mg, 75.00 mmol) and DBU (0,2 mL, 0.13 mmol) in n-hexanol (2,0 mL) was refluxed and stirred under inert atmosphere for 12 h. The product was precipitated, centrifuged and then washed with hot solvents (hexane, methanol, ethanol). The final product was further purified by column chromatography over a silica gel using a mixture of CHCl$_3$: MeOH (100/2 v/v) as eluent. Yield: 0.065 g (15%). UV-Vis (DMSO): $\lambda_{max,}$ nm (log ε) 684 (5.22), 617 (4.36), 325 (4.81). FT-IR υ_{max} /cm^{-1} (KBr pellet): 2923 (Ar-CH), 1596 (C=C), 810 (C-Br) 1232, 1186 (C-O-C); ^{1}H NMR (CDCl$_3$): δ= 7.55-7.45 (12H, m, Pc-H), 7.15-6.95 (16 H, m, Ar-H), 6.85-6.70 (16 H, m, Ar-H). The results of elemental analysis, Calcd for C$_{80}$H$_{44}$Br$_4$N$_8$O$_8$Pd: C, 57.49; H, 2.65; N, 6.70: Found: C, 56.80; H, 2.34; N, 6.96; MS (MALDI-MS; Dithranol (DIT) as matrix) m/z: Calc. 1671; Found: 1684 [M+8 (^{81}Br- Ref. [18]+ 5H]$^+$ and 1797 [M+ 8+ 3K +H]$^+$.

2.3. Photophysical and photochemical studies

Single oxygen, photodegradation and fluorescence quantum yields were calculated performing the experimental setup described in the literature [21-23].

3. Results and discussion
3.1. Synthesis and characterization

Scheme 1 shows the synthetic route for the preparation of the phthalonitrile derivative (**1**) and the metallophthalocyanine (**2**). As shown, compound **1** was obtained by mixing of 4-nitrophthalonitrile and 4-4(bromophenoxy) phenol in DMSO at room tempareture for one day. This aromatic nucleophilic reaction was catalyzed by K$_2$CO$_3$ as the base. The pure compound **1** had a 50% yield after the recrystallization by methanol. To synthesis of palladium phthalocyanine (**2**), the cyclotetramerization process was performed using palladium chloride salt. After the reaction, on the FT-IR spectra, the distinctive C≡N peaks disappeared. Also, the typical vibrations corresponding to the C-O-C group occurred at 1232, 1186 cm^{-1}, and aromatic C-H peaks were observed at 2923 cm^{-1}, **Figure 1**.

In UV-Vis studies, the absorption bands of the complex were the typical spectrum of phthalocyanine. One of them was in the visible region at 684 nm (Q band) and the other band was in the UV region at 325 nm (B band) due to n → π * transitions [24].

In ^{1}H-NMR spectrum were showed signals with δ ranging from 7.74 to 6.92, integrating for a total of 11 protons for complex **1** and 7.55-6.70 integrating for a total of 44 protons (δ= 7.55-7.45 (12H, m, Pc-H), 7.15-6.95 (16 H, m, Ar-H), 6.85-6.70 (16 H, m, Ar-H)) for complex **2** as expected, **Figure 2**.

For mass spectrum, the presence of molecular ion peaks at m/z 392.0 [M+H]$^+$ for complex **1**, 1684 [M+8 (^{81}Br-Ref.[18]+5H]$^+$ and 1797 [M+8+3K+H]$^+$ for complex **2**, approved the recommended structures. All analytical results were consistent with the predicted structures.

3.2. Photophysical studies
3.2.1. Ground state electronic absorption spectra

The characteristic features of phthalocyanines can determined by examining of their absorption spectra and the aromatic 18π-electron structure of the phthalocyanine ring specifies the spectral properties of Pcs. The UV-Vis spectra of Pcs mainly include two strong bands denoted B- and Q-band. π-π* transition from the HOMO (highest occupied molecular orbital) to the LUMO (lowest unoccupied molecular orbital) of the Pc ring at visible region leads to the appearance of the Q-band giving the blue/green color of Pcs [25]. The absorption spectra of compound **2** was studied in DMSO and are presented in **Fig 3**. The Q-band of complex **2** appeared at 684 nm and its B-band was observed at 325 nm. The log ε values of the bands are 5.22 for Q-band and 4.81 for B-band. The heavier metal ions usually have more red-shift of the Q-band. Comparing the Q band of complex **2** with the ZnPc derivative (Q band= 680 nm) [20], the PdPc makes the complex 4 nm more red shift.
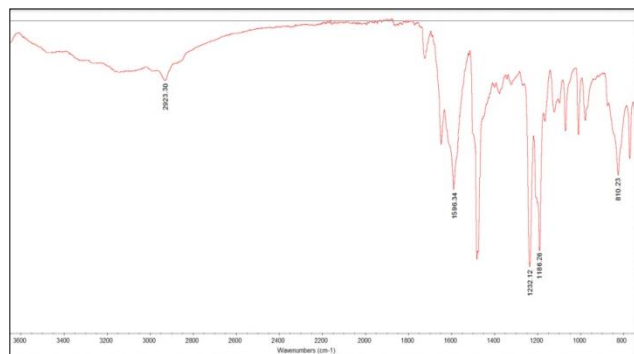
Figure 1. The FT-IR spectra of compound **2**
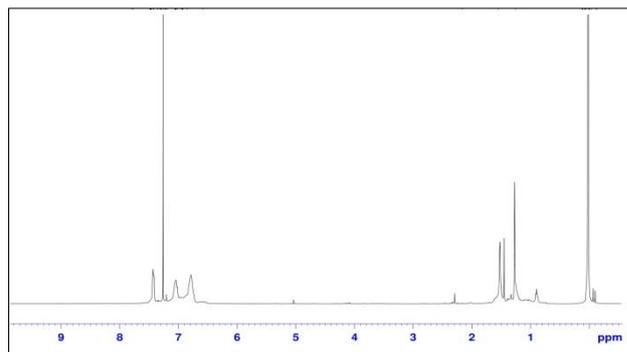
Figure 2. ^{1}H-NMR (CDCl$_3$) spectrum of compound **2**
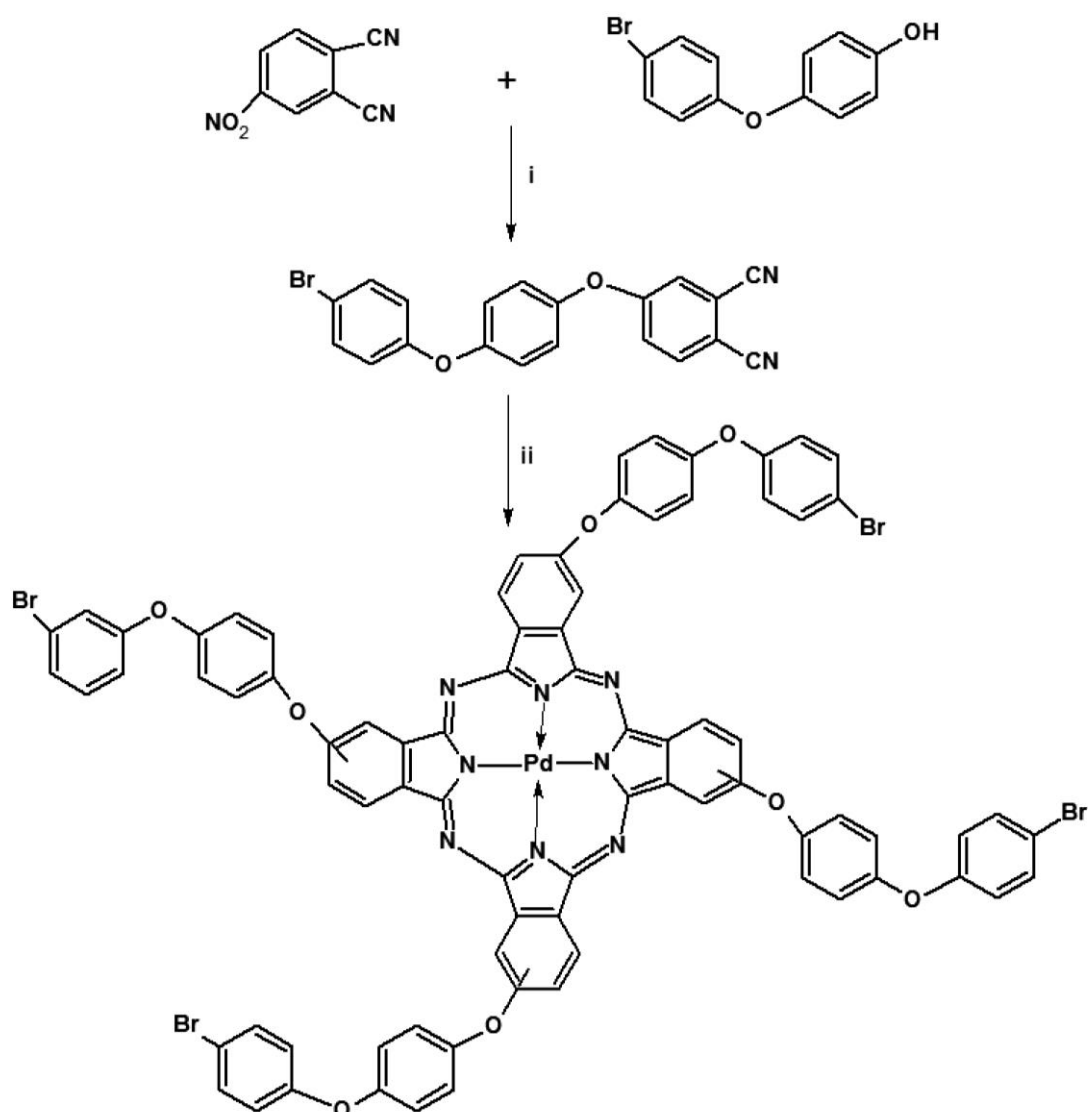
Scheme 1. Synthesis of new palladium phthalocyanine. Reagents and conditions; **(i)** K$_2$CO$_3$, DMF, 24 hours **(ii)** Palladium chloride, hexanol, DBU, argon atm, reflux 12 hours.

3.2.2. Fluorescence Spectra and Quantum Yield (Φ_F)

The fluorescence properties of photosensitizing molecules are important measures to determine the suitability of these molecules as biological imaging materials [26]. The fluorescence property of complex **2** was investigated in DMSO and fluorescence quantum yield is listed in **Table 1**. The absorption, excitation, and emission spectra of the molecule are shown in **Fig 3**. Fluorescence emission maxima was observed at 695 nm and the absorbance spectra was a mirror image of the excitation spectra. The effect of substituent nature and metal ion on the value of Φ_F were examined and the fluorescence quantum yield was found as 0.17. The value was determined using the comparative method. Unsubstituted zinc phthalocyanine (ZnPc) in DMSO ($\Phi_F = 0.20$) was used as the standard [16].

Generally, the heavy metal effect leads to lower values of Φ_F due to the heavy atom which promotes intersystem crossing [27] and the new palladium phthalocyanine have lower fluorescence quantum yields

than standard ZnPc ($\Phi_F = 0.20$ in DMSO) [16] and its previously reported ZnPc pattern ($\Phi_F = 0.23$) [20].
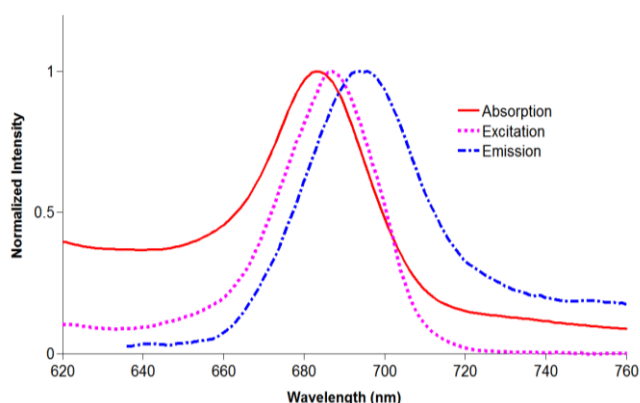
Figure 3. Absorption (684), excitation (687) and emission (695) spectra of compound **2** in DMSO.

Table 1. Spectral parameters of photophysical and photochemical properties of compound

Solvent	Q band λ_{max}, nm	log ε	Excitation λ_{Ex}, nm	Emission λ_{Em}, nm	Φ_F	$\Phi_{\Delta\,(PDT)}$	$\Phi_{\Delta\,(SPDT)}$	$\Phi_d(10^{-4})$
DMSO	684	5.22	687	695	0.17	0.74	0.90	4

3.3. Photochemical studies

3.3.1. Singlet oxygen quantum yields (Φ_Δ) for PDT and SPDT

A sono/or photosensitizer should have effective singlet oxygen yield to be used in photodynamic or sonodynamic therapy. In this part, the singlet oxygen quantum yield was calculated by both sono-photochemical and photochemical studies to achieve higher yields. The yields were determined by using DPBF as a chemical quencher. The spectrum of the intensity of DPBF absorbance at about 417 nm reduced by ultrasound activation and light irradiation and the spectra are present in **Figs. 3-6** and **Table 1**.

In the literature, ultrasound at a frequency of approximately 1MHz is used in cell applications of SPDT [3, 9]. However, in this study, ultrasound at a frequency of 35 kHz was preferred because it was desired to show the singlet oxygen formation in the same UV spectrum. In both PDT and SPDT studies, there were no changes in the Q band intensities, approving that the compound is not degraded.

According to the obtained yields, compound **2** have significantly higher Φ_Δ values than its ZnPc derivative ($\Phi_\Delta = 0.63$) [20] and unsubstituted ZnPc ($\Phi_\Delta = 0.67$) in DMSO and also have lower Φ_Δ values than the indium derivative ($\Phi_\Delta = 0.79$ for PDT method and 0.95 for SPDT method) [18] because of the heavy atom effect that may support intersystem crossing (ISC) [28].

When PDT, SDT, and SPDT were compared, it was seen that the highest decrease in the intensity of DPBF was obtained by the SPDT method, and the lowest decrease was obtained by the SDT method, **Fig. 2**. While the efficiency of the singlet oxygen in the PDT method was $\Phi_\Delta = 0.74$, it was found $\Phi_\Delta = 0.90$ in the SPDT method. This result shows that sensitizer **2** would generate a more therapeutic effect by a combination of sonochemical and photochemical studies.
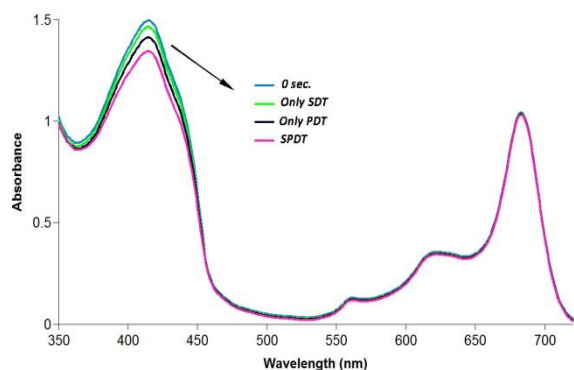
Figure 4. Comparison of SDT, PDT and SPDT spectrum of compound **2** in DMSO
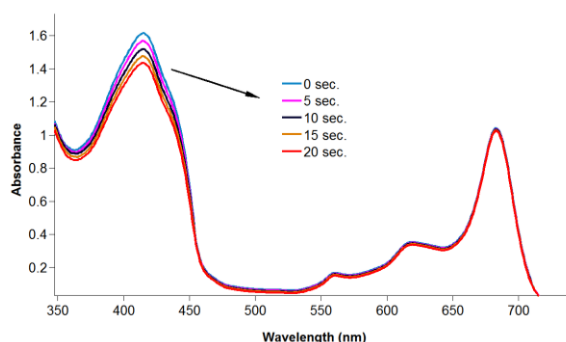
Figure 5. A typical spectrum for the determination of singlet oxygen quantum yield (for PDT method) of compound **2** in DMSO.
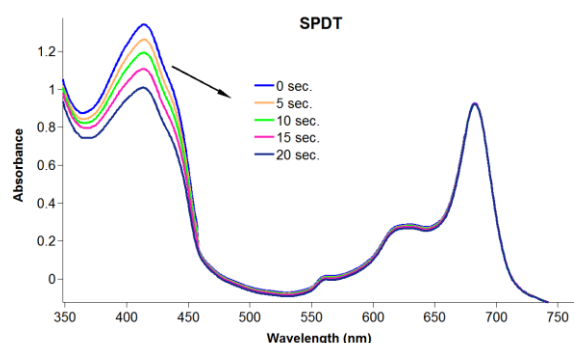
Figure 6. A typical spectrum for the determination of singlet oxygen quantum yield (for SPDT method) of compound **2** in DMSO.

3.3.2. Photodegradation quantum yield (Φ_d)

In photodynamic /or sonodynamic therapy, photosensitizers should be as stable as possible to light in the process of producing singlet oxygen. To investigate the stability, the molecule is irradiated by the light every ten minutes and the maxima Q band is examined using UV-vis spectrometry. The Q band of the molecule was decreased during the irradiation and the observed spectral changes are shown in **Fig. 7** and the quantum yield listed in **Table 1**. The palladium complex showed average stability with Φ_d in the order of 10^{-4}. But PdPc is less stable than its ZnPc derivative ($\Phi_d = 0.8 \cdot 10^{-4}$) because of the heavy metal effect.
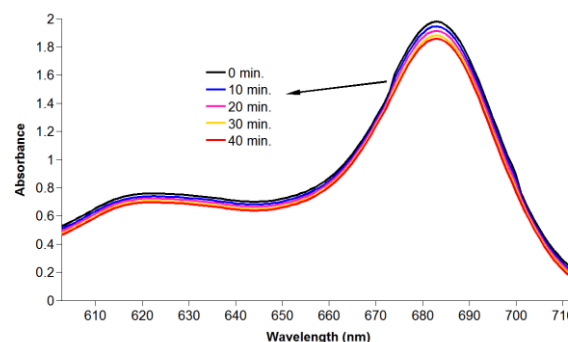
Figure 7. A typical spectrum for the determination of photodegradation of the compound **2** in DMSO.

4. Conclusion

The target of this paper was to enhance the photophysicochemical effect of phthalocyanines by the SPDT method and heavy central atom. In this way, a new palladium phthalocyanine was synthesized and investigated its photochemical and sono-photochemical properties for the first time. A very high result (Φ_Δ =0.90) was obtained in singlet oxygen quantum yield with the SPDT method and palladium center atom. Compared to its previously reported ZnPc derivative, the new PdPc is a more powerful performing intersystem crossing and could be a better sensitizer. Besides, while the efficiency in the PDT method was Φ_Δ =0.74, the efficiency reached Φ_Δ =0.90 with the SPDT method. The yields indicated that only the photochemical study is not sufficient and the sono-photochemical study can be a more effective method for anticancer treatment.

Acknowledgements

Author's Contributions

Göknur Yaşa Atmaca: Drafted and wrote the manuscript, performed the experiment and result analysis.

Ethics

There are no ethical issues after the publication of this manuscript.

References

1. Shen, X.M., Zheng, B.Y., Huang, X.R.,Wang, L., Huang J.D. 2013. First silicon (IV) phthalocyanine-nucleoside conjugates with high photodynamic activity. *Dalton Transaction*, 42 (29), 10398 – 10403.

2. Hışır, A, Köse, G. G., Atmaca, G.Y., Erdogmus, A., Karaoglan, G.K. 2018. Novel carboxylic acid terminated silicon (IV) and zinc (II) phthalocyanine photosensitizers: Synthesis, photophysical and photochemical studies. *Journal Porphyrins and Phthalocyanines*, 22, 1010–1021.

3. Liu, Y., Wang, P., Liu, Q., Wang, X. 2016. Sinoporphyrin sodium triggered sono-photodynamic effects on breast cancer both in vitro and in vivo. *Ultrasonics Sonochemistry*, 31, 437–448

4. Dolmans, D.E., Fukumura, D., Jain, R.K. 2003. Photodynamic therapy for cancer. *Nature Reviews Cancer*, 3, 380–387.

5. Yumita, N., Nishigaki, R., Umemura, K., Umemura, S.i. 1989. Hematoporphyrin as a sensitizer of cell-damaging effect of ultrasound. *Cancer Science*, 80, 219– 222.

6. Trendowski, M. 2014. The Promise of Sonodynamic Therapy. *Cancer Metastasis Reviewer*. 33, 143–160.

7. KÖKEN.,E. C. Doktorate thesis. Adnan Menderes University. Ehrlich Asit Tümör Hücreleri Üzerinde Kloraluminyum Ftalosiyanin ve Dosetakselin Sonodinamik Etkilerinin Araştirilmasi, 2014, Aydın.

8. Chen, H., Zhou, X., Gao,Y., Zheng, B., Tang, F., Huang, J. 2014. Recent progress in development of new sonosensitizers for sonodynamic cancer therapy. *Drug Discovery Today*, 19, 502-509.

9. D.Costley, C.M. Ewan, C. Fowley, A.P. McHale, J.Atchison, N.Nomikou, J. F. Callan. 2015. Treating cancer with sonodynamic therapy: A review. *International Journal of Hyperthermia*, 31(2)107–117.

10. Hai-Jun, Xiao-Bin Zhou, Ai-Lan Wang , Bi-Yuan Zheng , Chih-Kuang Yeh , Jian-Dong Huang. 2018. Synthesis and biological characterization of novel rose bengal derivatives with improved amphiphilicity for sono-photodynamic therapy. *European Journal of Medicinal Chemistry*,145, 86-95.

11. Li., Q., Liu.Q. Wang, P., Feng, X., Wang, H., Wang, X. 2014. The effects of Ce6-mediated sono-photodynamic therapy on cell migration, apoptosis and autophagy in mouse mammary 4T1 cell line. *Ultrasonics*, 54, 4, 981-989.

12. Jin. Z.H. , Miyoshi, N ., Ishiguro, K., Umemura, S ., Kawabata, K ., Yumita, N ., Sakata, I. , Takaoka,K ., Udagawa ,T., Nakajima ,S.,Tajiri ,H. , Ueda, K. , Fukuda, M. , Kumakiri, M. 2000. Combination Effect of Photodynamic and Sonodynamic Therapy on Experimental Skin Squamous Cell Carcinoma in C3H/HeN Mice. *Journal of Dermatol*, 27, 294.

13. Kolarova, H., Tomankova, K., Bajgar, R., Kolar, P., Kubinek, R. 2009. Photodynamic and Sonodynamic Treatment by Phthalocyanine on Cancer Cell Lines. *Ultrasound Medicinal Biology*, 35, 1397.

14. Kessel D, Lo J, Jeffers R, Fowlkes, J.B., Cain, C. 1995. Modes of photodynamic vs. sonodynamic cytotoxicity. *Journal of Photochemistry and Photobiology B Biology* 28(3):219-21.

15. Wang, X., Zhang, W., Xu, Z., Luo, Y., Mitchell, D., Ralph W. 2009. Moss. Sonodynamic and Photodynamic Therapy in Advanced Breast Carcinoma: A Report of 3 Cases. *Integrative Cancer Therapies*, 8, 3, 283–287.

16. Atmaca, G.Y., Dizman, C., Eren, T., Erdoğmuş, A. 2015. Novel axially carborane-cage substituted silicon phthalocyanine photosensitizer; synthesis, characterization and photophysicochemical properties. *Spectrochimica Acta Part A: Molecular and Biomolecular Spectroscopy*, 137, 244-249.

17. Atmaca, G.Y., Measurement of singlet oxygen generation of 9(Hydroxymethyl)anthracene substituted silicon phthalocyanine by sono-photochemical and photochemical studies, *Journal of Molecular Structure,* 1226 (2021)129320.

18. Atmaca, G.Y., Investigation of the differences between sono-photochemical and photochemical studies for singlet oxygen generation of indium phthalocyanine, *Inorganica Chimica Acta*, 515 (2021) 120052.

19. Atmaca, G.Y., Investigation of Singlet Oxygen Efficiency of Di-axially Substituted Silicon Phthalocyanine with Sono-Photochemical and Photochemical Studies, *Polyhedron,* 193 (2021)114894.

20. Kırbaç, E., Atmaca, G.Y., Erdoğmuş, A. 2014. Novel highly soluble fluoro, chloro, bromo-phenoxy-phenoxy substituted zinc phthalocyanines; synthesis, characterization and photophysicochemical properties. *Journal of Organometalic Chemistry,* 752, 115-122.

21. Atmaca, G.Y., Erdoğmuş, A. 2019. Synthesis of new water soluble silicon phthalocyanine substituted by linker sulfur atom and photophysicochemical studies for photodynamic therapy. *Journal of Porphyrins and Phthalocyanines* 23, 1398-1405.

22. Tayfuroglu, O., Kılıçarslan, F.A., Atmaca, G.Y., Erdogmus, A. 2018. Synthesis, characterization of new phthalocyanines and investigation of photophysical, photochemical properties and theoretical studies. *Journal of Porphyrins and Phthalocyanines*, 22, 250-265.

23. Guzel, E., Arslan, B, Atmaca, G.Y., Nebioglu, M., Erdogmus, A. 2019. High Photosensitized Singlet Oxygen Generating Zinc and Chloroindium Phthalocyanines Bearing (4-isopropylbenzyl) oxy Groups as Potential Agents for Photophysicochemical. *Chemistry Select*, 4, 2, 515-520.

24. Güzel, E. 2019. Dual-purpose zinc and silicon complexes of 1, 2, 3-triazole group substituted phthalocyanine photosensitizers: synthesis and evaluation of photophysical, singlet oxygen generation, electrochemical and photovoltaic properties. *Royal Society of Chemistry*. 9, 10854-10864.

25. Sen, P., Dumludağ, F., Salih, B., Özkaya, A.R., Bekaroğlu, Ö. 2011. Synthesis and electrochemical, electrochromic and electrical properties of novel s-triazine bridged trinuclear Zn(II), Cu(II) and Lu(III) and a tris double-decker Lu(III) phthalocyanines. *Synthetic Metals,* 161, 13:14, 1245-1254.

26. Koca, B., Hamuryudan, E., Catak, S., Erdoğmuş, A., Monari, A., Aviyente, V. 2019. Exploring the Photophysics of Polyfluorinated Phthalocyanine Derivatives as Potential Theranostic Agents. *Journal of Physical Chemistry C*, 123, 40, 24417-24425.

27. Chauke, V., Durmuş, M., Nyokon, T. 2007. Photochemistry, photophysics and nonlinear optical parameters of phenoxy and tert-butylphenoxy substituted indium (III) phthalocyanines. *Journal of Photochemistry and Photobiology A: Chemistry* 192 (2-3), 179-187.

28. Sen, P., Managa, M., Nyokong, T. 2019. New type of metal-free and Zinc(II), In(III), Ga(III) phthalocyanines carrying biologically active substituents: Synthesis and photophysicochemical properties and photodynamic therapy activity. *Inorganica Chimica Acta*, 491, 1-8.

Celal Bayar University Journal of Science

Polyvinyl Alcohol-Corn Starch-Lemon Peel Biocomposite Films as Potential Food Packaging

Pınar Terzioğlu[1]* (iD), Fatma Nur Parın[1] (iD)

[1]Bursa Technical University, Faculty of Engineering and Natural Sciences, Department of Polymer Materials Engineering, Bursa, TURKEY
*pinar.terzioglu@btu.edu.tr
*Orcid: 0000-0003-4114-7044

Abstract

In this study, novel biocomposite films were prepared by incorporating lemon peel to a polyvinyl alcohol-starch matrix. The influence of the lemon peel content on the structural, mechanical, and optical properties of biocomposite films was discussed. The FT-IR studies revealed the formation of a strong interaction between the lemon peel and polymer matrix. Blending with lemon peel led to an improvement in the UV-light barrier properties of the polyvinyl alcohol-starch films. The incorporation of 1 wt% lemon peel further enhanced the mechanical properties of the films due to good compatibility and bonding between peel particles and polymer matrix. The results showed that lemon by-product has great potential to be evaluated into added-value products for packaging applications.

Keywords: Biodegradable polymer, *citrus* by-product, composite films, organic filler.

1. Introduction

Food packaging sector plays a significant role in the global polymer market. The most widely used polymer packaging materials are produced from non-renewable petroleum sources. Therefore, sustainable production requirements are increasing day by day due to growing consumption and environmental concerns [1].

Polyvinyl alcohol (PVA) is one of the most used biodegradable polymers in the packaging industry. It has unique properties as film-forming ability, biodegradability, high resistance to oil and solvents, and gas (O_2) barrier properties [2]. However, PVA has a relatively high price [3]. PVA is convenient for blending with natural polymers due to being highly polar and soluble in water [4]. Polyvinyl alcohol and starch blends are stand out due to being more economical, showing excellent compatibility with each other, and enhanced biodegradability features [5]. The reinforcement of the PVA/starch matrix with natural fibers or powders can further improve the mechanical properties of these materials [6]. Therefore, the investigations towards the development of green polymer composites via efficiently evaluating natural lignocellulosic by-products because of their renewable, environmentally-friendly, inexpensive, and non-toxic nature have shown an increasing trend [6]. Previous

studies reported the utilization of different food industry by-products as organic fillers or reinforcing agents in packaging systems. Apple pomace [7], banana peel [8], mangosteen rind [9], pomegranate peel [10], tomato pomace [11] has been successfully used to develop biocomposite films. Lemon (*Citrus limon* L.) peel is also an agro-industrial solid residue resulting from the lemon juice processing industry. Annual worldwide lemon production is estimated at over 4 200 000 tons [12]. The peels generate about 50-65 % of the fresh lemon weight [13,14]. Only a small quantity of lemon peel has been used as food additives [15], while most are usually discarded. Lemon peel contains many crude fibers as well as pectin, bioactive compounds, and carbohydrates [16]. The use of lemon peel in packaging appears as an interesting inexpensive alternative.

Currently, there is no report about the incorporation of lemon peel as filler in PVA/starch-based biocomposite films. Additionally, glycerol and citric acid were chosen as plasticizers that are widely used compounds in the food industry. Recently, there is an increasing trend to use citric acid in polymer film preparation which naturally occurs in fruits as the main organic acid [17]. Citric acid can effectively enable esterification reaction with hydroxyl groups of the PVA/starch blend due to having three carboxylic groups and one hydroxyl per monomer. It provides both crosslinking and plasticizing

effect to enhance the features of the composite film. Furthermore, the use of glycerol together with citric acid can enhance the film flexibility [18]. In this way, PVA/starch biocomposite films with better functional properties can be developed with the incorporation of citric acid and glycerol.

The principal goal of this work was the evaluation of the structural, mechanical, and optical properties of PVA/starch based packaging materials containing waste lemon peels. The films were characterized by Fourier transform infrared spectroscopy (FT-IR) and Ultraviolet-Visible (UV-VIS) spectroscopy. Mechanical properties of the composite films were evaluated in terms of tensile strength, Young's modulus, and p**2.3.2.** elongation. **2.3.3.**

2. Materials and Methods
2.1. Materials

Polyvinyl alcohol (average molecular weight; 30.000, 95.4% purity, 87.16% hydrolysis degree, 24.9 r**2.3.4.** viscosity) was obtained from Zag Kimya (TURKEY). Corn starch and citric acid were obtained from Güneş Company and Aksu Company (TURKEY), respectively. Glycerol was purchased from Merck (Darmstadt, GERMANY). Lemon peel was purchased from Naturelka (Aydın, TURKEY). The lemon peel was sieved using a steel mesh sieve (<200 μm).

2.2. Preparation of biocomposite films

The five different composite films were prepared by solution casting method according to the ratios given in Table 1. The film solutions were prepared by dissolving 8% (w/v) PVA in distilled water under magnetic stirring (700 rpm) overnight at 90°C. Separately, 2% (w/v) corn starch was gelatinized at 95°C for 15 minutes. Next, gelatinized corn starch was added to the PVA solution and continuously stirred at 70°C for an hour. The solution was then cooled to 50°C followed by the addition of citric acid (10%, w/w of total po**2.3.5.** weight) as a plasticizer and stirred for 10 mi **2.3.6.** Following the addition of glycerol as a plasticizer at a constant concentration (20%, w/w of total polymer weight), the stirring was continued for another 10 minutes. Then, Tween 80 (50μL) was added as a surfactant to the mixture and stirred for 10 minutes. Finally, the lemon peel with concentrations from 1% to 8% (w/w of total polymer weight) was added to the film solutions. The prepared film solution (35 mL) was cast

onto the glass petri dishes (12 cm) and dried in an oven at 40°C for 24 hours. PVA/Corn starch film-forming solution without lemon peel was used to produce a control film.

2.3. Characterization of biocomposite films
2.3.1. Thickness of films

The film thickness was measured by a digital caliper (ABS ASİMETO, Turkey). Measurements were randomly taken at three locations on each specimen. The results were expressed as the mean of measurements.

2.3.2. Fourier-transform infrared spectroscopy

Fourier-transform infrared (FT-IR) spectra of the composite films were recorded on a Thermo Scientific Nicolet i550 spectrometer between 4000 and 500 cm^{-1} wavelengths.

2.3.3. UV-VIS spectrophotometric analysis

The optical properties of the PVA/starch/lemon peel films were measured by UV-VIS-NIR Shimadzu UV-3600 device (Shimadzu, Japan). Each film sample cut into square and placed into the spectrophotometer cell. Percent transmittance was taken at the selected wavelength between 200 and 800 nm. Three replicates of each sample were applied.

The transparency and opacity of the films calculated using equation 2.1 and 2.2, respectively as given by Cazon et al. (2020) [19]:

$$\text{Transparency} = \frac{\log(\%T_{600})}{x} \quad \textbf{(2.1)}$$
$$\text{Opacity} = \frac{Abs_{500}}{x} \quad \textbf{(2.2)}$$

where %T_{600}=the percent transmittance, Abs_{500}=the absorbance at 500 nm, and x=film thickness (mm).

2.3.4. Mechanical properties

The mechanical properties of neat PVA/starch and PVA/starch/lemon peel composite films were measured by Universal Tensile Test Machine (Shimadzu-AGS-X, Japan) and the tests were performed according to ASTM D882, rectangular strips were prepared for each film, the samples were clamped and deformed under 1 kN load cell and crossheads peed set at 15 mm/min.

Table 1. The formulations of composite films.

Sample Code	PVA (w/v %)	Starch (w/v %)	Lemon peel (wt.% of total polymer)	Glycerol (wt.% of total polymer)	Citric acid (wt.% of total polymer)
L0	8	2	0	20	10
L1	8	2	1	20	10
L2	8	2	2	20	10
L3	8	2	4	20	10
L4	8	2	8	20	10

3. Results and Discussion
3.1. Film thickness

Film thickness is an important parameter that affects the barrier, optical, and mechanical properties of films [4]. The thickness of films varied from 0.29 to 0.35 mm (Table 2). In general, the films containing 4 wt. % and 8 wt. % lemon peel were slightly thicker than the other samples. The increment of film thickness with the incorporation of lemon peel could be because of the increase in solid content in films. A similar result was reported by Gaikwad et al. (2016) [7] that the addition of apple pomace increased the thickness of polyvinyl alcohol bio-composite films. The thicknesses of the prepared PVA/Corn starch/Lemon peel composite films were homogeneous indicating the good compatibility of the selected matrix materials.

Table 2. Thicknesses of PVA/Corn starch/Lemon peel biocomposite films.

Sample	Thickness (mm)
L0	0.29±0.01
L1	0.29±0.01
L2	0.29±0.01
L3	0.30±0.01
L4	0.35±0.02

3.2. FT-IR analysis of the biocomposite films

FT-IR spectra of the composite films are shown in Figure 1. A wide absorption centered around 3280 cm^{-1} represents the stretching vibration of O–H as hydrogen-bonded hydroxyl groups related to the absorbed moisture in the films. The presence of asymmetric CH_2 methyl group stretch/stretching vibration is observed at 2938 cm^{-1} [20]. The band at 1712 cm^{-1} is the characteristic peak of the C=O stretching vibration peak due to the ester bond and carboxyl groups in citric acid [20]. The peak at 1420 cm^{-1} is attributed to the CH_2 bending with deformation [21]. The mixed bending modes of CH and OH groups and attributed to the associated alcohols were observed at 1373 cm^{-1} [22]. The deformation vibration of the CO groups occurred at 1330 cm^{-1} [21]. The peak at 1241 cm^{-1} due to the wagging vibration of CH groups [22]. The stretching vibration of CO bond in C-O-H was observed at 1088 cm^{-1} [23]. The peak at 1024 cm^{-1} assigned to C–O stretching of the glucose ring [24]. The rocking vibration of CH_2 groups appeared at 919 cm^{-1} [22]. The band occurs at 844 cm^{-1} related to C-C groups stretching vibrations and out of plane bending vibration of OH groups [22].

The addition of lemon peel slightly weakened the intensities of 2938, 1342, 1024, 944 and, 919 cm^{-1} absorption bands. The peak at 919 and 842 cm^{-1} in the pure PVA-starch film also shifted to 922 and 845 cm^{-1} in the PVA/starch/lemon peel composite films, respectively. This was attributed to the formation of new hydrogen bonds between the PVA, starch, and lemon peel.

3.3. Optical analysis of the biocomposite films

The optical characteristics including color, transparency, opacity, and desired light-blocking ability of film materials are significant quality parameters [25]. These factors are important in view of consumer's acceptance and expanding the shelf life of packed products [19].

The light barrier properties of the biocomposite films by the percentage transmittance in the UV region (200-400 nm), and the VIS region (400-800 nm) are given in Figure 3. It is clear that the transmittance decreased with increasing lemon peel concentration in the polymer matrix in the UV-A (320-400 nm), UV-B (280-320 nm), and UV-C (190-280 nm) region, as shown in Figure 3. The lemon peel incorporated films were slightly yellowish. The L4 sample (8 wt. % lemon peel) significantly lowered the transmittance of the
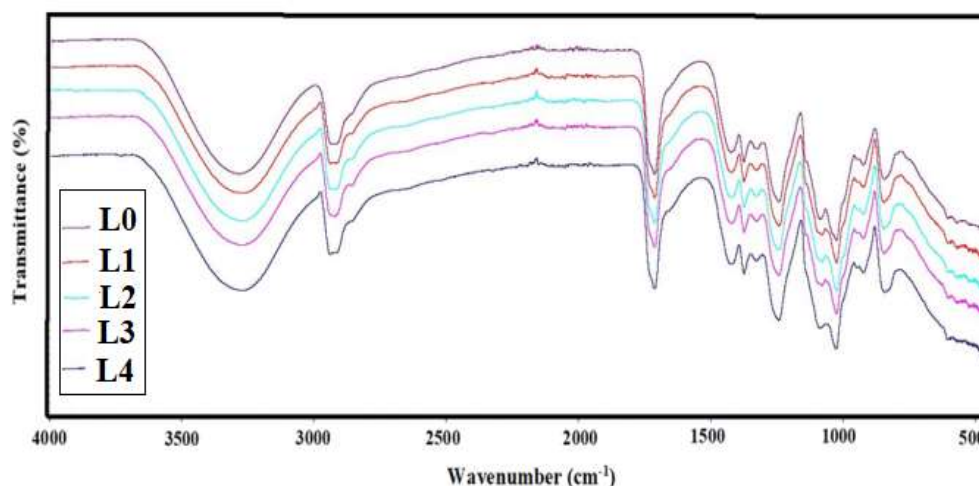
Figure 1. FT-IR spectra of PVA/Corn starch/Lemon peel biocomposite films

al Bayar University Journal of Science
ume 16, Issue 4, 2020, p 373-378
:10.18466/cbayarfbe.761144

P. Terzioğlu
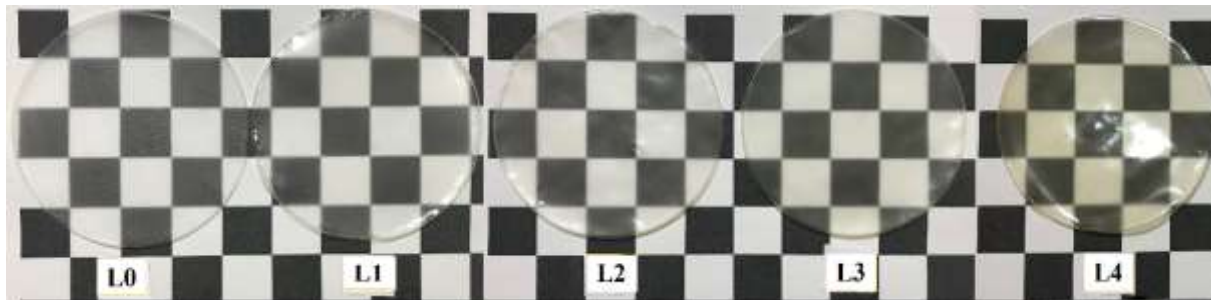
Figure 2. Visual appearances of PVA/Corn starch films containing different lemon peel contents.
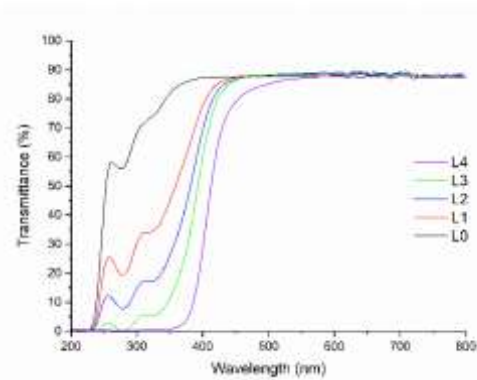
Figure 3. UV–VIS spectra profiles of the biocomposite films.
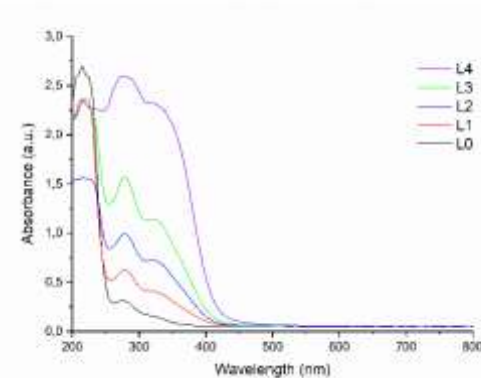
Figure 4. Absorbance spectra of PVA/Corn starch/Lemon peel biocomposite films.

PVA/starch film which was also apparent in the digital photographs of the composite films (Figure 2). The results showed that produced films would help to prohibit oxidative deterioration of packed food due to exposure to visible light. This result was supported by the study of Hanani et al. (2019) [10] who reported the effect of pomegranate (Punicagranatum L.) peel powder on the color of fish gelatin films.

The light absorbance of composite films is shown in Figure 4. The biocomposite films exhibited a strong absorption peak around 280 nm. The absorbance values of films were increased with the increase of the lemon peel content in UV-A (320-400 nm) and UV-B (280-320 nm) region. According to the absorbance results,

less light could pass through the lemon peel incorporated biocomposite films.

Table 3 presents the transparency and opacity results of the lemon peel incorporated biocomposite films with the effect of the blend ratio.

Table 3. Transparency and opacity values of the biocomposite films.

Sample	Transparency	Opacity
L0	6.71±0.01	0.18±0.01
L1	6.71±0.01	0.18±0.01
L2	6.71±0.01	0.18±0.01
L3	6.54±0.02	0.20±0.01
L4	5.55±0.01	0.19±0.01

The transparency and opacity results of the films ranged from 5.55 to 6.71 and 0.18 to 0.20, respectively. The 4 wt. % and 8 wt. % lemon peel incorporated PVA/starch films had lower transparency and higher opacity when compared to other films. Therefore, it can be concluded that the addition of the lemon peel at these concentrations into the PVA/starch matrix significantly enhanced the light barrier properties.

3.4. Mechanical analysis of the composite films

Mechanical properties are important parameters to obtain information about the stiffness, brittleness, and ductility of the biocomposites [26]. Tensile testing was conducted to examine the effect of blending with lemon peel on the mechanical properties of PVA/starch-based biocomposite films. The results are presented in Table 4 and Figure 5. The tensile strength of pure PVA/starch film (L0) increased from 24.35 ± 1.2 to 25.11 ± 1.3 MPa with the incorporation of 1 wt% lemon peel (L1). However, the tensile strengths of the films were decreased with further increment of lemon peel concentration. This might be attributed to the slight aggregation of lemon peel at higher concentrations and voids formation within the polymer matrix resulted in cracks at the biocomposite interface [27]. It could be due to the availability of surface hydroxyl groups of this lignocellulosic waste which tended to agglomerate easily by forming hydrogen bonds. In further studies, the surface modification of lemon peel should be evaluated to enhance dispersibility in the polymer

matrix and interfacial interaction of the matrix/filler at higher concentrations [28]. Similar to the tensile strength result, the elongation at break of pure PVA/starch film was 260.18 ± 13.00 % and has been increased to 275.19 ± 13.8 % with blending 1 wt. % lemon peel. The good dispersion of lemon peels and strong interfacial interaction might improve the ability to deliver external stress transfer from the PVA/starch matrix to lemon peel particles which leads to enhancement of both elongation at break and tensile strength [29]. With the increase of lemon peel concentration in the range of 2-8 wt. % in the polymer matrix, the elongation at break of the films was decreased because of the improvement in the stiffness of three-dimensional network by incorporation of filler [26]. In another study, the tensile strength and % elongation of PVA/starch/barley husk films were also reduced with the increase in barley husk content from 1 to 2% [30].

When compared with pure PVA/starch film, the biocomposite with lower lemon peel contents (1 and 2 wt. %) indicated a slightly decreased Young's modulus.

Table 4. Mechanical properties of biocomposite films.

Sample	Tensile strength (MPa)	Elongation at break (%)	Young'smodulus (MPa)
L0	24.35 ± 1.2	260.18± 13.0	56.33 ± 2.8
L1	25.11 ± 1.3	275.19 ± 13.8	52.70 ± 2.6
L2	22.52 ± 1.1	215.85± 10.8	51.26 ± 2.6
L3	20.03 ± 0.9	199.91 ± 10.0	59.46± 2.9
L4	17.72 ± 0.9	211.78 ± 10.6	71.82 ± 3.6
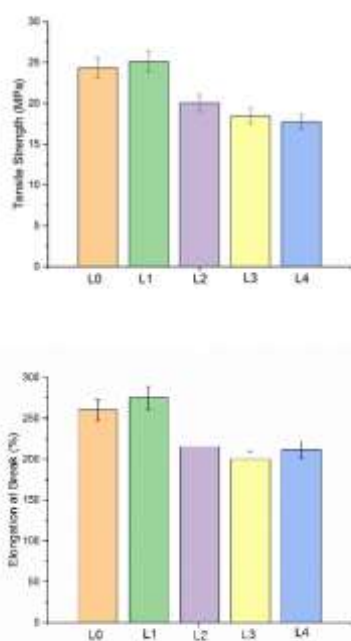
Figure 5. Tensile strength and elongation at break of biocomposite films.

However, when lemon peel content increased from 2 to 4 wt. %, Young's modulus was increased from 51.26 ± 2.6 to 59.46 ± 2.9 MPa. The highest Young's modulus was observed for the L4 sample which was containing the highest amount of lemon peel (8 wt. %).

4. Conclusion

A new approach was developed to add value to lemon peel by a cost-effective way to obtain functional packaging materials. A series of PVA/corn starch/lemon peel biocomposite films were successfully prepared using a solution blending method in the presence of glycerol and citric acid. UV-VIS results showed that the optical barrier properties of lemon peel incorporated PVA/starch films against UV-radiation enhanced with the increase of the lemon peel concentration. The mechanical properties of the films improved at the appropriate incorporation of lemon peel. Reduction in tensile strength and elongation at break were observed with the addition of lemon peel in the range of 2-8 wt. %. The lemon peel incorporated PVA/corn starch films with desirable performance can be taken into consideration as a sustainable and environmentally-friendly material alternative to the traditional packaging applications.

Author's Contributions

Pınar Terzioğlu: Drafted and wrote the manuscript, performed the experiment, supervised the characterization progress and interpreted the results.

Fatma Nur Parın: Performed the characterization studies and helped in manuscript preparation.

Ethics

There are no ethical issues after the publication of this manuscript.

References

1. Crizel, TM, Rios, AO, Alves, VD, Bandarra, N, Moldao-Martins, M, Flores, SH, 2018. Active food packaging prepared with chitosan and olive pomace. *Food Hydrocolloids*; 74: 139-150.

2. Mathew, S, Jayakumar, A, Kumar, VP, Mathew, J, Radhakrishnan, EK. 2019. One-step synthesis of eco-friendly boiled rice starch blended polyvinyl alcohol bionanocomposite films decorated with in situ generated silver nanoparticles for food packaging purpose. *International Journal of Biological Macromolecules*; 139: 475-485.

3. Abral, H, Hartono, A, Hafizulhaq, F, Handayani, D, Sugiartic, E, Pradipta, O. 2019. Characterization of PVA/cassava starch biocomposites fabricated with and without sonication using bacterial cellulose fiber loadings. *Carbohydrate Polymers*; 206: 593-601.

4. Marvdashti, LM, Koocheki, A, Yavarmanesh, M. 2017. Alyssum homolocarpum seed gum-polyvinyl alcohol biodegradable composite film: Physicochemical, mechanical, thermal and barrier properties. *Carbohydrate Polymers*; 155: 280-293.

al Bayar University Journal of Science
ume 16, Issue 4, 2020, p 373-378
:10.18466/cbayarfbe.761144

P. Terzioğlu

5. Srivastava, KR, Singh, MK, Mishra, PK, Srivastava, P. 2019. Pretreatment of banana pseudostemfibre for green composite packaging film preparation with polyvinyl alcohol. *Journal of Polymer Research*; 26: 95.

6. Mittal, A, Garg, S, Bajpai, S. 2020a. Fabrication and characteristics of poly (vinyl alcohol)-starch-cellulosic material based biodegradable composite film for packaging application. Materials Today: Proceedings; 21: 1577–1582.

7. Gaikwad, KK, Lee, JY, Lee, YS. 2016. Development of polyvinyl alcohol and apple pomace bio-composite film with antioxidant properties for active food packaging application. *Journal of Food Science and Technology;* 53(3): 1608–1619.

8. Kumar, T, Rajini, N, Alavudeen, A, Siengchin, S, Rajulu A, Ayrilmis N. (2019). Development and Analysis of Completely Biodegradable Cellulose/Banana Peel Powder Composite Films. *Journal of Natural Fibers.* doi: 10.1080/15440478.2019.1612811.

9. Zhang, X, Liu, J, Yong, H, Qin, Y, Liu, J, Jin, C. 2019. Development of antioxidant and antimicrobial packaging films based on chitosan and mangosteen (Garciniamangostana L.) rind powder. *International Journal of Biological Macromolecules;* doi: 10.1016/j.ijbiomac.2019.10.038.

10. Hanani, ZAN, Yee, FC, Nor-Khaizura, MAR. 2019. Effect of pomegranate (Punicagranatum L.) peel powder on the antioxidant and antimicrobial properties of fish gelatin films as active packaging. *Food Hydrocolloids*; 89: 253-259.

11. Aloui, H, Baraket, K, Sendon, R, Silva, AS, Khwaldia, K. 2019. Development and characterization of novel composite glycerol-plasticized films based on sodium caseinate and lipid fraction of tomato pomace by-product. *International Journal of Biological Macromolecules*; 139: 128-138.

12. Boluda-Aguilar, M, López-Gómez, A. 2013. Production of bioethanol by fermentation of lemon (Citrus limon L.) peel wastes pretreated with steam explosion. *Industrial Crops and Products*; 41: 188–197.

13. Jagannath, A, Biradar, R. 2019. Comparative Evaluation of Soxhlet and Ultrasonics on the Structural Morphology and Extraction of Bioactive Compounds of Lemon (Citrus limon L.) Peel. *Journal of Food Chemistry and Nanotechnology*; 5(3): 56-64.

14. Simeone, GDR, Di Matteo, A, Rao, MA, Di Vaio, C. 2020. Variations of peel essential oils during fruit ripening in four lemon (Citrus limon (L.) Burm. F.) cultivars. *Journal of the Science of Food and Agriculture;* 100: 193–200.

15. El-ghfar, MHAA, Ibrahim, HM, Hassan, IM, Fattah, AAA, Mahmoud, MH. 2016. Peels of Lemon and Orange as Value-Added Ingredients: Chemical and Antioxidant Properties. *International Journal of Current Microbiology and Applied Sciences;* 5(12): 777-794.

16. Papoutsis, K, Pristijono, P, Golding, JB, Stathopoulos, CE, Scarlett, CJ, Bowyer, MC, Vuong, QV. 2016. Impact of different solvents on the recovery of bioactive compounds and antioxidant properties from lemon (Citrus limon L.) pomace waste.*Food Science and Biotechnology;* 25(4): 971-977.

17. Park, HR, Chough, SH, Yun, YH, Yoon, SD. 2005. Properties of Starch/PVA Blend Films Containing Citric Acid as Additive.*Journal of Polymers and the Environment*; 13(4): 375-382.

18. Das, A, Uppaluri, R, Das, C. 2019. Feasibility of poly-vinyl alcohol/starch/glycerol/citric acid composite films for wound dressing applications.*International Journal of Biological Macromolecules*; 131:998-1007.

19. Cazón, P, Vázquez, M, Velázquez, G. 2020. Regenerated cellulose films with chitosan and polyvinyl alcohol: Effect of the moisture content on the barrier, mechanical and optical properties. *Carbohydrate Polymers;* 236: 1160312.

20. Mustafa, P, Niazi, MBK., Jahan, Z, Samin, G, Hussain, A, Ahmed, T, Naqvi, SR. 2019. PVA/starch/propolis/anthocyanins rosemary extract composite films as active and intelligent food packaging materials, *Journal of Food Safety*; 12725 doi: 10.1111/jfs.12725.

21. Gulati, K, Lal, S, Arora, S. 2019. Synthesis and characterization of PVA/Starch/CMC composite films reinforced with walnut (Juglansregia L.) shell flour. *SN Applied Sciences;* 1: 1416, doi: 10.1007/s42452-019-1462-8.

22. Popescu, MC, Dogaru, BI, Goanta, M, Timpu, D. 2018. Structural and morphological evaluation of CNC reinforced PVA/Starch biodegradable films. *International Journal of Biological Macromolecules*; 116: 385–393.

23. Chen, Y, Cao, X, Chang, PR, Huneault, MA. 2008. Comparative study on the films of poly(vinyl alcohol)/pea starch nanocrystals and poly(vinyl alcohol)/native pea starch. *Carbohydrate Polymers*; 73: 8–17.

24. Priya, B, Gupta, VK, Pathania, D, Singha, AS. 2014. Synthesis, characterization and antibacterial activity of biodegradable starch/PVA composite films reinforced with cellulosic fibre. *Carbohydrate Polymers*; 109: 171-179.

25. Kochkina, NE, Butikova, OA.2019. Effect of fibrous TiO_2filler on the structural, mechanical, barrier and optical characteristics of biodegradable maize starch/PVA composite films. *International Journal of Biological Macromolecules;* 139: 431-439.

26. Mathew, S, Jayakumar, A, Kumar, VP, Mathew, J, Radhakrishnan, EK. 2019. One-step synthesis of eco-friendly boiled rice starch blended polyvinyl alcohol bionanocomposite films decorated with in situ generated silver nanoparticles for food packaging purpose. *International Journal of Biological Macromolecules;*139: 475-485.

27. Gulati, K, Lal, S, Diwan, PK, Arora, S. 2019. Investigation of thermal, mechanical, morphological and optical properties of polyvinyl alcohol films reinforced with buddha coconut (Sterculiaalata) leaf fiber. *International Journal of Applied Engineering Research and Development;* 14(1): 170-179.

28. Wang, G, Yang,X, Wang,W.2019. Reinforcing Linear Low-Density Polyethylene with Surfactant-Treated Microfibrillated Cellulose.*Polymers*; 11:441.

29. Wu, H,Xiao, D,Lu, J, Li, T, Jiao, C,Li, S, Lu, P,Zhang, Z. 2020. Preparation and Properties of Biocomposite Films Based on Poly(vinyl alcohol) Incorporated with Eggshell Powder as a Biological Filler. *Journal of Polymers and the Environment;* 28: 2020–2028.

30. Mittal, A, Garg, S, Bajpai, S. 2020. Thermal decomposition kinetics and properties of grafted barley husk reinforced PVA/starch composite films for packaging applications. *Carbohydrate Polymers;* 240: 116225.

Celal Bayar University Journal of Science

Thermal Degradation Kinetics of Ascorbic Acid and Some B-Complex Vitamins in Black Mulberry (*Morus nigra*) Juice

Cemre Sernikli[1] , Çetin Kadakal[1*]

[1] Pamukkale University, Faculty of Engineering, Food Engineering Department, 20160, Kınıklı, Denizli, Turkey
*ckadakal@pau.edu.tr
*Orcid: 0000-0002-6608-3887

Abstract

In this paper, L-ascorbic acid, thiamine (vitamin B_1), riboflavin (vitamin B_2) and niacin (vitamin B_3) thermal degradations depending on different thermal treatment times (0, 5, 10, 15, 20, 25 and 30 min) and temperatures (70, 80, 90 and 95°C) were investigated and results were presented. Firstly, black mulberry juice was obtained from fresh black mulberry fruits and then thermal treatment was carried out. L-ascorbic acid, thiamine, riboflavin and niacin were analyzed by using HPLC method with 25 min separation time. L-ascorbic acid, thiamine, riboflavin and niacin thermal degradation followed first order kinetic model during thermal treatments. Particularly, increment in temperature from 80°C to 90°C significantly increased rate constants of compounds. Activation energy, which indicates temperature dependence of reaction, was calculated using Arrhenius equation. Activation energies were found to be 58.5 kJ mol^{-1}, 40.5 kJ mol^{-1}, 45.9 kJ mol^{-1} and 52.1 kJ mol^{-1} between 70°C and 95°C for ascorbic acid, thiamine, riboflavin and niacin, respectively. L-ascorbic acid, thiamine, riboflavin and niacin thermal degradation in black mulberry juice was investigated for the first time. Thus, this study will be beneficial for future studies.

Keywords: Ascorbic acid, B-complex vitamins, black mulberry, HPLC, kinetic

1. Introduction

The black mulberry (*Morus nigra*) is a member of Moraceae family and its native countries are India, China and Japan [1]. It also grows especially well in the north America and Africa [2].

Black mulberry is regarded as a source of bioactive compounds. The main importance of black mulberry is its high content of total phenolics, total flavonoids, and vitamin C [3] and nutritional values of protein, carbohydrates, fat, fiber, mineral matter (particularly calcium, iron, phosphorus) and water-soluble vitamins (thiamine, riboflavin, nicotinic acid and ascorbic acid) [4]. Black mulberries have been used as a medicine (expectorant, hypoglycemic, anthelmintic, laxative, emetic, odontalgic and warming agents) since prehistoric times [5]. In addition, black mulberry fruits have antioxidant, anti-inflammatory and antimicrobial properties with the contain of various phytochemicals including phenolics [6].

Because of its physiological, nutritional and technological properties, black mulberry fruits have great importance. The black mulberry has sweet and pleasant taste. It is a fruit that is difficult to be harvested, transported and marketed due to its soft texture and its short-term deterioration. For this reason, the fruit is mostly consumed as processed [7]. Turkey is an important country in term of traditional and indigenous food production techniques. Evaluation form of black mulberry consists of raw, dried or processed foods such as pekmez, juice, marmalades, liquors, pestils and komes [7, 8].

Vitamins are essential organic compounds for human and animal bodies in terms of body resistance, biochemical functions and growing. Water-soluble and fat-soluble vitamins are different subgroups of vitamins. Studies on determining the vitamin values of black mulberry juice are very limited. Fruit maturity, harvest time, storage conditions and duration, pre-consumption cooking etc. affect the vitamin content of fruit [9]. As known, vitamins can degrade during processing and storage of foods because of chemical reactions.

Quantitative analysis of vitamins has great importance for manufacturers due to their essential role in nutrition and their relative instability [10]. For separation of vitamins, HPLC is suggested method with solid phase extraction because of removing interfering components [11].

Determination of kinetic properties of quality parameters is important to maintain the highest level of quality in new food process designs [12]. Therefore, prediction of probable quality changes in foods can be provided by determining kinetic properties of quality parameter [13]. No study on HPLC determination of thiamine (TH), riboflavin (RB), niacin (NC) and degradation of L-ascorbic acid (LAA), TH, RB and NC in black mulberry juice (BMJ) are current in the literature. The aim of this study is a) to determine loss of LAA, TH, RB and NC during thermal treatments at different temperatures b) to define kinetic properties of thermal degradation of LAA, TH, RB and NC such as reaction order, rate constant of reaction, activation energy, half-life and Q_{10}.

2. Materials and Methods
2.1. Material

The fresh black mulberry fruits were provided from Gümüssu Food Co., a well-established local factory in Gümüshane province in Turkey. Nearly 300 kilograms of fresh black mulberries taken from the factory were transported to the Department of Food Engineering at Pamukkale University, Denizli, Turkey by refrigerated vehicles and processed for BMJ.

2.2. Production of BMJ

The black mulberry fruit is first washed in water in a clean container and removed dirt, leaves and foreign materials. After grounding by a fruit grinder (Model KMS6000, Vestel), extraction of raw black mulberry juice was done in a cloth bag by using a hydraulic press (Bucher-Guyer AG, Niederweningen, Switzerland). Black mulberry juice, obtained after pressing of the mulberries were filtered through a filter (25 µm pore size) and the filtered juice was then added into pyrex tubes (a three-necked round bottom flask, 75 x 10 mm ID) for the thermal processing and kept at 4 °C till the thermal treatment.

2.3. Thermal Treatment

Temperatures were selected as 70, 80, 90 and 95 °C for the thermal treatment. 25 ml of BMJ samples added into pyrex tubes and heated by placing in thermostatic water bath (Model 3047, Kottermann, Hänigsen/Germany). After the temperature of samples reached the desired temperature, the application time is started. In all heating treatment, reaching the desired temperature took less than 10 minutes. To prevent evaporation, the tubes were tightly capped and placed in a thermostatic water bath. Juice samples were removed from the water bath at regular time intervals (0, 5, 10, 15, 20, 25 and 30 min) and then were rapidly cooled in an ice water. LAA, TH, RB and NC were determined by sampling with test tubes filled with BMJ from water bath at 5 minutes intervals. Sampling was carried out in triplicate. All experiments and calculating the reaction rate constants of each temperature were performed in triplicate.

2.4. Selection of Temperatures and Heating Periods

The lowest temperature is 70°C for the industrial production of BMJ and concentrates. However, bottled BMJ are kept in boiling water for 20-30 minutes in traditional production. Therefore, temperature of bottled BMJ can reach to 95°C.

2.5. Analysis of Water-Soluble Vitamins
2.5.1. Equipment

The HPLC apparatus (Shimadzu Corporation, Kyoto, Japan) used in the study consisted of a PDA detector (Model SPD-M10 AVP, Shimadzu), a pump (Model LC-10AT-VP, Shimadzu), a column oven (Model CTO-10ASVP, Shimadzu) and a degasser (Model DGU 14A, Shimadzu). The peak areas were analyzed by using Shimadzu Software Program. The column for separation was reversed-phase C18 (15 cmx4.6 mm ID, 5µm particle size, Cat. No: 504955) and provided from SUPELCO (Bellefonte, PA, USA). Also, injection volume to HPLC was 20 µL of the samples and performed by using a micro syringe.

2.5.2. Reagents

Doubly distilled and deionized water was used in the experiments. Methanol (HPLC grade) and potassium dihydrogen phosphate (extra pure) was purchased from Merck (Darmstadt, Germany). LAA, TH, RB and NC analytical standards were provided from Sigma (Sigma-Aldrich Chemie GmbH, Deisenhofen-Germany) and stock standards were prepared in mobile phase. Linear calibration curves (r^2=0.999) involving five point were prepared by plotting concentration (g ml^{-1}) versus peak area (mAU) for each compound. Following then sonication, stock standards were transferred to amber glass to prevent light damage and stored under refrigeration.

2.5.3. Sample Preparation (Solid Phase Extraction=SPE)

Due to chromatographic interference of many components of black mulberry with LAA, TH, RB and NC, a SPE cartridges (Sep-Pak C18, 500 mg) were used to remove components which cause interfering. 20 g of deionized water added into 5 g of BMJ. After homogenization, centrifugation of homogenate was

carried out at 9x103 rpm for 10 min (Model 2-16, Sigma Bioblock Scientific). A method suggested by Cho, Ko, and Cheong [11] was used for SPE extraction of LAA, TH, RB and NC with slight modifications. To activate stationary phase, 10 ml of pure water at 4.2 pH and 10 ml of methanol were mixed and added into SPE as flushing liquid. After the activation of stationary phase, the black mulberry juice (10 mL) was loaded. 0.005 M HCl solution was used for pH adjustment of acidified water. The elution of samples was performed with 5 ml of acidified water and 10 ml of methanol with 1 ml min of flow rate. Following that, eluents were collected and evaporated to dryness. The mobile phase was used to dissolve the residue and the residue was filtered through a 0.45 μm microfilter (Schleicher & Schuell, Darmstadt-Germany). 20 μl of filtered sample was injected to HPLC.

2.6. Methods

Detection wavelengths of LAA, TH, RB and NC were selected as 265, 234, 266 and 261 nm for the monitoring of column elution, respectively. After degassing by sonication, mobile phase was filtered through 0.45 μm filter. The mobile phase consisted of methanol (90:10) and 0.1 mol L^{-1} potassium dihydrogen phosphate (pH: 7) and 0.7 ml min^{-1} was the flow rate. 20 μl of the samples was injected into the system and the column temperature was 25 °C (room temperature). Concentrations of the LAA, TH, RB and NC were calculated using integrated areas of the corresponding standards and the samples.

2.7. Recovery of Water-Soluble Vitamins

Determining the recovery was carried out adding three additional levels of standard LAA, TH, RB and NC into the BMJ samples containing known amounts of LAA, TH, RB and NC. Therefore, two determinations were performed with two replicates for each addition level.

2.8. Calculation of Kinetic Parameters

General equation for degradations of food components can be written as given below [14]:

$$-\frac{d[C]}{dt} = k[C]^m \qquad (2.1)$$

[C]: concentration of the compound
m: reaction order
k: rate constant of reaction.

Thermal degradation of LAA, TH, RB and NC in BMJ followed first-order kinetic model. First order kinetic model (Eq. 2.2) is described by integrating of Eq. (2.1).

$$\ln\left(\frac{[C]_t}{[C]_0}\right) = -kt \qquad (2.2)$$

C_0: the initial LAA, TH, RB and NC
C_t: the residual LAA, TH, RB and NC
k: rate constant of reaction (min^{-1})
t: time (min)

Arrhenius equation (Eq. 2.3) was used to describe temperature dependence of LAA, TH, RB and NC.

$$k = k_0 \times e^{-Ea/RT} \qquad (2.3)$$

k_0: factor of frequency (min^{-1}),
E_a: activation energy (kJ mol^{-1})
T: absolute temperature (K),
R: universal gas constant (8,314 x 10^{-3} kJ $mol^{-1}K^{-1}$).

Quotient indicator (Q_{10}) expresses temperature-dependence of reaction rate and calculated with Eq. (2.4):

$$Q_{10} = \left(\frac{k_2}{k_1}\right)^{\frac{10}{T_2-T_1}}_0 \qquad (2.4)$$

T: temperature,
k_1: rate constants of LAA, TH, RB and NC degradation at temperatures T_1
k_2: rate constants of LAA, TH, RB and NC degradation at temperatures T_2

The time required for the initial concentration to be halved is calculated by the following equation 2.5, given below:

$$t_{1/2} = 0.693/k \qquad (2.5)$$

Where k is the reaction rate constant (per min).

2.9. Further Determinations

Total solid (%), water soluble solid (Bx), pH and total acidity (dry citric acid) was measured by using the Method of Association of Official Analytical Chemists [15]. the Lane-Eynon method was used for the determining the amount of total sugar in the BMJ [16].

2.10. Statistical Analysis

All data were statistically evaluated by using "Statistical Analysis Systems" of SAS® software [17]. Statistical significance differences were considered at the level of $p < 0.05$

3. Results and Discussion

Studies on the LAA content of black mulberry and its products have been frequently published but limited studies on TH, RB, NC content and their changes during processing are current in the literature. Degradation kinetics of LAA, TH, RB and NC with HPLC determination in BMJ were investigated for the first time. Thus, contribution of this study is critical for the literature.

Chemical components have a wavelength giving maximum absorbance. Therefore, LAA, TH, RB and NC were sensitively determined by setting detector at specific wavelength that give maximum absorbance. As

seen from Figure 1, LAA, TH, RB and NC were separated well by isocratic elution within 25 min. Unknown peaks in the chromatogram were detected but no interfering with LAA, TH, RB and NC.
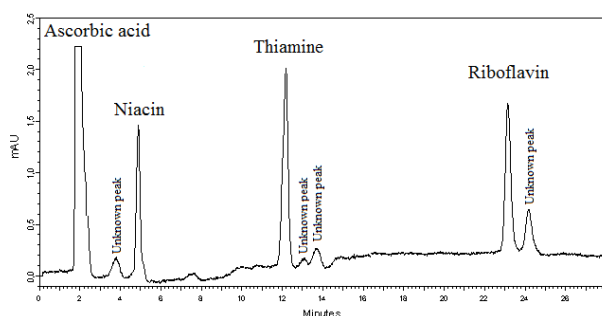
Figure 1. Chromatographically separated LAA, TH, RB and NC by isocratic elution.

3.1. Analytical Characteristic of the HPLC Method
3.1.1. Linearity, Detection Limit, Recovery and Precision

Detection limit, linearity of standard curve, recovery and precision of proposed method for determination of LAA, TH, RB and NC in BMJ is shown in Table 1. The "R^2" values of LAA, TH, RB and NC were determined

as 0.9992, 0.9996, 0.9989 and 0.9990, respectively. Coefficients of determinations (r^2) were determined above 99.74% for LAA, TH, RB and NC. The detection limits of LAA, TH, RB and NC were calculated with "S/N" (signal/noise) of 3 [18] and found to be 0.1, 0.01, 0.01 and 0.01 mg/l, respectively. Standard addition procedure was used for recovery experiments to determine the reliability of the method. In this context, recovery experiments were performed by adding standard solution of LAA, TH, RB and NC, whose contents were 50, 0.1, 0.2 and 0.5 mg/L, respectively, to the samples. Recovery values of LAA, TH, RB and NC in BMJ were calculated as 96.6±0.5%, 97.2±0.5%, 93.9±0.7% and 103.2±1.0%, respectively. The precision of the method was determined under the same conditions (apparatus and reagents) with triplicate experiments. Calculation of precision was done by applying intra- and inter-day tests and the results were given as relative standard deviation (*RSD*, %). Low *RSD* values indicate good precision for HPLC. *RSD* values of LAA, TH, RB and NC were found to be as 0.6%, 2.8%, 3.6% and 2.1%, respectively.

Table 1. Linearity of standard curve, detection limit, recovery and precision of the proposed method for determination of AA, TH, RB and NC in BMJ.

Vitamin	Linear range (mg/L)	*R*	*r²*	Detection limit (mg/L)	Initial content (mg/L)	Content after addition (mg/L)[a]	Recovery (%) Mean SD[b]	Precision R.S.D. (%)
L Ascorbic acid	5.0-250.0	0.9992	99.67	0.1	34.50	82.8±0.34	96.6±0.5	0.6
Thiamine	1.0-50.0	0.9996	99.93	0.01	0.124	0.221±0.016	97.2±0.5	2.8
Riboflavin	1.0-40.0	0.9989	99.83	0.01	0.212	0.399±0.010	93.9±0.7	3.6
Niacin	1.0-20.0	0.9990	99.84	0.01	0.524	1.04±0.010	103.2±1.0	2.1

a50 mg for ascorbic acid, 0.1 mg for thiamine, 0.2 mg for riboflavin and 0.5 mg for niacin   bMean ± standard deviation

3.2. Characteristics of BMJ Samples Used

The characteristics of the BMJ used in the study are as follows: 16.15 % total solid, 15.15 Bx soluble solid, 3.4 pH value, 0.35 % total acidity, 11.50 % total sugar, 34.50 mg/l LAA, 0.124 mg/l TH, 0.212 mg/l RB and 0.524 mg/l NC. Soluble solid, total acidity and pH values of BMJ were reported between 11.55-19.04°Brix, 1.37-2.24 g/100ml in citric acid equivalent and 3.63-4.18, respectively [19]. Snapyan et al. [20] studied the physiochemical properties of BMJ and reported that it contained ascorbic acid (15.4 mg/100g), thiamine (0.49 µg/ml) and niacin (19.05 µg/ml). Okatan [21] reported the highest value of vitamin C as 31.34 mg/100g in mulberry genotypes collected from natural resources of Uşak province. In addition, 15.37 mg/100g LAA, 0.040 mg/100g RB and 1.60 mg/100g NC content (fresh weight basis) in black mulberry (*Morus nigra*) fruits [22] and 30 g/100g LAA, 0.04 mg/100 g TH and

0.08 mg/100 g RB content in mulberry fruits were reported [23].

3.3. Kinetic Parameters of LAA, TH, RB and NC Thermal Degradation in BMJ

Thermal stability of LAA, TH, RB and NC in BMJ were studied at 70, 80, 90 and 95 °C. The initial LAA, TH, RB and NC contents determined by HPLC were 34.50 mg/l, 0.124 mg/l, 0.212 mg/l and 0.524 mg/l, respectively and their concentrations highly decreased during the 30 min heating periods of 95 °C, with the reductions of 38.70%, 51.61%, 46.70% and 41.41%, respectively. On the other hand, 30 min heating periods of 70 °C in BMJ resulted with the reductions of 12.61%, 22.60%, 20.30% and 16.22% for LAA, TH, RB and NC, respectively.

Ç.Kadakal

Degradations of LAA, TH, RB and NC in BMJ during thermal treatment were presented in Figure 2. As understood from Figure 2, first-order kinetic model was found to be the most suitable kinetics model to describe degradations of these compounds. Based on the increment in temperature and time, degradations of LAA, TH, RB and NC increased. Determination coefficients of LAA, TH, RB and NC degradations at each constant temperature based on time were found to be over 0.98 for first-order kinetic model. This indicates a linear relation between natural logarithm of LAA, TH, RB and NC concentrations and time. Degradations of quality parameters may follow zero or first-order reactions, but differences may be insignificant between zero and first-order reactions [14]. On the other hand, no studies on degradation kinetics of LAA, TH, RB and

NC in BMJ are current in the literature. The results of this study were compared with degradations of these compounds in other foods. Likewise, it was reported by Karhan, Aksu, Tetik, and Turhan [24] that ascorbic acid degradation in rosehip pulp was fitted to first-order kinetic model at different temperatures. Moreover, Rekha, Singhal, and Pandit [25] reported that degradation of thiamine in red gram splits (*Cajanus cajan L.*) follows first-order kinetic model at different pH values (4.5, 5.5 and 6.5) and temperature ranging from 50 to 120°C. Additionally, Mulley, Stumbo and Hunting [26] notified that degradations of vitamins in foods and model systems under different conditions are fitted to first-order kinetic model.
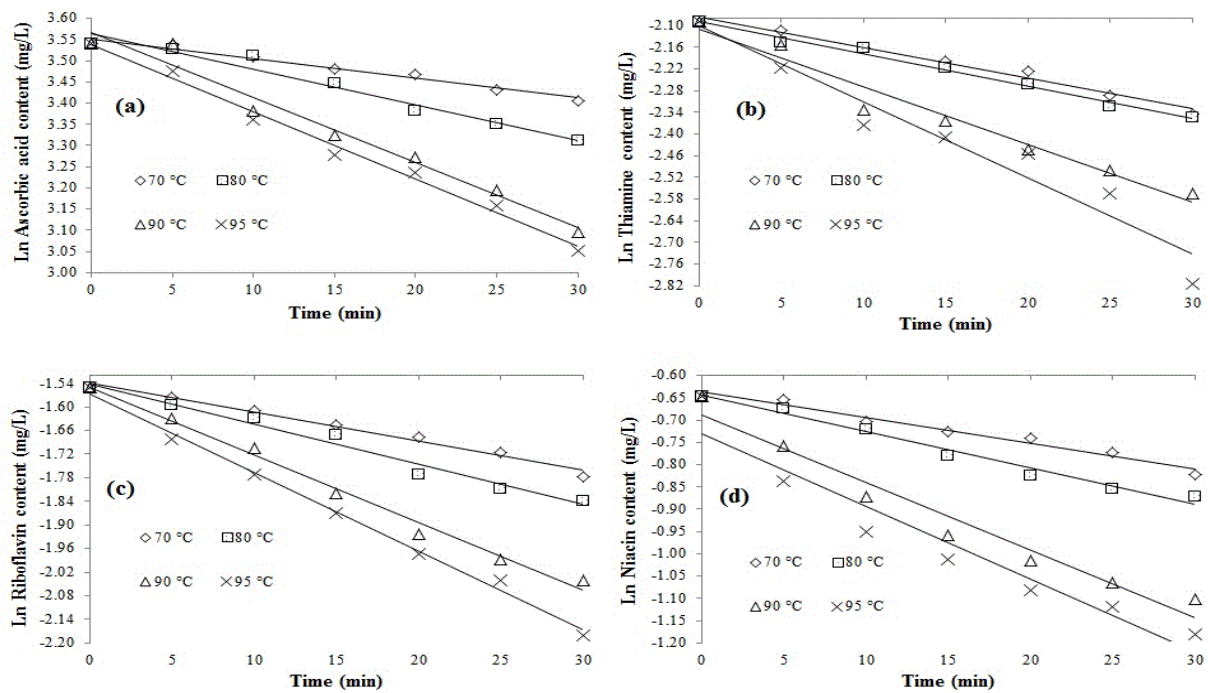
Figure 2. First order degradation kinetics of **(a)** LAA, **(b)** TH, **(c)** RB and **(d)** NC during thermal treatment.

Kinetic parameters of thermal degradation of LAA, TH, RB and NC in BMJ were listed in Table 2. The rate constants of LAA, TH, RB and NC increased depending on the increment in temperature. This result indicates that LAA, TH, RB and NC degrade as temperature-dependent. The lowest degradation rate constant was obtained from LAA, followed NC, RB and TH. This shows that LAA is less thermal sensitive in comparison to NC, RB and TH. Also, temperatures rising from 70 to 80 and 80 to 90°C were found to be more effective on the rate constant of LAA than from 90 to 95°C. On the contrary, while a slight increasing in rate constants of TH, RB and NC at 70-80°C and 90-95°C temperature range was observed, the highest increment in rate constants of TH, RB and NC was determined at 80-90°C

temperature range. The k values of LAA, TH, RB and NC varied between 4×10^{-3}-15×10^{-3}, 8×10^{-3}-21×10^{-3}, 7×10^{-3}-20×10^{-3} and 5×10^{-3}-16×10^{-3} over the temperature range of 70-95 °C, respectively (Table 2). In conclusion, it was observed that thermal treatment and time have great effect on degradation of LAA, TH, RB and NC. Increment in temperature and time caused a rapid degradation in LAA, TH, RB and NC. Combs [27] notified that stability of LAA is higher at acidic medias when compared to alkaline or neutral medias. Several studies on thermal stability of RB are current in various foods and model systems. However, there are very limited data on thermostability of TH, RB and NC in fruit juice and no studies are current in BMJ.

As shown in Table 2, the half-life values (t$_{1/2}$) for LAA, TH, RB and NC decreased with the increment of temperature. It was observed that higher temperatures provide faster degradation of LAA, TH, RB and NC. Thermal stability of LAA was higher in comparison to TH, RB and NC due to having the highest t$_{1/2}$ values among the other components at the same temperatures.
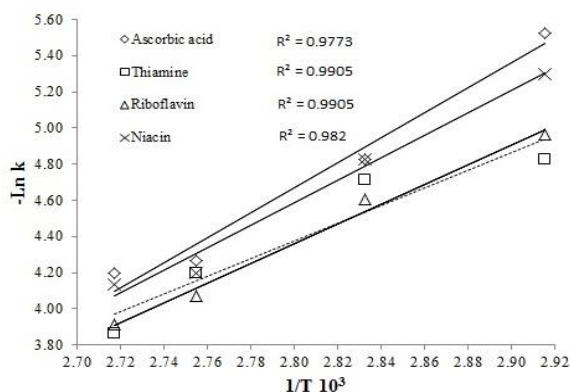
Figure 3. Arrhenius plots for degradation of LAA, TH, RB and NC in BMJ during heating.

Figure 3 shows Arrhenius type relation of LAA, TH, RB and NC during thermal treatment. Arrhenius equation explains relation between degradation rate constants and temperature. If the natural logarithms of the degradation rate constants are plotted vs absolute temperature, a linear curve is obtained. Ea can be calculated by means of the slope of the linear curve. It was found that activation energies (E_a) of LAA, TH, RB and NC degradation in BMJ differ by temperature (70-95°C). The highest activation energies were obtained from LAA, NC, RB and TH, respectively.

When compared to NC, TH and RB, thermal stability of LAA is higher. Sensitivity of a reaction to temperature change can be explained with activation energy. Higher activation energy indicates higher sensitivity. Therefore, LAA, TH, RB and NC degraded more at 95°C than 70°C. The activation energy of LAA was calculated as 58.5 kJ mol^{-1}. When comparing to other reports, activation energies of heated rosehip (70-95°C), raspberry (60-90°C) and citrus juice were reported to be 47.5 kJ mol^{-1}, 15.7 kJ mol^{-1} and 35.9 kJ mol^{-1}, respectively [24, 28, 29]. The activation energy of LAA was found to be higher than those reports. On the contrary, the activation energy of LAA was lower than 115.5 kJ mol^{-1} for orange juice [30] and 81.67 kJ mol^{-1} for pomegranate juice [31].

Table 2. Kinetic parameters of LAA, TH, RB and NC in BMJ.

Vitamin	T (°C)	k 10^3 (min^{-1})	t$_{1/2}$ (min)	Q$_{10}$ 70-80 °C	Q$_{10}$ 80-90 °C	Q$_{10}$ 90-95 °C	E$_a$ (kJ mol^{-1})
Ascorbic acid	70	4	173.3				
	80	8	86.6				
	90	14	49.5	2.00	1.75	1.15	58.5
	95	15	46.2				
Thiamine	70	8	86.6				
	80	9	77.0	1.13	1.67	1.96	40.5
	90	15	46.2				
	95	21	33.0				
Riboflavin	70	7	99.0				
	80	10	69.3	1.43	1.70	1.38	45.9
	90	17	40.8				
	95	20	34.7				
Niacin	70	5	138.6				
	80	8	86.6	1.60	1.88	1.14	52.1
	90	15	46.2				
	95	16	43.3				

Q_{10} values of vitamin degradation in BMJ were presented in Table 2. Q_{10} values were found to be different for each 10°C temperature increment. The temperature ranges of 70 to 80 ºC, 90 to 95 ºC, 80 to 90 ºC and 80 to 90 ºC were observed for the highest Q_{10} values of LAA, TH, RB and NC, respectively. As understood from this result, these temperature ranges significantly affected the degradations of these compounds. For example, when compared to other temperature ranges, Q_{10} values of LAA and NC were lower at the range of 90-95°C and very close. This indicates that degradation of LAA and NC was slightly affected by the temperature change in this range. The results could not be compared with literature since no data on this subject are current. However, comparison between Q_{10} values of LAA, TH, RB and NC in BMJ and other fruits was made. Karhan, Aksu, Tetik and Turhan [23] reported that Q_{10} value of LAA in the rosehip was 1.21 during thermal treatment under anaerobic conditions.

4. Conclusion

Degradation of examined compounds fit the first-order kinetics. Degradation rate of LAA, TH, RB and NC increased with the increment of heating time and the temperature. The best temperature of long-term heating of black mulberry juice was found as 70°C for less loss of LAA, TH, RB and NC. Results of this study may be benefit for the BMJ producing industry for prevent the loss of examined for water-soluble vitamins which are important quality parameters. Therefore, designing a thermal treatment with a high retention of water-soluble vitamins may be easier when the degradation kinetics of LAA, TH, RB and NC is known.

Acknowledgement

Author's Contributions

Cemre Sernikli: Performed the experiments, wrote the manuscript.
Çetin Kadakal: Performed the model, design of the experiments, statistical analysis, wrote the manuscript.

Ethics
There are no ethical issues after the publication of this manuscript.

References

1. Dinçer, C, Tontul, I, Topuz, A. 2016. A comparative study of black mulberry juice concentrates by thermal evaporation and osmotic distillation as influenced by storage. *Innovative Food Science and Emerging Technologies*; 38:57–64.

2. Lim, S.H, Choi, C.I. 2019. Pharmacological properties of *Morus nigra* L. (Black Mulberry) as a promising nutraceutical resource. *Nutrients;*11:437.

3. Khalid, N, Fawad, AS, Ahmed, I. 2011. Antimicrobial activity, phytochemical profile and trace minerals of black mulberry (*Morus nigra* L.) fresh juice. *Pakistan Journal of Botany*; 43:91-96.

4. Venkatesh, KP, Chauhan, S. 2008. Mulberry: Life enhancer. *Journal of Medicinal Plants Research;* 2:271-278.

5. Gungor, N, Sengul, M. 2008. Antioxidant activity, total phenolic content and selected physicochemical properties of white mulberry (Morus alba L.) fruits. *International Jurnal of Food Properties*; 11:44–52.

6. Gecer, MK, Akin, M, Gundoğdu, M, Eyduran, SP, Ercişli, S, Eyduran, E. 2016. Organic acids, sugars, phenolic compounds, and some horticultural characteristics of black and white mulberry accessions from Eastern Anatolia. *Canadian Journal of Plant Science*; 96:27–33.

7. Okatan, V, Polat, M, AŞKIN, MA. 2016. Some physico-chemical characteristics of Black mulberry (Morus nigra L.) in Bitlis. *Scientific Papers-Series B, Horticulture;* 60:27-30.

8. Boranbayeva, T, Karadeniz, F, Yılmaz, E. 2014. Effect of storage on anthocyanin degradation in black mulberry juice and concentrates. *Food and Bioprocess Technology*; 7:1894–1902.

9. Yang, CST, Atallah, WA. 1985. Effect of four drying methods on the quality of intermediate mouisture lowbush, bluberries. *Journal of Food Science*; 50:1233-1237.

10. Kadakal, C, Duman, T, Ekinci, R. 2017. Thermal degradation kinetics of ascorbic acid, thiamine and riboflavin in rosehip (Rosa canina L) nectar. *Food Science and Technology;* 38:667-673.

11. Cho, CM, Ko, JH, Cheong, WJ. 2000. Simultaneous determination of water-soluble vitamins excreted in human urine after eating an overdose of vitamin pills by a HPLC method coupled with a solid phase extraction. *Talanta*; 51:799–806.

12. Van Boekel, MA. 2008. Kinetic modeling of food quality: a critical review. *Comprehensive Reviews in Food Science and Food Safety;* 7: 144-158.

13. Van Boekel, MAJS. 2008. Kinetic Modeling of Reactions in Foods. 1st ed. CRC Press, London.

14. Labuza, TP, Riboh, D. 1982. Theory and application of Arrhenius kinetics to the prediction of nutrients losses in foods. *Food Technology*; 36:66–74.

15. Association of Official Analytical Chemists – AOAC. 1990). *Official methods of analysis of AOAC International* (15th ed.). Arlington: AOAC.

16. Cemeroglu, B. 1992. Basic Analysis Methods in Fruit and Vegetable Processing Industry. 1st ed. Biltav Press, Ankara.

17. SAS®_ Institute Inc. – SAS. (1985). *SAS user's guide. Statistics*. Cary: SAS.

385

Ç.Kadakal

18. Li, HB, Chen, F. 2000. Determination of silicate in water by ion exclusion chromatography with conductivity detection. *Journal of Chromatography A*; 874:143-147.

19. Erkaleli, ZÖ, Dalkılıç, Z. 2016. Determination of morphological, phenological and pomological characterization of black mulberry (Morus nigra L.) grown in Ulubey vicinity, Usak province. *Journal of Adnan Menderes University Agricultural Faculty*; 13:89-106.

20. Snapyan, GG, Mınasyan, SM, Astabasyan, GA, Chencenko, ZA, Khachatryan GV, Khodzumyan, GA, Akopyan, AA, Gevorkyan, VG. 1981. Biochemical indices and technological properties of mulberries. *Konsevnaya-i ovoshchesushil'naya promyshlennost*; 6:35-36.

21. Okatan, V. 2018. Phenolic compounds and phytochemicals in fruits of black mulberry (Morus nigra L.) genotypes from the Aegean region in Turkey. *Folia Horticulturae*; 30:93-101.

22. Imran, M, Khan, H, Shah, M, Khan, R, Khan, F. 2010. Chemical composition and antioxidant activity of certain Morus species. *Journal of Zhejiang University-Science B (Biomedicine & Biotechnology)*; 11:973-980.

23. Iqbal, M, Khan, KM, Jilani, MS, Khan, MM. 2010. Physico-chemical characteristics of different mulberry cultivars grown under agro-climatic conditions of Miran Shah, North Waziristan (Khyber Pakhtunkhwa) Pakistan. *Journal of Agricultural Research*; 48:209-217.

24. Karhan, M, Aksu, M, Tetik, N, Turhan, I. 2004. Kinetic modeling of anaerobic thermal degradation of ascorbic acid in rose hip (*Rosa Canina L*) pulp. *Journal of Food Quality*; 27:311-319.

25. Rekha, PN, Singhal, S, Pandit, AB. 2003. A study on degradation kinetics of thiamine in red gram splits (Cajanus cajan L.). *Food Chemistry*; 85:591-598.

26. Mulley, EA, Stumbo, CR, Hunting, WM. 1975. Kinetics of thiamin degradation by heat. Effects of pH and form of the vitamin on its rate of destruction. *Journal of Food Science*; 40: 989-992.

27. Combs, GF. 2008. The Vitamins: Fundamental Aspects in Nutrition and Health. 3rd ed. Elsevier Academic Press, London.

28. Summen, MA, Erge, HS. 2014. Thermal degradation kinetics of bioactive compounds and visual color in raspberry pulp. *Journal of Food Processing and Preservation*; 38:551-557.

29. Dhuique-Mayer, C, Tbatou, M, Carail, M, Caris-Veyrat, C, Dornier, M, Amiot, MJ. 2007. Thermal degradation of antioxidant micronutrients in citrus juice: kinetics and newly formed compounds. *Journal of Agricultural Food Chemistry*; 55:4209-4216.

30. Johnson, JR, Braddock, RJ, Chen, CS. 1995. Kinetics of ascorbic acid loss and nonenzymatic browning in orange juice serum: Experimental rate constants. *Journal of Food Science*; 60:502–505.

31. Paul, R, Ghosh, R. 2012. Effect of thermal treatment on ascorbic acid content of pomegranate juice. *Indian Journal of Biotechnology*; 11:309-313.

Celal Bayar University Journal of Science

Effects of Detergents, Ions, and Organic Solvents on the Activity of Four *Bacillus clausii* Pectinases

Sevinç Berber[1] iD, Serap Çetinkaya[1*] iD

[1] Department of Molecular Biology and Genetics, Science Faculty, Sivas Cumhuriyet University, 58140 Sivas, Turkey.
*serapcetinkaya2012@gmail.com
*Orcid: 0000-0001-7372-1704

Abstract

Four different pectinolytic enzyme activity essays were employed to detect different pectinases of *Bacillus clausii* from an extracellular protein cocktail. The mixture was obtained by ethanol precipitation. Dinitrosalicylic acid (DNS) and sodium hydroxide (NaOH) titrimetric methods were used for the pectinase assays. Each of the essays produced a positive result, indicating the presence of pectate lyase (PGL), pectin lyase (PL), pectin methyl esterase (PME), and polygalacturonase (PG). Activities of these enzymes were then assessed at differing concentrations of NaCl, detergents (SDS and tweens), ion chelators, and organic solvents. Results, presented as histograms, were the indication of original findings, as most of them were new to the relevant literature.

Keywords: *Bacillus clausii*, ionic strength tolerance, organic solvent tolerance, pectinase activity, salt tolerance.

1. Introduction

The walls of growing plant cells are called primary cell walls and about 90% are composed of polysaccharides [1]. The plant cell wall is a barrier that protects plants against microbial infections. This barrier contains cellulose, hemicellulose, lignin and pectin polysaccharides. Pectin has a heterogeneous structure and gives rigidity to the cell wall by cross-linking polysaccharides [2]. At the same time, these bonds are thought to limit cell growth and reduce biodegradability [3].

Depolymerisation and esterification of polysaccharides in the cell wall is carried out by extracellular enzymes. Pectinases are a group of enzymes involved in the breakdown of pectin, a complex polysaccharide found in the primary cell wall and in the middle lamellae of higher plant tissues. After pectin is broken down by pectinases, it first enters the periplasmic space and then the cytoplasm [4]. Pectic degradation products regulate the physiological responses and gene expression of plants [1]. Phytopathogenic species such as *Erwinia* cause softening and rotting, especially in plant roots [2]. This explains the phytotoxicity mechanism of pectic fragments [1].

Aspergillus, *Erwinia*, and *Penicillium* species were mainly used in pectinase production. In the last fifteen years, *Bacillus*, *Fusarium*, *Kluyveromyces*, *Rhizopus*, and *Saccharomyces* have also been studied. Selection of microbial sources for pectinase production is generally based on the culture conditions, the number and type of pectinase produced, the pH, and the thermal stability of the enzymes [5].

In today's fruit juice production, pectinases play a key role in the breakdown of cell walls, colour compounds, and aroma essences. Thus, thanks to pectinases, it has become possible to obtain high quality concentrated products. In addition, pectinases are used effectively in many other industrial areas such as textile, fibre processing, paper making, waste water treatment, animal feed preparation, tea and coffee production, and oil extraction [6-8]. It is estimated that microbial pectinases have a 25% share in the world food enzyme market [9].

This study was performed to gain an insight into the catalytic capacity of crude alkaline pectinolytic enzymes of *Bacillus clausii* in harsh environment where organic solvents, detergents or high concentrations of ions were present.

2. Material and Methods
2.1 Isolation and identification of *Bacillus clausii*

For the bacterial source, Koyulhisar (Sivas, Turkey) apple orchard soil samples were used. The isolates obtained were identified at the species level by partial protein- (mass spectrometry) and 16S rRNA gene sequence analysis [10,11].

2.1.1 Identification of bacteria by mass spectrometry

Colonies grown in Horikoshi-I agar at 37°C by 24 h incubation were used in the analysis. The colonies grown in the plate were treated with the solution used in the MALDI-TOF device and compared with the partial protein profiles in the library of the device and the original spectrum results were recorded [11].

2.1.2 16S rRNA gene sequencing

PCR- and DNA sequencing conditions have been described in an earlier article [11].

2.2 Screening of pectinase activity

Soil samples were inoculated onto two separate agar media, containing polygalacturonic acid and pectin. Agar plates were incubated for three days at 37°C. Gram iodine solution was dropped onto individual colonies and waited for 5 minutes. Zone formation was examined. As another method, 1% CTAB solution was dropped and zone formation was examined. Zones around the colony indicate the presence of pectinase activity.

2.3 Preparation of crude enzyme

Liquid Horikoshi-I medium was inoculated with bacteria and an overnight culture was obtained at 37°C. After the incubation, cells were pelleted by centrifugation for 10 min at 5,000 rpm at +4°C. Onto the culture supernatant 0.5, 0.6, 0.75, 1.0, 1.25, 1.75 or 2 volumes cold 95% ethanol were added and total protein content was precipitated cold ethanol and kept at -20°C overnight. Then the proteins were collected by centrifugation at 5000 rpm at +4°C for 15 minutes. Ethanol was removed at room temperature.

2.4 Enzyme identification

Polygalacturonase (PG) activity was assayed by DNS method [12,13]. Enzyme activity was calculated as μmol galacturonic acid released per minute.
Pectin lyase (PL) assay relied on the absorbance of double bonds formed in the pectin substrate at 235 nm. The activity was calculated as the change of absorbance measured at 235 nm per minute [14].

Pectate lyase (PGL) activity was determined by reading the absorbance of double bonds formed in the pectin substrate at 235 nm. The activity was calculated as the change of absorbance measured at 235 nm per minute [15].

Pectin methylesterase (PME) activity was determined by monitoring and recording the pH change. The activity was calculated by measuring the amount of NaOH required to keep the pH constant during the reaction [13].

3. Results and Discussion
3.1 Identification of Pectinase-producing Bacteria

Fifty colonies isolated from the soil were grown in selective medium containing pectin and polygalacturonic acid.
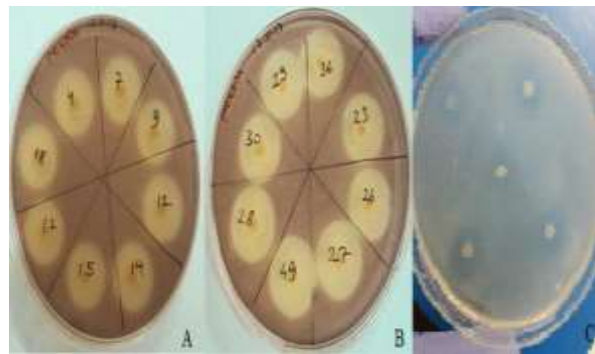
Figure 1. Detection of enzyme activity in the medium containing pectin.

After incubation (3 days at 37°C), 1% CTAB and iodine solution were dropped onto the colonies. About a third of the colonies (16:50) formed zones on both media (Figure 1,2).
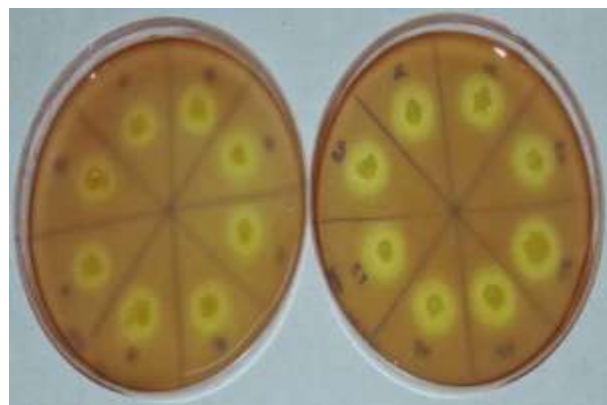
Figure 2. Detection of enzyme activity in media containing PGA.

Zones were visualised with iodine solution in the PGA medium containing agar plates. Zone formation was observed in all of the isolates.

3.2 Isolate identification

Morphological and partial biochemical characterization showed that the isolates were Gram-positive, catalase-negative, and rod-shaped bacteria (results not shown). One of the strains was selected for further studies.

Partial protein analysis was performed by MALDI-TOF mass spectrometry in the Department of Microbiology, Faculty of Medicine, Cumhuriyet University, and it was determined that all the isolates were *Bacillus clausii.*
A phylogenetic analysis based on 16S ribosomal RNA (rRNA) gene sequence comparison also showed that this strain belonged to *B. clausii*. The rRNA gene sequence was submitted to GenBank (Accession number: MT524963, GenBank).

3.3 Enzyme activity measurement
3.3.1 Effect of ionic strength

Effect of sodium chloride was investigated at differing NaCl concentration and under optimum pH and temperature points (Figure 3).
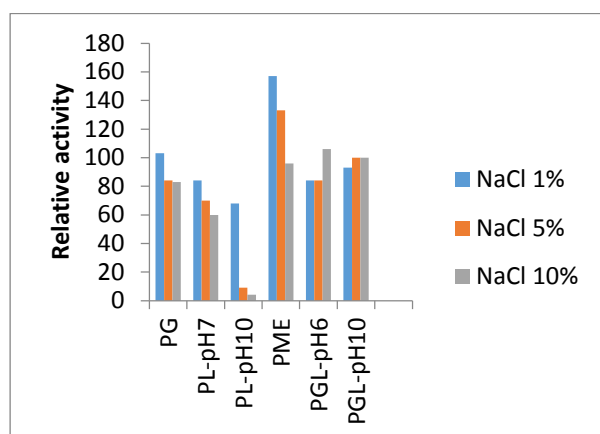
Figure 3. Effects of ionic strength.

Polygalacturonase (PG): 1% PGA and enzyme solutions containing NaCl in different concentrations were prepared. Activity measurements were performed under optimum conditions. Media without NaCl was used as a control group. The activity in the medium containing NaCl (1%) was determined to be the same as the control group. At 5% and 10% NaCl concentrations only 7% activity loss was observed (Figure 3).

Pectin lyase (PL): It was observed that there was 84% activity in the environment containing 1% NaCl at pH7, 70% activity in the environment containing 5% NaCl, and 60% activity in the environment containing 10% NaCl. At pH10, 68% activity was observed in the sample containing 1% NaCl, whereas in reactions containing 5% and 10% NaCl, the activity almost disappeared.

Pectate lyase (PGL): PGL activity was measured at pH6 and pH10 in reactions containing different NaCl concentrations. Although the activity was somewhat reduced in the sample containing 1% NaCl at both pH, values approaching the optimum activity were recorded in increasing NaCl concentrations (Figure 3).

Pectin methylesterase (PME): PME activity was measured in optimum conditions with different NaCl conditions. The activity was determined to be 157% in 1% NaCl, 133% in 5% NaCl and 96% in 10% NaCl (Figure 3).

3.3.2 Effect of organic solvents

Activities were measured in reaction media containing different organic solvents and under optimum conditions (Figure 4).
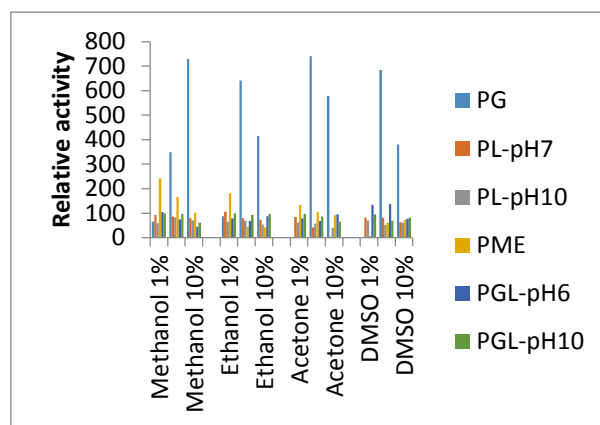
Figure 4. Effects of organic solvents.

Polygalacturonase (PG): 1%, 5% and 10% (v / v) methanol, ethanol, acetone and DMSO were added to the reaction medium to measure activity under optimum conditions. The group without organic solvent was used as a control. At a concentration of one percent, no significant loss of activity was observed in media containing methanol and ethanol, but no activity was recorded in media containing acetone and DMSO. In the medium containing five percent and ten percent organic solvents, an increase in activity was observed in all solvents compared to the control group (Figure 4).

Pectin lyase (PL): Since there were two different optimum pHs for PL, the effect of organic solvents on both pHs was investigated. It was determined that in the reactions containing 1% ethanol at pH 7, the relative activity increased by 6%. Loss of activity was observed in all other organic solvents at higher concentrations. It was shown that the enzyme was almost completely inhibited at a concentration of 10% of acetone (Fig. 4). In samples containing 1% and 10% methanol at pH10, 35% and 30% activity losses were observed, while 17% activity loss was observed in the environment containing 5% methanol. (Figure 4).

Pectate lyase (PGL): The effect of organic solvents on PGL activity was investigated at pH6 and pH10. It was observed that the activity decreased at pH6, at increasing concentrations of methanol. DMSO increased the activity at 1% and 5% concentrations and started to decrease at 10% concentration. Methanol also decreased the activity at increased concentrations. Ethanol and acetone reduced the activity at the concentrations of 1% and 5%, but led to a higher activity at 10% concentration. (Fig.4). Organic solvents did not significantly affect the activity at 1% concentration at pH10. Ethanol and DMSO reduced activity at 5%, but not at 10% concentration (Figure 4).

Pectin methylesterase (PME): The effect of organic solvents on PME activity at different concentrations was investigated under optimum conditions. While 1% methanol, ethanol, and acetone increased the activity, the activity appeared to decrease at higher concentrations. Surprisingly, however, DMSO inhibited the enzyme at 1% concentration, while increasing at higher concentrations (Figure 4).

3.3.3 Effects chemical reactifs

Activities were measured in reaction media containing different chemical reagents and under optimum conditions (Figure 5).
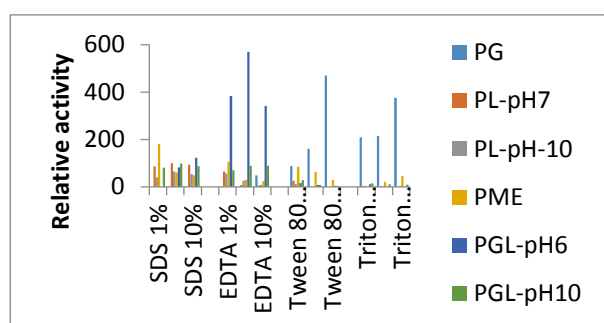
Figure 5. Effects of chemical reactifs.

Polygalacturonase (PG): Activities were measured at optimum conditions by adding SDS, EDTA, Tween-80 and Triton-X100 at 1%, 5% and 10% concentrations to the reaction medium. No activity was observed in samples containing SDS (1%) and EDTA (5%); however, increased activity was determined in reactions containing tween-80 and triton-X100. In samples containing ten percent chemical reagents, tween-80 and triton-X100 increased the activity. While EDTA inhibited the enzyme at 1% and 5% concentrations, a significant activity was observed at 10% concentration (Figure 5).

Pectin lyase (PL): As there were two different optimum pHs for PL, the effect of chemical reagents on both pHs was investigated. In the reactions containing 1% and 10% SDS at pH7, 14% and 7% activity loss was

observed, and no activity loss was observed at 5% SDS. Other chemicals decreased the activity at increasing concentrations. While Triton X100 almost completely inhibited the activity at pH10, 5% SDS caused only 35% loss of activity (Figure 5).

Pectate lyase (PGL): PGL activity was measured at pH6 and pH10. EDTA and 10% SDS increased the activity at pH6 (Fig. 5) and caused only a 10% decrease at pH10 (Fig. 5). Other chemical reagents were found to almost inhibit PGL at both pH points.

Pectin methylesterase (PME): The effect of chemical reagents on PME activity at different concentrations was investigated under optimum conditions. It was determined that the activity increased at 1% concentrations of both SDS and EDTA, but decreased at increasing concentrations. At higher concentrations Tween-80 inhibited the enzyme, but the activity increased at increasing concentrations of triton-X100 and there remained a 45% activity at 10% concentration (Figure 5).

Some of the examples of research involving Bacillus members can be summarised as follows:

Al-Rajabi and Mahasneh (1999) have studied pectin and pectate lyase activities isolated from Bacillus polymyxa strain [16]. It has been reported that 1mM EDTA in pectate lyase activity causes 48% reduction in nitrilotriacetate and 35% and 53% in pectin and pectate lyase activity, respectively.

Kashyap et al. (2000) have purified pectinase from the DT7 strain of Bacillus sp., using gel filtration and ion exchange chromatography. It has been stated that pectinase activity increased in the presence of 100mM CaCl2 and mercaptoethanol and that EDTA decreased the activity by 17% [17].

Joo et al. (2003) have shown that ta protease from the Bacillus clausii I-52 strain was stable in the presence of non-ionic surfactants such as Triton-X-100 and Tween-20, but also in strong anionic surfactant such as SDS [18]. A serine protease of Bacillus clausii has been used for the production of food additives within the regulations of FAO / WHO common food standards program (2010).

Mei et al. (2013) have isolated a pectinase from Bacillus halodurans M29 strain and cloned in E. coli JM109. It was determined that EDTA decreased the activity of this pectinase [19].

A pectinase of Bacillus circulans has been purified (Raju and Divakar, 2013). This enzyme appeared to have a maximum activity in Tween-80, and Tween-20 and SDS also increased its activity [20].

Sassi et al. (2016) have purified a polygalacturonase from a mutant strain Penicillium occitanis CT1. This enzyme was found to be highly active in the presence of Triton X-100, DTT, β-mercaptoethanol, urea, iodoacetamide, and iodoacetic acid, whereas EDTA and SDS cause a 20% and 10% decrease in its relative activity [21].

Madu et al. (2016) have purified a 38 kDa pectinase from Bacillus licheniformis and they have measured its relative activity at 1mM, 5mM and 10mM concentrations of NaCl. They have reported 127%, 117% and 98% relative activities respectively. Here again the enzyme activity decreased in 1mM and 5mM EDTA to 77% and 59%, respectively [22].

In a previous study, it has been shown that the pectinolytic enzymes of *B. clausii* reside in the alkaline side of the pH spectra. Thus these enzymes could be used in textile processing, in the degumming of plant fibres, in the treatment of pectic wastewaters, and in paper making.

4. Conclusions

Although studies with other species of *Bacillus* genus are frequently encountered in the literature, there is little information on the pectinases of *Bacillus clausii*, especially on pectin- and pectate lyases. In addition, *Bacillus clausii* is a probiotic species [23-26]. This makes it more interesting to understand its extracellular enzyme content. This study aimed at the discovery of pectinolytic enzymes of this probiotic species.

The study showed that specific activities of the enzymes of interest could be identified and assessed in an extracellular protein mixture. Its results could have strong biotechnological implications in industrial processes where the use of purified enzymes are unnecessary. As the producing organism was a probiotic bacterium, its crude extracellular products could directly be used. The work shed some light on some of the industrial properties of four pectinolytic enzymes produced by one isolate of *Bacillus clausii*.

Acknowledgement

Author's Contributions

Sevinç Berber: Performed the experiment and result analysis and helped in manuscript preparation.

Serap Çetinkaya: Conceived and designed research, conducted experiments, contributed new reagents or analytical tools, analyzed data, wrote the manuscript.

Ethics

There are no ethical issues after the publication of this manuscript.

Conflict of interest

The authors declare that they have no conflict of interest.

References

1. McNeil, M., Darvill, A.G., Fry, S.C. and Albersheim, P. 1984. Structure and Function of The Primary Cell Walls of Plants. *Annual Review of Biochemistry;* 53: 625-663.

2. Abbott, D.W. and Boraston, A.B. 2008. Structural Biology of Pectin Degradation by Enretobacteriaceae. *Microbiology and Molecular Biology Reviews;* 72: 301-316.

3. Vries, R.P. and Visser, J. 2001. Aspergillus Enzymes Involved in Degradation of Plant Cell Wall Polysaccharides. *Microbiology and Molecular Biology Reviews;* 65: 497-522.

4. Abbott, D.W. and Boraston, A.B**.** 2008. Structural Biology of Pectin Degradation by *Enretobacteriaceae*. *Microbiology and Molecular Biology Reviews*; 72: 301-316.

5. Khairnar, Y., Krishna, V.K., Boraste, A., Gupta, N., Trivedi, S., Patli, P., Gupta, G., Gupta, M., Jhadav, A., Mujapara, A., Joshi, B. and Mishra, D. 2009. Study of Pectinase Production in Submerged Fermentation Using Different Strains of *Aspergillus niger*. *International Journal of Microbiology Research*; 1: 13-17.

6. Hoondal, G.S., Tiwari, R.P., Tewari, R., Dahiya, N. and Beg, Q.K. 2002. Microbial Alkaline Pectinases and Their Industrial Applications: A Review. *Applied Microbiology Biotechnology*; 59: 409-418.

7. Kashyap, D.R., Vohra, P.K. Chopra, S. and Tewari, R. 2001. Applications of Pectinases in the Commercial Sector: A Review. *Bioresource Technology*; 77: 215-227.

8. Mojsov, K., 2012. Biotechnological applications of pectinases in textile processing and bioscouring of cotton fibers. *II International Conference Industrial Engineering and Environmental Protection Zrenjanin, Serbia,* 314-322.

9. Sharma, N., Rathore, M. and Sharma, M. 2012. Microbial Pectinase: Sources, Characterization and Applications. *Reviews in Environmental Science and Bio/Technology*; 12: 45-60.

10. Berber, S. 2018. Productıon, Isolatıon and Characterızatıon of Extracellular Pectinase from Soil Bacteria. Master's Thesis, *Cumhuriyet University Institute of Science;* Sivas, 21.

11. Berber, S. and Çetinkaya, S. 2020. An Isolate of *Bacillus clausii* Appears to Possess Four Distinct Pectinolytic Activities. *Iğdır University Journal of the Institute of Science;* 10, in press.

12. Kocabay, S. 2015. Producdution, Isolation and Characterization of Extracellular Amylase Enzyme from Gaıta Bacreria. Master's Thesis, *Cumhuriyet Üniversitesi Fen Bilimleri Enstitüsü*; Sivas, 96.

13. Whitaker, J.R. 1990. Microbial Pectolytic Enzymes. Microbial Enzymes and Biotechnology, Fogarty, W. M. ve Kelly, C. T. (Ed.), *Department of Industrial Microbiology, University College*, *Dublin*; 133-177,

14. Pickersgill, R.W. and Jenkins, J.A. 2003. The Structures and Active Sites of Pectinases. Advances in Pectin and Pectinase Research, Voragen, F., Schols, H. ve Visse, R. (Ed.), *Wageningen University, Netherlands*; 267-277.

15. Gummadi, S.N., Monaj, N. and Kumar, S. 2007. Structural and Biochemical Properties of Pectinases. Industrial Enzymes Structure, Function and Application, Polaina, J., MacCabe, A. P. (Ed.), *Instituto de Agroquimica y Technologia de Alimentos, Valencia*; 99-117.

16. Al-Rajabi, I.I. and Mahasneh, A.M. 1999. Partial Characterization of an Alkalophilic Extracellular Crude Pectinases From a *Bacillus polymyxa* Strain. *Qatar University Science Journal*; 18: 67-80.

17. Kashyap, D.R., Chandra, S., Kaul, A. and Tewari, R. 2000. Production, Purification and Characterization of Pectinase from a *Bacillus sp. DT7*. *World Journal of Microbiology and Biotechnology*; 16: 277-282.

18. Joo, H.S., Kumar, C.G., Park, G.C., Paik, S.R. and Chang, C.S. 2003. Oxidant and SDS-stable alkaline protease from *Bacillus clausii* I-52: Production and Some Properties. *Journal of Applied Microbiology*; 95: 267-272.

19. Mei, Y., Chen, Y., Zhai, R. and Liu, Y. 2013. Cloning, Purification and Bıchemical Properties of a thermostable Pectinase from *Bacillus halodurans M29*. *Journal of Molecular Catalysis B: Enzymatic*; 94: 77-81.

20. Raju, E.V.N. and Divakar, G. 2013. Production of Pectinase by Using *Bacillus circulans* Isolated From Dump Yards of Vegetable Wastes. *IJPSR*; 4: 2615-2622.

21. Sassi, A.H., Tounsi, H., Trigui-Lahiani, H., Bouzouita, R., Romdhane, Z.B. and Gargouri, A. 2016. A Low-Temperature Polygalacturonase from *P.occitanis*: Characterization and Application in Juice Clarification. *International Journal of Biological Macromolecules*; 91: 158-164.

22. Madu, O.J., Okonji, R.E., Torimiro, N. and Agboola, F.K. 2016. Purification and Characterization of Pectinase from *Bacillus licheniformis* obtained from a Cassava Waste Dump. *Journal of Advances in Biology*; 8: 1685-1695.

23. Ciffo, F. 1984. Determination of the spectrum of antibiotic resistance of "*Bacillus subtilis*" strains of enterogermina. *Chemioterapia;* 3: 45–52.

24. Cutting, S.M. 2011. *Bacillus* probiotics. *Food Microbiol.;* 28: 214–220.

25. Lippolis, R., Siciliano, R.A., Mazzeo, M.F., Abbrescia, A., Gnoni, A., Sardanelli, A.M. and Papa, S. 2013. Comparative secretome analysis of four isogenic Bacillus clausii probiotic strains. *Proteome Sci.;* 11: 28.

26. Urdaci, M., Bressollier, P. and Pinchuk, I. 2004. *Bacillus clausii* Probiotic Strains Antimicrobial and Immunodulatory Activities. *Journal of Clinical Gastroenterology*; 38: 86-90.

Celal Bayar University Journal of Science

Improved Jacobi Matrix Method for Solving Multi-Functional Integro-Differential Equations with Mixed Delays

M. Mustafa Bahşi [1]* ![iD], Mehmet Çevik[2] ![iD]

[1] Manisa Celal Bayar University, Kırkağaç Vocational School, Manisa/Turkey
[2] İzmir Katip Çelebi University, Department of Mechanical Engineering, İzmir/Turkey
*mustafa.bahsi@cbu.edu.tr
*Orcid No: 0000-0003-2237-5818

Abstract

In this study, we suggested a novel approach for solving multi-functional integro-differential equations with mixed delays, by using orthogonal Jacobi polynomials. These equations include various classes of differential equations, integro-differential equations and delay differential equations. This new algorithm proposes solutions for each class of these equations and combinations of equation classes, such as Volterra integro-differential equation, Fredholm integro-differential equation, pantograph-delay differential equations. Since the present method is based on fundamental matrix relations and collocation points, numerical solutions can be obtained easily by means of symbolic computation programs. We developed an error estimation algorithm based on the present method for the verification of solutions. Application of the method is illustrated by four numerical examples.

Keywords: Jacobi matrix method, functional integro-differential equation, error estimation algorithm.

1. Introduction

In recent years, many researchers have studied on the numerical solution of different classes of the integro differential equations because integro-differential equations have been one of the principal tools in various areas of applied mathematics, biological models, physics and engineering [1] and also functional integro-differential equations are often used to model some problems with aftereffect in mechanics and the related scientific fields [2]. Our study is aimed to introduce a new numerical solution method of the multi-functional integro-differential equations with mixed delays (mf-IDD Eqs.) which include Volterra integro-differential equations, Fredholm integro-differential equation, pantograph-delay differential equations and also all sub-classes or combinations of these. For this reason, we generate a procedure to obtain a numerical solution for the following mf-IDD equations

$$
\sum_{k=0}^{m_1} \sum_{l=0}^{m_2} P_{kl}(x) y^{(k)}(\alpha_{kl} x + \beta_{kl}) = f(x) + \\
\sum_{r=0}^{m_3} \sum_{s=0}^{m_4} \lambda_{rs} \int_{u_{rs}(x)}^{v_{rs}(x)} K_{rs}(x,t) y^{(r)}(\mu_{rs} t + \gamma_{rs}) dt, \\
a \le x, t \le b
$$

(1.1)

under the initial and boundary conditions

$$
\sum_{k=0}^{m-1} \left[a_{ik} y^{(k)}(a) + b_{ik} y^{(k)}(b) \right] = \eta_i, \\
m = \max(m_1, m_3), i = 0, 1, 2, \dots, m - 1
$$

(1.2)

where $P_{kj}(x)$ and $f(x)$ are known functions defined on the interval, $a \le x \le b$; $\beta_{kj}, \lambda_{rs}, \gamma_{rs} \, a_{ik}, b_{ik}$ and η_i are real or complex constants, $0 < \alpha_{kj}, \mu_{rs} < 1$, $K_{rs}(x,t)$ are kernel functions and, $y(x)$ is the unknown function to be determined.

In very recent years, several mathematicians have been interested in mf-IDD Equations and their sub-classes for obtaining numerical solutions. Oğuz and Sezer [3] developed Chelyshkov collocation method for the numerical solutions of mixed functional integro-differential equations. Mirzaee et al. [4] gave the numerical solution method based on Euler polynomial for the solutions of Volterra differential equations pantograph-delay type. Kürkçü et al. [5] used Dickson polynomials to enhance matrix based collocation method for mf-IDD equations. Yüzbaşı [6] presented a new numerical approach by using Laguerre polynomials for solving linear pantograph-type Volterra integro-

differential equations. Reutskiy [7] studied linear Volterra-Fredholm integro differential equations with linear functional arguments.

We use the orthogonal Jacobi polynomials $P_n^{(\alpha,\beta)}(x)$ in order to develop a new approach to obtain the numerical solutions of the mf-IDD equation. The orthogonal Jacobi polynomials are defined with respect to $\omega^{\alpha,\beta}(x) = (1-x)^\alpha (1+x)^\beta$ $(\alpha > -1, \beta > -1)$ (weight function) on $(-1,1)$ and it is proved that the Jacobi polynomials satisfy the following relation [8, 9];

$$P_n^{(\alpha,\beta)}(x) = \sum_{k=0}^{n} B_n^{(\alpha,\beta,n)}(x-1)^k; \quad \alpha,\beta > -1$$

$$B_n^{(\alpha,\beta,n)} = 2^{-k} \binom{n+\alpha+\beta+k}{k} \binom{n+\alpha}{n-k};$$
$$k = 0, 1, 2, \dots, n$$

Note that α and β are special parameters of the Jacobi polynomials. The Jacobi polynomials transform to some known orthogonal polynomials with respect to α and β. Some of the most important are Legendre ($\alpha = \beta = 0$), Chebyshev ($\alpha = \beta = -1/2$) and Gegenbauer ($\alpha = \beta$) polynomials. This versatility of Jacobi polynomials are provided that more than one solution unlike the most of others.

By using the definition of the Jacobi polynomials, we assume a solution expressed as the truncated series of orthogonal Jacobi polynomials defined by

$$y(x) \cong y_N^{(\alpha,\beta)}(x) = \sum_{n=0}^{N} a_n P_n^{(\alpha,\beta)}(x)$$

where $P_n^{(\alpha,\beta)}(x), n = 0, 1, 2, \dots, N$ denote the orthogonal Jacobi polynomials defined above; N is chosen any positive integer such that $N \geq n$ and $a_n, n = 0, 1, 2, \dots, N$ are unknown coefficients.

Jacobi collocation method is a collocation method based on matrix operations. This matrix operations method named "matrix method" was introduced by Sezer [8] and developed over time by applying to different problems like differential equations [9] and integro-differential equations [10]. The matrix method have also been adapted to many different problems based on various polynomials such as Bessel polynomials [11] and Laguerre polynomials [12] for various classes of the integral equations. Researchers applied the method to various engineering problems. Baykuş and Çevik [13] solved the single-degree-of-freedom (SDOF) system by using Taylor polynomials. Çevik et al. [14] solved the delayed SDOF problem by using exponential functions. Deniz and Sezer [15] solved the nonlinear heat transfer equations using Rational Chebyshev polynomials. In addition, Deniz et al. [16] published a study in which stability analysis of the Taylor Collocation Method is performed.

2. Matrix Representation of Each Term of the Problem

In this section, we transform each term of Eq. (1.1) to matrix form. First, we obtain $P_n^{(\alpha,\beta)}(x)$ orthogonal Jacobi polynomials of matrix form as follows:

$$\mathbf{P}^{(\alpha,\beta)}(x) = \mathbf{X}(x)\mathbf{M}^{(\alpha,\beta)} \tag{2.1}$$

where

$$\mathbf{P}^{(\alpha,\beta)}(x) = \begin{bmatrix} P_0^{(\alpha,\beta)}(x) & P_1^{(\alpha,\beta)}(x) & \dots & P_N^{(\alpha,\beta)}(x) \end{bmatrix}$$
$$\mathbf{X}(x) = \begin{bmatrix} 1 & (x-1) & (x-1)^2 & \dots & (x-1)^N \end{bmatrix}$$

and $\mathbf{M}^{(\alpha,\beta)} = \left[m_{ij}^{(\alpha,\beta)} \right]_{(N+1)\times(N+1)}$ such that

$$m_{ij}^{(\alpha,\beta)}$$
$$= \begin{cases} 2^{1-i} \binom{i+j-2+\alpha+\beta}{i-1} \binom{j-1+\alpha}{j-i}, & i \leq j \\ 0 & , & i > j \end{cases}$$

We assume the desired solution $y(x)$ of Eq. (1.1) to be defined by the truncated orthogonal Jacobi series in matrix form as follows:

$$\left[y_N^{(\alpha,\beta)}(x) \right] = \mathbf{P}^{(\alpha,\beta)}(x)\mathbf{A} \tag{2.2}$$

where $\mathbf{A} = \left[a_{ij} \right]_{(N+1)\times 1}$ such that
$$a_{ij} = a_{i-1} \tag{2.3}$$

By substituting the matrix form of Jacobi polynomials (2.1) into (2.2), we can obtain the fundamental matrix equation of the approximate solution for the unknown function as [17, 18]

$$\left[y_N^{(\alpha,\beta)}(x) \right] = \mathbf{X}(x)\mathbf{M}^{(\alpha,\beta)}\mathbf{A}. \tag{2.4}$$

First, in order to explain the relation between the matrix form of the unknown function $y(x)$ and the matrix form of its derivatives $y^{(k)}(x)$, we introduce the relation between the matrix $\mathbf{X}(x)$ and its derivatives $\mathbf{X}^{(k)}(x)$ which can be expressed as

$$\mathbf{X}^{(k)}(x) = \mathbf{X}(x)\mathbf{B}^k \tag{2.5}$$

where $\mathbf{B} = \left[b_{ij} \right]_{(N+1)\times(N+1)}$ such that

$$b_{ij} = \begin{cases} i & , & j-i = 1 \\ 0 & , & others \end{cases}$$

Then, using (2.4) and (2.5), one may write

$$\begin{aligned} \left[y^{(k)}(x) \right] &\cong \left[\left(y_N^{(\alpha,\beta)} \right)^{(k)}(x) \right] \\ &= \mathbf{X}^{(k)}(x)\mathbf{M}^{(\alpha,\beta)}\mathbf{A} \\ &= \mathbf{X}(x)\mathbf{B}^k\mathbf{M}^{(\alpha,\beta)}\mathbf{A} \end{aligned} \tag{2.6}$$

Similarly, the relation between the matrix form of $y(x)$ and the matrix form of its delay forms' derivatives $y^{(k)}(\alpha_{kl}x + \beta_{kl})$ can be expressed as

$$
\begin{aligned}
y^{(k)}(\alpha_{kl}x + \beta_{kl}) &= \mathbf{X}^{(k)}(\alpha_{kl}x + \beta_{kl})\mathbf{M}^{(\alpha,\beta)}\mathbf{A} \\
&= \mathbf{X}(\alpha_{kl}x + \beta_{kl})\mathbf{B}^k\mathbf{M}^{(\alpha,\beta)}\mathbf{A} \qquad (2.7) \\
&= \mathbf{X}(x)\mathbf{B}(\alpha_{kl},\beta_{kl})\mathbf{B}^k\mathbf{M}^{(\alpha,\beta)}\mathbf{A}
\end{aligned}
$$

where $\mathbf{B}(\alpha_{kj},\beta_{kj}) = [b_{ij}(\alpha_{kl},\beta_{kl})]_{(N+1)\times(N+1)}$ such that

$$
b_{ij}(\alpha_{kl},\beta_{kl}) = \begin{cases} \binom{j-1}{i-1}(\alpha_{kj})^{i-1}(\beta_{kj})^{j-i} & , \quad i \leq j \\ 0 & , \quad i > j \end{cases}
$$

Using (2.7), the matrix form of the differential part of Eq. (1.1) becomes

$$
\begin{aligned}
&\sum_{k=0}^{m_1}\sum_{l=0}^{m_2} P_{kl}(x)y^{(k)}(\alpha_{kl}x + \beta_{kl}) \\
&= \sum_{k=0}^{m_1}\sum_{l=0}^{m_2} P_{kl}(x)\mathbf{X}(x)\mathbf{B}(\alpha_{kl},\beta_{kl})\mathbf{B}^k\mathbf{M}^{(\alpha,\beta)}\mathbf{A}
\end{aligned} \qquad (2.8)
$$

Finally, the matrix form of the integral part of Eq. (1.1) is obtained as follows

$$
\begin{aligned}
&\int_{u_{rs}(x)}^{v_{rs}(x)} K_{rs}(x,t)y^{(r)}(\mu_{rs}t + \gamma_{rs})dt \\
&= \int_{u_{rs}(x)}^{v_{rs}(x)} K_{rs}(x,t)\mathbf{X}(t)\mathbf{B}(\mu_{rs},\gamma_{rs})\mathbf{B}^r\mathbf{M}^{(\alpha,\beta)}\mathbf{A}dt \\
&= \left(\int_{u_{rs}(x)}^{v_{rs}(x)} K_{rs}(x,t)\mathbf{X}(t)dt\right)\mathbf{B}(\mu_{rs},\gamma_{rs})\mathbf{B}^r\mathbf{M}^{(\alpha,\beta)}\mathbf{A} \\
&= \mathbf{Q}_{rs}(x)\mathbf{B}(\mu_{rs},\gamma_{rs})\mathbf{B}^r\mathbf{M}^{(\alpha,\beta)}\mathbf{A}
\end{aligned}
$$

where $\mathbf{Q}_{rs}(x) = [q_{ij}(x)]_{1\times(N+1)}$ such that

$$
q_{ij}(x) = \int_{u_{rs}(x)}^{v_{rs}(x)} K_{rs}(x,t)(t-1)^{j-1}dt
$$

We can write briefly as follows:

$$
\begin{aligned}
&\int_{u_{rs}(x)}^{v_{rs}(x)} K_{rs}(x,t)y^{(r)}(\mu_{rs}t + \gamma_{rs})dt \\
&= \mathbf{Q}_{rs}(x)\mathbf{B}(\mu_{rs},\gamma_{rs})\mathbf{B}^r\mathbf{M}^{(\alpha,\beta)}\mathbf{A}
\end{aligned} \qquad (2.9)
$$

From (2.8) and (2.9), we obtain the matrix form of Eq. (1.1) as follows:

$$
\begin{aligned}
&\sum_{k=0}^{m_1}\sum_{l=0}^{m_2} P_{kl}(x)\mathbf{X}(x)\mathbf{B}(\alpha_{kl},\beta_{kl})\mathbf{B}^k\mathbf{M}^{(\alpha,\beta)}\mathbf{A} \\
&\qquad\qquad = f(x) \qquad (2.10) \\
&+ \sum_{r=0}^{m_3}\sum_{s=0}^{m_4} \lambda_{rs}\mathbf{Q}_{rs}(x)\mathbf{B}(\mu_{rs},\gamma_{rs})\mathbf{B}^r\mathbf{M}^{(\alpha,\beta)}\mathbf{A}
\end{aligned}
$$

We can obtain the corresponding matrix forms for the conditions (1.2), by means of the relation (2.4), as

$$
\begin{aligned}
&\sum_{k=0}^{m-1}[a_{ik}y^{(k)}(a) + b_{ik}y^{(k)}(b)] \\
&= \sum_{k=0}^{m-1}[a_{ik}\mathbf{X}(a)\mathbf{B}^k\mathbf{M}^{(\alpha,\beta)}\mathbf{A} \qquad (2.11) \\
&\qquad + b_{ik}\mathbf{X}(b)\mathbf{B}^k\mathbf{M}^{(\alpha,\beta)}\mathbf{A}] \\
&= [\eta_i], \\
&i = 0,1,2,\dots,m-1.
\end{aligned}
$$

3. Method of Solution

For constructing the matrix equation, the matrix relations (2.8) and (2.9) are first substituted into Eq. (1.1); then, by using collocation points defined by

$$
x_\tau = a + \frac{b-a}{N}\tau, \qquad \tau = 0,1,2,\dots,N
$$

the system of matrix equations is obtained as

$$
\begin{aligned}
&\sum_{k=0}^{m_1}\sum_{l=0}^{m_2} P_{kl}(x_\tau)\mathbf{X}(x_\tau)\mathbf{B}(\alpha_{kl},\beta_{kl})\mathbf{B}^k\mathbf{M}^{(\alpha,\beta)}\mathbf{A} \\
&= f(x_\tau) + \sum_{r=0}^{m_3}\sum_{s=0}^{m_4} \lambda_{rs}\mathbf{Q}_{rs}(x_\tau)\mathbf{B}(\mu_{rs},\gamma_{rs})\mathbf{B}^r\mathbf{M}^{(\alpha,\beta)}\mathbf{A}, \\
&\qquad\qquad \tau = 0,1,2,\dots,N
\end{aligned}
$$

Therefore, the fundamental matrix equation becomes

$$
\begin{aligned}
&\left\{\sum_{k=0}^{m_1}\sum_{l=0}^{m_2} \mathbf{P}_{kl}\mathbf{X}\mathbf{B}(\alpha_{kl},\beta_{kl})\mathbf{B}^k\mathbf{M}^{(\alpha,\beta)}\right. \\
&\left. - \sum_{r=0}^{m_3}\sum_{s=0}^{m_4} \lambda_{rs}\overline{\mathbf{Q}_{rs}}\mathbf{B}(\mu_{rs},\gamma_{rs})\mathbf{B}^r\mathbf{M}^{(\alpha,\beta)}\right\}\mathbf{A} = \mathbf{F}
\end{aligned} \qquad (3.1)
$$

where $\mathbf{P}_{kl} = [p]_{(N+1)\times(N+1)}$

$$
\mathbf{P}_{kl} = \begin{bmatrix} P_{kl}(x_0) & 0 & \cdots & 0 \\ 0 & P_{kl}(x_1) & \cdots & 0 \\ \vdots & \vdots & \ddots & \vdots \\ 0 & 0 & \cdots & P_{kl}(x_N) \end{bmatrix},
$$

$$
\mathbf{F} = \begin{bmatrix} f(x_0) \\ f(x_1) \\ \vdots \\ f(x_N) \end{bmatrix},
$$

$$
\overline{\mathbf{Q}_{rs}} = \begin{bmatrix} \mathbf{Q}_{rs}(x_0) \\ \mathbf{Q}_{rs}(x_1) \\ \vdots \\ \mathbf{Q}_{rs}(x_N) \end{bmatrix} \text{ and } \mathbf{X} = \begin{bmatrix} \mathbf{X}(x_0) \\ \mathbf{X}(x_1) \\ \vdots \\ \mathbf{X}(x_N) \end{bmatrix}.
$$

The fundamental matrix equation (2.10) of Eq. (1.1) corresponds to a system of $N+1$ algebraic equations for the $N+1$ unknown coefficients $a_0, a_1, a_2, \cdots, a_N$. Briefly, if we determine

$$\mathbf{W}$$

$$= \left(\sum_{k=0}^{m_1} \sum_{i=0}^{m_2} \mathbf{P}_{kl} \mathbf{X} \mathbf{B}(\alpha_{kl}, \beta_{kl}) \mathbf{B}^k \right.$$

$$\left. - \sum_{r=0}^{m_3} \sum_{s=0}^{m_4} \lambda_{rs} \overline{\mathbf{Q}_{rs}} \mathbf{B}(\mu_{rs}, \gamma_{rs}) \mathbf{B}^r \right) \mathbf{M}^{(\alpha,\beta)}$$

then, we can write Eq. (3.1) in the form

$$\mathbf{WA} = \mathbf{F} \text{ or } [\mathbf{W}; \mathbf{F}]. \tag{3.2}$$

On the other hand, from (2.11), we can obtain the matrix form of conditions briefly as
$$\mathbf{U}_i \mathbf{A} = \eta_i \text{ or } [\mathbf{U}_j; \eta_i], \quad i = 0, 1, 2, \dots, m-1 \tag{3.3}$$

such that

$$\mathbf{U}_i = \sum_{k=0}^{m-1} [a_{ik} \mathbf{X}(a) + b_{ik} \mathbf{X}(b)] \, \mathbf{B}^k \mathbf{M}^{(\alpha,\beta)}$$

Consequently, in order to obtain the solution of Eq. (1.1) under the mixed conditions (1.2), we replace the row matrix (3.3), by last n rows of the augmented matrix (3.2), which yields the required augmented matrix

$$[\widehat{\mathbf{W}}; \widetilde{\mathbf{F}}] \tag{3.4}$$

If $\text{rank}\widehat{\mathbf{W}} = \text{rank}[\widehat{\mathbf{W}}; \widetilde{\mathbf{F}}] = N + 1$, then we can write $\mathbf{A} = (\widehat{\mathbf{W}})^{-1} \widetilde{\mathbf{F}}$. Thus the matrix $\mathbf{A}$ (thereby the coefficients $a_0, a_1, a_2, \cdots, a_N$) is uniquely determined. Eq. (1.1) has also a unique solution under the conditions (1.2). This solution is given by the truncated orthogonal Jacobi series. Thus we get the Jacobi polynomial solution for the arbitrary parameters α and β:

$$y(x) \cong y_N^{(\alpha,\beta)}(x) = \sum_{n=0}^{N} a_n P_n^{(\alpha,\beta)}(x)$$

4. Error Estimation Algorithm and Improved Solution

One of the ultimate objectives in this study is to develop an error estimation algorithm for mf-IDD equations and to obtain an improved solution of the Jacobi polynomial solution. Valid here only that the improved Jacobi polynomial solution is found by using error estimation algorithm. To obtain the error estimation function of the initial solution, we define the residual function of Eq. (1.1) [19] as

$$R_N(x)$$
$$= \sum_{k=0}^{m_1} \sum_{l=0}^{m_2} P_{kl}(x)(y_N^{(\alpha,\beta)})^{(k)}(\alpha_{kl}x + \beta_{kl})$$
$$- f(x)$$
$$- \sum_{r=0}^{m_3} \sum_{s=0}^{m_4} \lambda_{rs} \int_{u_{rs}(x)}^{v_{rs}(x)} K_{rs}(x,t)(y_N^{(\alpha,\beta)})^{(r)}(\mu_{rs}t$$
$$+ \gamma_{rs})dt \tag{4.1}$$

where $y_N^{(\alpha,\beta)}(x)$ is the approximate solution of the problem (1.1)-(1.2) for special Jacobi parameters α and β. On the other hand, $y_N^{(\alpha,\beta)}(x)$ satisfies the Eq. (1.1)-(1.2):

$$\sum_{k=0}^{m_1} \sum_{l=0}^{m_2} P_{kl}(x)(y_N^{(\alpha,\beta)})^{(k)}(\alpha_{kl}x + \beta_{kl})$$
$$- \sum_{r=0}^{m_3} \sum_{s=0}^{m_4} \lambda_{rs} \int_{u_{rs}(x)}^{v_{rs}(x)} K_{rs}(x,t) \left(y_N^{(\alpha,\beta)}\right)^{(r)} (\mu_{rs}t$$
$$+ \gamma_{rs})dt = R_N(x) - f(x) \tag{4.2}$$
$$\sum_{k=0}^{m-1} \left[a_{ik}(y_N^{(\alpha,\beta)})^{(k)}(a) + b_{ik}(y_N^{(\alpha,\beta)})^{(k)}(b)\right]$$
$$= \eta_i,$$
$$i = 0, 1, 2, \dots, m-1$$

The error function $e_N^{(\alpha,\beta)}(x)$ can be defined as

$$e_N^{(\alpha,\beta)}(x) = y(x) - y_N^{(\alpha,\beta)}(x) \tag{4.3}$$

where $y(x)$ is the exact solution of the problem (1.1)-(1.2). Substituting (4.3) into (1.1)-(1.2) and using (4.1) and (4.2), we derive the error differential equation with homogenous conditions:

$$\sum_{k=0}^{m_1} \sum_{l=0}^{m_2} P_{kl}(x)(e_N^{(\alpha,\beta)})^{(k)}(\alpha_{kl}x + \beta_{kl})$$
$$- \sum_{r=0}^{m_3} \sum_{s=0}^{m_4} \lambda_{rs} \int_{u_{rs}(x)}^{v_{rs}(x)} K_{rs}(x,t) \left(e_N^{(\alpha,\beta)}\right)^{(r)} (\mu_{rs}t$$
$$+ \gamma_{rs})dt = -R_N(x) \tag{4.4}$$
$$\sum_{k=0}^{m-1} \left[a_{jk} \left(e_N^{(\alpha,\beta)}\right)^{(k)}(a) + b_{jk} \left(e_N^{(\alpha,\beta)}\right)^{(k)}(b)\right]$$
$$= 0$$

Solving the problem (4.4) in the same way as in Section 3, we get the approximation $e_{N,M}^{(\alpha,\beta)}(x)$ to $e_N^{(\alpha,\beta)}(x)$, $M > N$ which is the error function based on the residual function $R_N(x)$. Consequently, by means of the orthogonal Jacobi polynomials $y_N^{(\alpha,\beta)}(x)$ and $e_{N,M}^{(\alpha,\beta)}(x)$, we obtain the improved Jacobi solution as

$$y_{N,M}^{(\alpha,\beta)}(x) = y_N^{(\alpha,\beta)}(x) + e_{N,M}^{(\alpha,\beta)}(x) \tag{4.5}$$

where, $e_{N,M}^{(\alpha,\beta)}(x)$ is the estimated error function.

5. Illustrative Examples

In this section, we apply the new Jacobi matrix method to four examples by using symbolic computational programing MAPLE. In these examples, the terms $\left|e_N^{(\alpha,\beta)}(x)\right|$ and $\left|E_{N,M}^{(\alpha,\beta)}(x)\right|$ represent the absolute error function for Jacobi polynomial solution and the absolute error function of the improved Jacobi polynomial solution, respectively.

5.1. Example 1

We consider the third order integro-differential equations

$$y'''(x) - xy'(x-1) + 4y\left(\frac{1}{2}x - 1\right)$$
$$= f(x) - 9 \int_{x^2-5}^{x^4+1} xt y'^{\left(\frac{1}{3}t-1\right)} dt, \quad \textbf{(5.1)}$$

The collocation points are determined as

$$\left\{x_0 = 0, \; x_1 = \frac{1}{4}, x_2 = \frac{2}{4}, x_3 = \frac{3}{4} \; x_4 = 1\right\}$$

and from Eq. (3.1), the fundamental matrix equation of problem is

$$0 \le x, t \le 1$$
$$y(0) = -2, y'(0) = 0, y''(0) = 12$$

where $f(x) = 3x^{17} - 21x^9 + 72x^7 - 654x^5 + 2390x^3 + 6x^2 - 3384x + 24$ and the exact solution of the problem is $y(x) = 4x^3 + 6x^2 - 2$.

We assume that, for $N = 4$ and $(\alpha, \beta) = (1/2, 1/3)$ which are chosen arbitrarily, the problem has a Jacobi polynomial solution in the form,

$$y(\text{x}) = \mathbf{P}^{(\alpha,\beta)}(x)\mathbf{A}$$

such that

$$\mathbf{A} = [a_0 \quad a_1 \quad \cdots \quad a_N]^{\mathbf{T}}$$

and

$$\mathbf{P}^{(\alpha,\beta)}(x) = \left[P_0^{(\alpha,\beta)}(x) \quad P_1^{(\alpha,\beta)}(x) \quad P_2^{(\alpha,\beta)}(x) \quad P_3^{(\alpha,\beta)}(x) \quad P_4^{(\alpha,\beta)}(x)\right]$$

$$= \begin{bmatrix} 1 \\ \dfrac{1}{12} + \dfrac{17x}{12} \\ -\dfrac{35}{12} + \dfrac{115}{24}x + \dfrac{667(x-1)^2}{288} \\ -\dfrac{805}{96} + \dfrac{1015}{96}x + \dfrac{7105(x-1)^2}{576} + \dfrac{41615(x-1)^3}{10368} \\ -\dfrac{2135}{128} + \dfrac{1225}{64}x + \dfrac{10045(x-1)^2}{256} + \dfrac{67445(x-1)^3}{2304} + \dfrac{3574585(x-1)^4}{497664} \end{bmatrix}^{\mathbf{T}}$$

$$\mathbf{WA} = \mathbf{F}$$

where

$$\mathbf{W} = \begin{bmatrix} 4 & -\dfrac{16}{3} & \dfrac{56}{9} & \dfrac{89005}{5184} & \dfrac{668255}{62208} \\ 4 & -\dfrac{265668199}{6291456} & \dfrac{2542557122971}{9663676416} & -\dfrac{329287935484420465}{237494511599616} & -\dfrac{394241050944918737 5159}{547187354725515264} \\ 4 & -\dfrac{298781}{4096} & \dfrac{554514379}{1179648} & -\dfrac{13410744877075}{5435817984} & \dfrac{361276085811263}{28991029248} \\ 4 & -\dfrac{5670779253}{6291456} & \dfrac{5644627506113}{9663676416} & -\dfrac{2131519714347125305}{712483534798848} & \dfrac{79559211137590390897 81}{547187354725515264} \\ 4 & -\dfrac{965}{12} & \dfrac{165437}{288} & -\dfrac{19998965}{6912} & \dfrac{8850194563}{663552} \end{bmatrix}$$

$$\mathbf{F} = \begin{bmatrix} 24 & -\dfrac{13484747456509}{17179869184} & -\dfrac{181884157}{131072} & -\dfrac{28337926270647}{17179869184} & -1564 \end{bmatrix}^{\mathbf{T}}$$

Using (3.3), we can write the matrix form of the initial conditions of the problem as follows

$$[\mathbf{U} \quad ; \quad \boldsymbol{\gamma}]$$

$$= \begin{bmatrix} 1 & \dfrac{1}{12} & -\dfrac{173}{288} & -\dfrac{665}{10368} & \dfrac{233065}{497664} & ; & -2 \\ 0 & \dfrac{17}{12} & \dfrac{23}{144} & -\dfrac{7105}{3456} & -\dfrac{30835}{124416} & ; & 0 \\ 0 & 0 & \dfrac{667}{144} & \dfrac{1015}{1728} & -\dfrac{454895}{41472} & ; & 12 \end{bmatrix}$$

Consequently, to obtain the solution of Eq. (5.1) under the initial conditions, by replacing the row matrix $[\mathbf{U}; \boldsymbol{\gamma}]$, by third and fourth rows of augmented matrix $[\mathbf{W}; \mathbf{F}]$, we obtain the required augmented matrix $[\widetilde{\mathbf{W}}; \widetilde{\mathbf{G}}]$.

By solving the augmented matrix $[\widetilde{\mathbf{W}}; \widetilde{\mathbf{F}}]$, we obtain the Jacobi polynomial coefficient matrix

$$\mathbf{A} = \left[-\frac{6272}{111339} \quad \frac{576}{493} \quad \frac{67392}{27347} \quad \frac{41472}{41615} \quad 0 \right]^{\mathrm{T}}.$$

From Eq. (3.4), the Jacobi polynomial solution of the problem is

$y_4^{(1/2,1/3)}(x) = 8 + 24(x-1) + 18(x-1)^2 + 4(x-1)^3$ which is the exact solution of the problem. Likewise, we can extract the exact solution of the problem for $N = 5$ and different values of α and β.

5.2. Example 2

We consider the first order integro-differential equations [3, 6]

$$y'(x) = y(x) - 2y'\left(x - \frac{1}{2}\right)$$
$$+ (x - x^2)y\left(\frac{1}{2}x - 1\right)$$
$$+ \int_0^x xe^{-t}y(t)dt + \int_0^{x/2} xe^{-t}y'(t)dt + f(x), \qquad \textbf{(5.2)}$$
$$0 \le x, t \le 1$$
$$y(0) = y'(0) = 1.$$

In Refs. [3, 6], $f(x) = -(x - x^2)e^{\left(\frac{x}{2}-1\right)} + 2e^{\left(x-\frac{1}{2}\right)} - x^2e^{\left(\frac{x}{2}\right)} + xe^{\left(\frac{x}{2}\right)}$, and the exact solution of the problem is $y(x) = e^x$.

Table 1 shows that both Jacobi polynomial solutions and improved Jacobi polynomial solutions are more effective than other methods.

In Table 2, we have presented a comparison of the absolute error values with the estimated absolute errors values, and it is seen that the error estimation is corrected gradually as M increases.

In Table 1 and Table 2 Jacobi polynomial solutions obtained for the Chebyshev base are then $\alpha = \beta = -1/2$. Chebyshev solutions are nearly the same with respect to the arbitrary α and β such that $(\alpha, \beta) = (1/2, 1/2)$ and $(\alpha, \beta) = (0, 1/3)$.

Table 1. Comparison of the absolute errors of the improved Jacobi method with some other numerical methods for Example 2.

	Present Method			Chelyshkov collocation method [3]	Laguerre collocation method [6]
x_i	$\left\|e_4^{(\alpha,\beta)}(x_i)\right\|$	$\left\|E_{4,5}^{(\alpha,\beta)}(x_i)\right\|$	$\left\|E_{4,6}^{(\alpha,\beta)}(x_i)\right\|$	$N = 4$	$N = 4$
0	0	0	0	0	$1.776e - 15$
0.2	$1.646e - 4$	$2.714e - 5$	$2.717e - 6$	$2.926e - 4$	$3.460e - 4$
0.4	$3.767e - 5$	$6.942e - 5$	$2.335e - 6$	$2.704e - 4$	$5.863e - 4$
0.6	$4.714e - 4$	$5.886e - 5$	$1.289e - 5$	$4.497e - 4$	$2.228e - 4$
0.8	$7.898e - 4$	$4.248e - 5$	$1.425e - 5$	$1.740e - 3$	$8.626e - 4$
1	$8.507e - 4$	$6.759e - 5$	$5.301e - 7$	$2.432e - 3$	$1.876e - 4$
x_i	$\left\|e_7^{(\alpha,\beta)}(x_i)\right\|$	$\left\|E_{7,8}^{(\alpha,\beta)}(x_i)\right\|$	$\left\|E_{7,9}^{(\alpha,\beta)}(x_i)\right\|$	$N = 7$	$N = 7$
0	0	0	0	0	$1.998e - 15$
0.2	$7.603e - 7$	$1.672e - 8$	$2.079e - 8$	$7.378e - 6$	$6.022e - 7$
0.4	$1.493e - 6$	$1.527e - 7$	$2.836e - 8$	$1.773e - 6$	$1.519e - 6$
0.6	$6.317e - 7$	$3.601e - 7$	$6.893e - 9$	$1.851e - 5$	$1.157e - 6$
0.8	$1.797e - 6$	$2.488e - 7$	$6.128e - 8$	$2.969e - 5$	$1.133e - 6$
1	$3.073e - 6$	$2.774e - 7$	$5.559e - 8$	$2.117e - 6$	-

Table 2. Comparison of the absolute error with the estimated absolute errors for Example 2.

x_i	Actual Absolute Error $\left\|e_4^{(\alpha,\beta)}(x)\right\|$	Estimated Absolute Errors $\left\|e_{4,7}^{(\alpha,\beta)}(x)\right\|$	$\left\|e_{4,8}^{(\alpha,\beta)}(x)\right\|$	$\left\|e_{4,9}^{(\alpha,\beta)}(x)\right\|$	$\left\|e_{4,10}^{(\alpha,\beta)}(x)\right\|$
0	0	0	0	0	0
0.2	$1.646e-4$	$1.653e-4$	$1.645e-4$	$1.645e-4$	$1.646e-4$
0.4	$3.767e-5$	$3.917e-5$	$3.783e-5$	$3.765e-5$	$3.767e-5$
0.6	$4.714e-4$	$4.708e-4$	$4.710e-4$	$4.714e-4$	$4.714e-4$
0.8	$7.898e-4$	$7.916e-4$	$7.896e-4$	$7.898e-4$	$7.898e-4$
1	$8.507e-4$	$8.476e-4$	$8.504e-4$	$8.507e-4$	$8.507e-4$

5.3. Example 3

Let us consider the Volterra type integro differential equation

$$y'(x) = \int_{x-1}^{x} (\cos(x+t+1)+2)y(t)dt + g(x), \qquad 0 \le x \le 3 \qquad (5.3)$$

with the initial condition is $y(0) = 1$ and $f(x) = 3\cos(x) - \frac{1}{4}\cos(3x+1) - 2 + \frac{1}{2}\sin(x+1) + \sin(2x) - 2\cos(x-1) + \frac{1}{4}\cos(3x+1) - \sin(2x+1)$. The exact solution of the problem is $y(x) = \sin(x) + 1$ [6].

Table 3 is shown the absolute error values of Jacobi polynomial solutions both direct solution for $N = 10$ and improved solutions for $M = 12$ and $M = 14$ in domain interval of the problem. And also, Table 3 is given comparison of the absolute errors values of the present method with Taylor collocation and Laguerre collocation methods.

Figure 1 is shown the comparison of exact solution and Jacobi polynomial solutions ($N = 4$, 5 and 6) and it is clearly seen form the figure that the numerical solutions

close the exact solution when N increases in [0,3] domain.

Jacobi polynomial solutions are obtained for the $\alpha = 0$ and $\beta = -1/2$. And also Legendre and Chebyshev solutions are obtained. For N=10 the absolute errors of the Legendre base solution is $7.254e-9$ and the absolute Chebyshev base solution is $8.226e-9$ while the Jacobi polynomial solution is $7.095e-9$.

5.4. Example 4

Consider the first order integro-differential equation

$$y'(x) = 2e^{1-x} - 3y(x) - 3\int_{x-1}^{x} y(t)dt - \int_{x-1}^{x} y'(t)dt, 0 \le x, t \le 2 \qquad (5.4)$$

under the initial condition

$$y(0) = 1.$$

with the exact solution $y(x) = e^{-x}$ [6, 20, 21].

Table 3. Comparison of the absolute errors of the improved Jacobi method with some other numerical methods for $N = 10$ and for $(N, M) = (10,12), (10,14)$ for Example 3.

x_i	Present Method $\left\|e_{10}^{(\alpha,\beta)}(x)\right\|$	$\left\|E_{10,12}^{(\alpha,\beta)}(x)\right\|$	$\left\|E_{10,14}^{(\alpha,\beta)}(x)\right\|$	Taylor collocation method [20] 16 collocation points	25 collocation points	Laguerre collocation method [6] $N = 10$
0.5	$7.095e-9$	$2.494e-9$	$3.564e-11$	$1.04e-6$	$1.0e-9$	$1.130e-08$
1.0	$7.034e-9$	$3.428e-9$	$5.276e-11$	$2.13e-6$	$7.0e-9$	$2.152e-08$
1.5	$5.704e-9$	$4.999e-9$	$7.585e-11$	$3.03e-6$	$1.3e-8$	$7.639e-09$
2.0	$1.010e-8$	$8.162e-9$	$1.240e-10$	$4.12e-6$	$2.6e-9$	$4.280e-10$
2.5	$1.957e-8$	$1.628e-8$	$2.474e-10$	$6.19e-6$	$4.7e-7$	$5.046e-07$
3	$1.476e-7$	$3.304e-8$	$5.484e-10$	$1.0e-5$	$8.9e-5$	$2.108e-05$
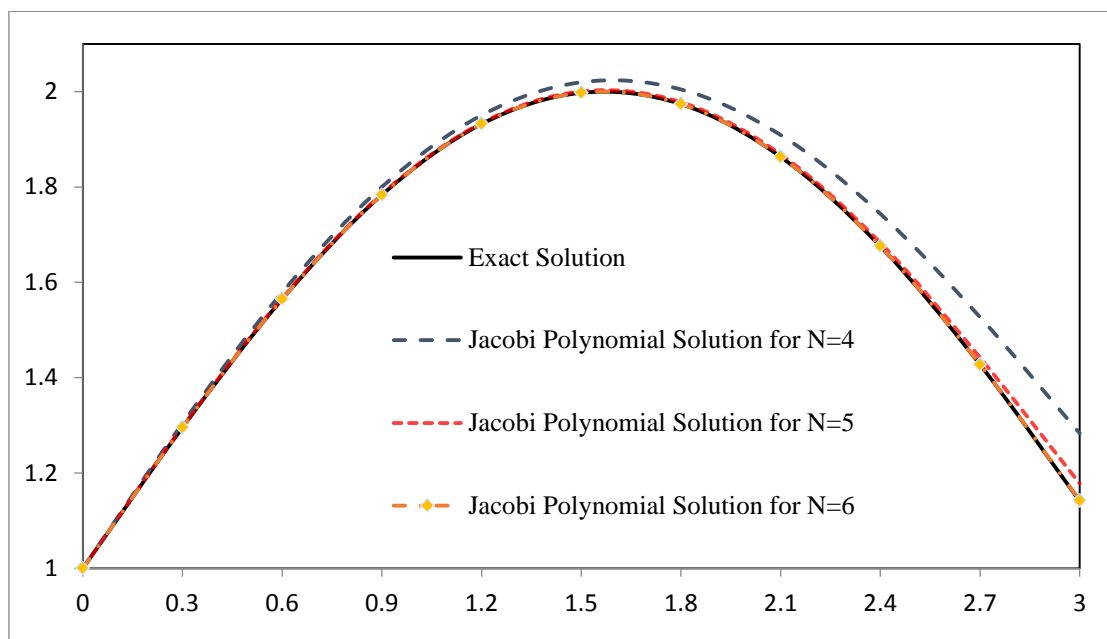
Figure 1. Comparison of exact solution and Jacobi polynomial solutions ($N = 4, 5$ and 6) for Example 3.

Table 4. Comparison of the maximum absolute error values with Jacobi collocation method and Spline collocation method (via various collocation parameters) and Laguerre collocation method for Example 4.

Maximum absolute error values			
Spline collocation method - Gauss I (by using collocation points 30) [6, 21]	$8.33e-9$	Spline collocation method – Gauss I (by using collocation points 60) [6, 21]	$1.30e-10$
Spline collocation method – Radau II (by using collocation points 30) [6, 21]	$1.43e-7$	Spline collocation method – Radau II (by using collocation points 60) [6, 21]	$4.67e-9$
Spline collocation method – Lobatto (by using collocation points 30) [6, 21]	$1.81e-6$	Spline collocation method - Lobatto (by using collocation points 60) [6, 21]	$1.13e-7$
Spline collocation method – Gauss I (by using collocation points 20) [6, 21]	$9.10e-7$	Spline collocation method – Gauss I (by using collocation points 40) [6, 21]	$6.57e-8$
Spline collocation method – Other (by using collocation points 30) [6, 21]	$4.25e-6$	Spline collocation method – Other (by using collocation points 60) [6, 21]	$5.85e-7$
Laguerre collocation method (by using collocation points 10) [6]	$4.80e-8$	Laguerre collocation method (by using collocation points 15) [6]	$2.93e-10$
Present Method (by using collocation points 10)	$2.93e-9$	Present Method (by using collocation points 15)	$1.31e-11$

It is seen clearly from Table 4 that the Jacobi polynomial solution gives better results with respect to Laguerre collocation method [6] and Spline collocation method for the collocation parameters for Gauss, Radau II, Lobatto, Gauss I and named as Other [21].

6. Conclusion

This study presented a new numerical method for solving multi-functional integro-differential equations with mixed delays. This method is based on Jacobi polynomials and matrix operations. From the obtained numerical results, it was concluded that the obtained results are excellent in terms of accuracy and corrections for all four tested problems. The main

advantage of the Jacobi collocation method is that it is easily programmable by using symbolic codes.

Therefore, the results of the problems are obtained quickly. Another advantage of the method is that the absolute error value of the obtained solutions decreases when N is increased. Estimated absolute error functions are obtained for the Jacobi Polynomial solutions obtained by the error estimation algorithm given Section 4.

Author's Contributions

M. Mustafa BAHŞI: Drafted and wrote the manuscript, performed the experiment and result analysis.

Mehmet ÇEVİK: Assisted in analytical analysis on the structure, supervised the experiment's progress, result interpretation and helped in manuscript preparation.

Ethics

There are no ethical issues after the publication of this manuscript.

References

1. Wazwaz, AM. Linear and Nonlinear Integral Equations Higher Education Press, Springer-Verlag, Beijing, Berlin, Heidelberg, 2011; pp 639.

2. Kolmanovskii, V, Myshkis, A. Introduction to the Theory and Applications of Functional Differential Equations. Kluger Academic Publishers, Dordrecht, Boston, London, 1999; pp 278.

3. Oğuz, C, Sezer, M. 2015. Chelyshkov collocation method for a class of mixed functional integro-differential equations. *Applied Mathematics and Computation*; 259: 943-954.

4. Farshid, M, Bimesl, S, Tohidi, E. 2016. A numerical framework for solving high-order pantograph-delay Volterra integro-differential equations. *Kuwait Journal of Science*; 43.1: 69-83.

5. Kürkçü, ÖK, Aslan, E, Sezer, M. 2016. A numerical approach with error estimation to solve general integro-differential–difference equations using Dickson polynomials. *Applied Mathematics and Computation*; 276: 324-339.

6. Yüzbaşı, Ş. 2014. Laguerre approach for solving pantograph-type Volterra integro-differential equations. *Applied Mathematics and Computation*; 232: 1183-1199.

7. Reutskiy, SY. 2016. The backward substitution method for multipoint problems with linear Volterra–Fredholm integro-differential equations of the neutral type. *Journal of Computational and Applied Mathematics*; 296: 724-738.

8. Sezer, M. 1994. Taylor polynomial solutions of Volterra integral equations. *International Journal of Mathematical Education in Science and Technology;* 25.5: 625-633.

9. Sezer, M, Kaynak, M. 1996. Chebyshev polynomial solutions of linear differential equations. *International Journal of Mathematical Education in Science and Technology;* 27.4: 607-618.

10. Akyüz, A, Sezer, M. 1999. A Chebyshev collocation method for the solution of linear integro-differential equations. *International Journal of Computer Mathematics;* 72.4: 491-507.

11. Şahin, N, Yüzbaşı, Ş, Gülsu, M. 2011. A collocation approach for solving systems of linear Volterra integral equations with variable coefficients. *Computers & Mathematics with Applications;* 62.2: 755-769.

12. Yüzbaşı, Ş. 2014. Laguerre approach for solving pantograph-type Volterra integro-differential equations. *Applied Mathematics and Computation;* 232: 1183-1199.

13. Kurt, N, Çevik, M. 2008. Polynomial solution of the single degree of freedom system by Taylor matrix method. *Mechanics Research Communications;* 35.8: 530-536.

14. Çevik, M, Bahşi, MM, Sezer, M. 2014. Solution of the delayed single degree of freedom system equation by exponential matrix method. *Applied Mathematics and Computation;* 242: 444-453.

15. Deniz, S, Sezer, M. 2020. Rational Chebyshev collocation method for solving nonlinear heat transfer equations. *International Communications in Heat and Mass Transfer;* 114: 104595.

16. Deniz, S, Bildik, N. 2017, A note on stability analysis of Taylor collocation method. *Celal Bayar Üniversitesi Fen Bilimleri Dergisi;* 13.1: 149-153.

17. Bahşi, MM, Çevik, M, Kurt Bahşi A, Sezer, M. 2016. Improved Jacobi matrix method for the numerical solution Fredholm integro-differential-difference equations. *Mathematical Sciences.* 10:83-93.

18. Bahşi, MM, Çevik, M, Sezer, M. 2018. Jacobi polynomial solutions of Volterra integro-differential equations with weakly singular kernel. *New Trends in Mathematical Sciences*; 6.3: 24-38.

19. Şahin, M, Sezer, M. 2018. Pell-Lucas collocation method for solving high-order functional differential equations with hybrid delays. *Celal Bayar Üniversitesi Fen Bilimleri Dergisi*; 14.2: 141-149.

20. Bellour, A, Bousselsal, M. 2014. Numerical solution of delay integro-differential equations by using Taylor collocation method. *Mathematical Methods in the Applied Sciences*; 37.10: 1491-1506.

21. Horvat, V. On polynomial spline collocation methods for neutral Volterra integro–differential equations with delay arguments. Proceedings of the 1. Conference on Applied Mathematics and Computation, Dubrovnik, Croatia, 1999.

Celal Bayar University Journal of Science

Determination of Antibiotic Susceptibility Profile and *Intl*1, *bla*SHV and *bla*TEM Genes of Raw Milk Origin Enterobacteriaceae Isolates

Ceren Başkan[1*] iD

[1]Amasya University, Sabuncuoğlu Şerefeddin Health Services Vocational School, Amasya, Turkey
*ceren.yavuz@amasya.edu.tr
*Orcid: 0000-0001-7849-4459

Abstract

In this study, a total of 68 raw milk samples were used to investigate the prevalence of Enterobacteriaceae in milk samples obtained from different dairies and supermarkets in the province of Amasya (Turkey), and to determine the antibiotic resistance profile and presence of the *Intl1*, *bla*TEM and *bla*SHV genes. In this study, isolates were obtained using a classical culture technique. The detection of antibiotic resistance profile was carried out using disc diffusion methods. Twelve different antibiotics, including meropenem, cefotaxime, nalidixic acid, ceftriaxone, chloramphenicol, ceftazidime, streptomycin, ampicillin, gentamicin, tetracycline, levofloxacin and trimethoprim-sulfamethoxazole were employed. Single strain polymerase chain reaction (PCR) was created for the detection of extended spectrum beta-lactamase (ESBLs). For these aims, *bla*TEM and *bla*SHV genes were demonstrated by PCR assay. *Intl*1 was determined by using PCR assay. As a result, 50 isolates that belong to the Enterobacteriaceae family were obtained. A total of 41 (82%), 38 (76%), 7 (14%), 6 (12%), 2 (4%) and 1 (2%) isolates were determined to be resistant to ampicillin, trimethoprim-sulfamethoxol, ceftazidime, cefotaxime, meropenem and nalidixic acid as well as ceftriaxone and streptomycin respectively. In addition, 49 (98%), 50 (100%) 49 (98%) and 50 (100%) isolates were determined to be sensitive to chloramphenicol, gentamicin tetracycline and levofloxacin respectively. Among the Enterobacteriaceae isolates, 22 (44%), 6 (12%) and 2 (4%) rates of strains carried the *Intl*1, *bla*SHV and *bla*TEM genes, respectively. In conclusion, the resistance of Enterobacteriaceae isolates that were isolated from milk samples to many antibiotics poses a potential danger in terms of public health.

Keywords: Enterobacteriaceae, antibiotic resistance, *Intl*1, *bla*TEM, *bla*SHV, raw milk

1. Introduction

Milk is a foodstuff that contains almost all nutrients; it has with a unique taste, smell and consistency in a sufficient and balanced manner [1]. However, pathogenic microorganisms can easily contaminate milk regardless of the hygienic conditions and cause the quality of milk to deteriorate [2]. Species that belong to the Enterobacteriaceae family were frequently isolated from milk [3].

The Enterobacteriaceae family is a large and heterogeneous family of Gram-negative bacilli of medical importance. It is a group of facultative anaerobic, non-spore-forming catalase-positive and glucose-fermented microorganisms that are known to cause various infections such as urinary tract infections,

cystitis, pneumonia and bacteremia [3, 4]. Many members of the Enterobacteriaceae family are detected in soil, water, and plants, and a significant proportion of Enterobacteriaceae are detected in the normal intestinal biota of humans and animals. However, there are also members of Enterobacteriaceae that cause hospital and community-borne bacterial infections, especially infections that affect the gastrointestinal system. In addition, Enterobacteriaceae that are detected in various foods cause foods to spoil faster. Although they are associated with fecal contamination, their presence can be seen as an indication that hygiene rules are not observed in post-milking processes as well as an indication environmental contamination [5, 6, 7].

Enterobacteriaceae detected in foods are considered an indicator of hygiene for quality and safety during the

processing of foodstuffs [8]. Members of the Enterobacteriaceae family have an important role in foodborne poisoning [9] Today, food poisoning cases that originate from members of the Enterobacteriaceae family can be fatal. The intense use of antibiotics in medical clinics, animal husbandry, aquaculture and soil cause the selection of resistance genes. Consequently, multidrug resistant (MDR) Enterobacteriaceae emerged [6]. Beta-lactams (mostly extended-spectrum cephalosporins and carbapenems) and fluoroquinolones are among the preferred antibiotic groups in preventing infections caused by Enterobacteriaceae [10]. However, the most important feature of the members of this family is that they produce beta-lactamase enzyme in their body and are resistant to antibiotics that contain beta lactam. Antibiotic resistance increases the cost of treatment of infections caused by bacteria that produce extended-spectrum beta-lactamase (ESBLs). The main genes responsible for ESBL production include TEM (*bla*TEM), SHV (*bla*SHV) and CTX-M (*bla*CTX-M) genes. ESBLs are a group of enzymes that are encoded by genes that are detected on the plasmid that is predominantly common among Enterobacteriaceae. In addition, genes that encode ESBL are associated with mobile genetic elements [11]. Integrons have an important role in the formation of resistance against antimicrobials. In particular, it is associated with the spread of antibiotic resistance to classes 1, 2 and 3 integrons, which are most commonly detected in pathogens. For the continued insertion and deletion of gene cassettes, it is important to obtain the integrase gene (*Intl*l), which is an important part of the integrons [12].

Studies in the literature have focused on the investigation of ESBLs in human derived Enterobacteriaceae isolates; however, few studies investigate the presence of ESBLs in Enterobacteriaceae isolates that are isolated from food [4].
For this purpose, this study aimed to determine (i) the antibiotic resistance profiles of Enterobacteriaceae isolates that are isolated from raw milk samples using a classical culture technique, (ii) the molecular characterization of resistance genes (*bla*TEM and *bla*SHV) and (iii) the presence of integrase (*Intl*1) gene of the isolates.

2. Materials and Methods
2.1. Food Samples

A total of 68 raw milk samples were collected randomly from the different dairy farms between April and August in 2018. Milk samples were brought to the laboratory under the cold chain following purchase.

2.2. Bacteria Isolation and Phenotypic Identification

10 mL of samples were taken and 90 mL of buffered peptone water (Merck, Germany, 107228) was added (10^{-1} dilution) and homogenized. Subsequently, decimal dilutions were made and cultivated on Violet Red Bile Glucose Agar (Merck, Germany, 110275) using classic culture technique. Presumptive colonies (1-2 mm diameter dark pink or red colonies surrounded by precipitate zone by the formation of bile acids around the colony) were subcultured onto Tryptone Soy Agar (TSA, Merck, 22091). After incubation, colonies grown on TSA were transferred to Brain-heart Infusion (BHI, Merck, 53286) broth with 15% glycerol for the next analysis and stored at -20 °C [7].

2.3. Antimicrobial Susceptibility Tests

Antibiotic susceptibility properties of the isolates were determined using the disc diffusion method using Mueller Hinton Agar (MHA; Merck, Germany, RM347.20). Resistance profiles of the obtained isolates were tested against 12 different antibiotics. These antibiotic discs (Bioanalyse Ltd., Turkey): meropenem (MEM, ASD05400, 10 µg), cefotaxime (CTX, ASD01800, 30 µg), nalidixic acid (NA, ASD06000, 30 µg), ceftriaxone (CRO, ASD02300, 30 µg), chloramphenicol (C, ASD02800, 30 µg), ceftazidime (CAZ, ASD02100, 30 µg), streptomycin (S, ASD08400, 10 µg), ampicillin (AM-10 µg), gentamicin (CN, ASD04300, 10 µg), tetracycline (TE, ASD08900, 30 µg), levofloxacin (LEV, ASD04800, 5 µg) and trimethoprim / sulfamethoxazole (TMP / STX, ASD09320, 25 µg). For this purpose, the MHA medium was switched after each Enterobacteriaceae isolate subcultured at TSA was adjusted to a degree of turbidity of 0.5 McFarland. After the plates were incubated at 35° C for 24 hours, the zone diameters formed were measured Clinical and Laboratory Standards Institute (CLSI) criteria [13]. *Escherichia coli* ATCC 25922 was used as a positive control.

2.4. Genomic DNA Extraction and Detection of *Intl* 1, *SHV* and *TEM* Genes

DNA was obtained using the boiling method. For this purpose, first Enterobacteriaceae isolates were removed from -20 °C and passaged in a 5% sheep blood agar and incubated at 24 hours 37 °C. A loopful of isolate was suspended in 500 µl of sterile distilled water for DNA isolation. The solution was kept in boiling distilled water for 10 minutes and then centrifuged at 10,000 x g for 5 minutes. The supernatant containing genomic DNA was taken into a fresh tube [14]. The primer sequences used are given in Table 1.

Table 1. Primer sequences used in this study

Target gene	Primer sequence 5′-3′	Reference
intl 1 F	CCT CCC GCA CGA TGA TC	[15]
intl 1 R	TCC ACG CAC TGT CAG GC	
*bla*SHV F	AAGATCCACTATCGCCAGCAG	
*bla*SHV R	ATTCAGTTCCGTTTCCCAGCGG	[16]
*bla*TEM F	GAGTATTCAACATTTCCGTGTC	
*bla*TEM R	TAATCAGTGAGGCACCTATCTC	

PCR mixture for *Intl* 1 gene; 2.5 mM MgCl$_2$, 1X PCR buffer, 200 µM dNTP, 0.2 µM primer (Forward and Reverse) were completed with 1.25 U Taq Polymerase, 5 µL template DNA and the remaining volume bidistilled water and the final volume was 25 µL. Amplification, 5 minutes pre-denaturation at 94 °C, 30 cycles followed by 1 minute at 94 °C followed by 1.5 minutes of primer at 55 °C, and 1 minute extension at 72 °C and 7 minutes at 72 °C. elongation step was performed (TurboCycler Lite 9020, Blue-Ray, Biotech). PCR products were carried out in an electrophoresis device with 1.5% agarose gel at 90 V for 60 minutes and bands corresponding to 280 bp were evaluated as positive for the *Intl* 1 gene [14, 15, 16].

Mixture of PCR components for bla$_{SHV}$ and bla$_{TEM}$ genes: 2.5 mM MgCl$_2$, 1X PCR buffer, 200 µM dNTP, 0.2 µM primer (Forward and Reverse) were completed with 1.25 U Taq Polymerase, 5 µL template DNA and the remaining volume bidistilled water and the final volume was 25 µL. The thermal reactions were performed as follows: the primary denaturation for 5 min at 95 ºC; followed by 40 cycles as 30 sec for 94 ºC, 30 sec at annealing temperature (58 and 56 ºC respectively), and 30 sec at 72 ºC; and the final extension phase for 5 min at 72 ºC. Amplified samples were done electrophoresis on 2% agarose gel in TBE (Trisma base, Boric acid, EDTA) buffer at 90 V for 60 minutes.

3. Results and Discussion

The presence and number of enteric pathogens that may pose a health hazard to consumers is always taken as an absolute index of fecal contamination of milk and its products. This index is an indication of the lack of health measures during milk production and processing [8]. In this study, 68 raw milk samples that are presented for consumption in Amasya within a period of 4 months were analyzed by a phenotypic method (classical culture technique), and 50 isolates that belong to the Enterobacteriaceae family were obtained. The presence of a high rate of Enterobacteriaceae in the milk samples is consistent with other studies in the literature. The isolates in the milk samples can be attributed to their access to milk during milking in the animal's environment, skin and udders [8, 10, 17]. This situation shows the necessity of taking measures to improve milking and product processing hygiene in farms where milk samples are obtained.

There are reports of high-level antibiotic resistance in community and hospital acquired Enterobacteriaceae species in Turkey [14, 16, 18]. In the last few years, antibiotic-resistant ESBL-producing Enterobacteriaceae have been reported in patients hospitalized in various hospitals in Turkey [19]. Nevertheless, few studies address the antibiotic resistance profile of Enterobacteriaceae species and ESBL production in

food animals. Intense and indiscriminate use of antibiotics in animal production has led to the emergence of many antibiotic-resistant strains, including ESBL production in animals. Therefore, animals not only act as a reservoir but also directly or indirectly transmit these pathogens to humans. For this reason, antibiotic resistance is important in food samples. Antibiotic resistance profiles of Enterobacteriaceae isolates in this study are shown in Table 2.

Table 2. Results of antimicrobial resistance rate of Enterobacteriaceae isolates

Antibiotics	R (n) %	I (n) %	S (n) %
MEM (10 µg)	2/50 (%4)	-	48/50 (%96)
CTX (30 µg)	6/50 (%12)	2/50 (%4)	42/50 (%44)
NA (30 µg)	2/50 (%4)	4/50 (%8)	44/50 (%88)
CRO (30 µg)	1/50 (%2)	3/50 (%6)	46/50 (%92)
C (30 µg)	-	1/50 (%2)	49/50 (%98)
CAZ (30 µg)	7/50 (%16)	3/50 (%6)	40/50 (%80)
S (10 µg)	1/50 (%2)	3/50 (%6)	46/50 (%92)
AM (10 µg)	41/50 (%82)	-	9/50 (%18)
CN (10 µg)	-	-	50/50 (%100)
TE (30 µg)		1/50 (%2)	49/50 (%98)
LEV (5 µg)	-	-	50/50 (%100)
TMP/STX (1,25/23,75 µg)	38/50 (%76)	10/50 (%20)	2/50 (%4)

*MEM: Meropenem, CTX: Cefotaxime, NA: Nalidixic acid, CRO: Ceftriaxone, C: Chloramphenicol, CAZ: Ceftazidime, S: Streptomycin, AM: Ampicillin, CN: Gentamycin, TE: Tetracycline, LEV: Levofloxacin, TMP/STX: Trimethoprim-sulfamethoxazole. R: Resistant, I: Intermediate, S: Sensitive
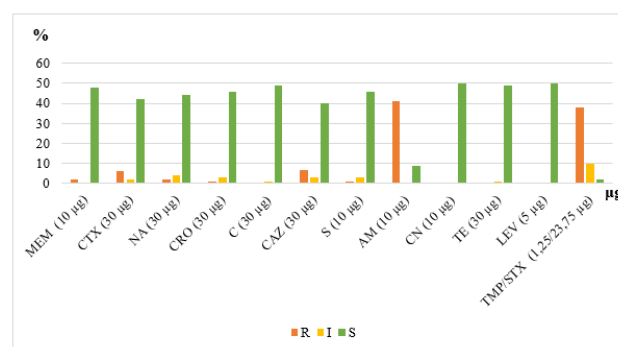
Figure 1. Antibiotic resistance profile of Enterobacteriaceae isolates (R= resistant, I =intermediate, S= Sensitive)

It was determined that 50 (100%) of the isolates were susceptible to levofloxacin and gentamicin; 49 (98%) of the isolates were susceptible to chloramphenicol and also tetracycline; and 48 (96%) of the isolates were susceptible to meropenem (Fig 1).

In contrast to our results, which showed that 76% of Enterobacteriaceae isolates were resistant to trimethoprim-sulfamethoxazole, Vitas et al. found that only 26.5% of Enterobacteriaceae isolates from chicken were resistant to trimethoprim-sulfamethoxazole, and Seedy et al found that 97.6% of Enterobacteriaceae isolates from milk were susceptible to trimethoprim-sulfamethoxazole [12, 18]. Some Enterobacteriaceae strains isolated from raw milk samples exhibited multiple resistance profiles against different antibiotic groups similar to finding reported by other authors [22].

When the isolates in this study were evaluated in terms of multiple antibiotic resistance, the following resistance outcomes were observed 2 (4%) isolates were resistant to 5 different antibiotics (Meropenem, Ceftriaxone, Streptomycin, Ampicillin, and Trimethoprim-sulfamethoxazole); 1 (2%) isolate was resistant to 5 different antibiotics (Ceftazidime, Ampicillin, Trimethoprim-sulfamethoxazole, and Cefotaxicin); 1 (2%) isolate was resistant to 4 different antibiotics (Streptomycin, Nalidixic acid, Ampicillin, and Trimethoprim-sulfamethoxazole), 2 (4%) isolates were resistant to 3 different antibiotics (Ceftriaxone, Ampicillin, and Trimethoprim-sulfamethoxazole) and 1 (%2) isolate was resistant antibiotics to 3 different antibiotics (Tetracycline, Ampicillin, and Trimethoprim-sulfamethoxazole) (Table 3). Increasing resistance to antibiotics in environmentally derived bacteria due to intensive use of antibiotics or contamination of their waste into the environment is an important problem that threatens public health [23, 24].

Table 3. Distribution of multiple drug resistant Enterobacteriaceae isolates

Number of isolates	Ratio (%)	Number of antibiotics	Antibiotics names
2	4	5	Meropenem, Ceftriaxone, Streptomycin, Ampicillin, Trimethoprim/sulfamethoxazole
1	2	5	Ceftazidime, Ampicillin, Trimethoprim/sulfamethoxazole, Cefotaxime, Nalidixic acid
1	2	4	Streptomycin, Nalidixic acid, Ampicillin, Trimethoprim/sulfamethoxazole
2	4	3	Ceftriaxone, Ampicillin, Trimethoprim-sulfamethoxazole
1	2	3	Tetracycline, Ampicillin, Trimethoprim-sulfamethoxazole

Antibiotic resistance genes are transferred by the horizontal transfer of plasmids, transposons, and integrons [25]. In this study, among the studied strains, 22 isolates (44%) contained $Int1$ while 28 isolates (56%) were negative for the $Int1$ gene. In addition, all isolates that carry the $Int1$ gene were determined to be resistant to ampicillin and trimethoprim-sulfamethoxazole. Thongkao and Sudjaroen, investigated whether a correlation exists between the presence of the $Int1$ gene and antibiotic resistance acquisition by the Enterobacteriaceae isolate [26]. Similar to our study, they found that all isolates with the positive $Int1$ gene were also resistant to ampicillin. Among the 22 isolates with the $Int1$ gene, 7 isolates were MDR. In the light of this information, antibiotic resistance properties of Enterobacteriaceae isolates can be associated with a class 1 integron.

One of the most important consequences of the introduction of beta-lactams is the plasmid mediated spread of beta-lactamases. It is reported that TEM-1 is the most common plasmid-mediated enzyme in the Enterobacteriaceae species. It has been reported that this enzyme is frequently encountered in ampicillin-resistant isolates [25]. In this study, all 50 isolates were PCR performed to detect beta-lactamase genes. blaSHV and blaTEM genes were detected in 2 (4%) isolates and 6 (12%) isolates, respectively. In addition, all blaTEM positive isolates were determined to be resistant to ampicillin. In China a study by Ye et al. revealed that the frequency of blaTEM and blaSHV were 81.9%, 38.9%, respectively [4]. In another study of Turkey by Pehlivanoğlu et al. the frequency of blaTEM and blaSHV were 77.4% and 9.7%, respectively [26]. In a survey performed by Shahid et al. the frequencies of blaSHV and blaTEM among ESBL-producing strains were 13.7%, and 10.9%, respectively [17]. In research in Turkey, Tekiner and Özpınar showed that 20% of the isolates were positive for both blaSHV and blaTEM [19].

4. Conclusion

These results show that the prevalence of blaTEM and blaSHV genotypes is high in ESBL-producing Enterobacteriaceae isolates. Considering the data obtained in this study, it is seen that the isolates carrying the blaSHV, blaTEM and $Int1$ encoding genes are interrelated. Accurate detection of food pathogens that originate from MDR Enterobacteriaceae and the increasing prevalence of beta-lactamase and determination of antibiotic susceptibility patterns are important. To prevent the emergence of drug-resistant strains, attention should be paid to the use of antibiotics in the growth and feeding conditions of food animals.

Author's Contributions

Ceren Başkan: drafted the manuscript, compiled information from the literature, and designed the figures and tables.

Ethics

There are no ethical issues in the publication of this manuscript.

References

1. Yılmaz, B, Tosun H. 2013. The natural antimicrobial systems in milk and their utilization in food industry. *Celal Bayar University Journal of Science*; 8(1): 11-20.

2. Şen, A. 2006. Çiğ sütte *Pseudomonas aeruginosa* sayılması için modifikasyonları üzerine çalışmalar" Yüksek Lisans Tezi A: Ü. Fen Bilimleri Enstitüsü Ankara.

3. Mitchell, J, Yehuda, C. 2008. Carbapenem-resistant Enterobacteriaceae. A potential threat. *Journal of the American Medical Association*; 300(24): 2911–2913.

4. AlTamimi, M, AlSalamah, A., AlKhulaifi, M, AlAjlan, H. 2017. Comparison of phenotypic and PCR methods for detection of carbapenemases production by Enterobacteriaceae, *Saudi Journal of Biological Sciences*; 24(1): 155-161.

5. Jarzab, A, Gorska-Fraczek, S, Rybka, J, Witkowaka, D. 2011. Enterobacteriaceae infection-diagnosis, antibiotic resistance and prevention. *Postępy Higienyi Medycyny Doświadczalnej*; 16(65): 55–72.

6. Ye, Q, Wu, Q, Zhang, S, Zhang, J, Yang, G, Wang, J, Xue, L, Chen, M. 2018. Characterization of extended-spectrum β-lactamase-producing Enterobacteriaceae from retail food in China. *Frontiers in microbiology*; 9: 1-12.

7. Tasci, F. 2011. Microbiological and chemical properties of raw milk consumed in Burdur. *Journal of Animal and Veterinary Advances*; 10(5): 635-641.

8. Kornacki, JL, Johnson, JL. Enterobacteriaceae, coliforms, and *Escherichia coli* as quality and safety indicators. In: Downes P, Ito K (eds) Compendium of methods for the microbiological examination of foods. 4th edn. APHA, Washington, 2001; pp. 69–82.

9. Mullane, NR, Murray, J, Drudy, D, Prentice, N, Whyte, P, Wall, PG, Parton, A, Fanning, S. 2006. Detection of *Cronobacter sakazakii* in dried infant milk formula by cationic-magnetic-bead capture. *Applied Environmental Microbiology*; 72(9): 6325–6330.

10. Kačániová, M, Terentjeva, M, Godočíková, L, Puchalski, C, Kluz, M, Kordiaka, R, Kunová, S, Haščí,k P. 2017. Rapid identification of Enterobacteriaceae in milk and dairy products with the matrix-assisted laser desorption ionization–time of flight mass spectrometry (MALDI-TOF MS). *Animal Science and Biotechnologies*; 50: 41-46.

11. Schultsz, C, Geerlings, S. 2012. Plasmid-mediated resistance in Enterobacteriaceae: changing landscape and implications for therapy. *Drugs*; 72(1): 1-16.

12. Vitas, AI, Nai,k D, Pérez-Etayo, L, González, D. 2018. Increased exposure to extended-spectrum β-lactamase-producing multi drug resistant Enterobacteriaceae through the consumption of chicken and sushi Products. *International Journal of Food Microbiology*; 269: 80–86.

13. Tekiner, IH, Özpinar, H. 2016. Occurrence and characteristics of extended spectrum beta-lactamases-producing Enterobacteriaceae from foods of animal origin. *Brazilian Journal of Microbiology*; 47(2): 444–451.

14. Clinical and Laboratory Standards Institute (CLSI). Performance standards for antimicrobial susceptibility testing. twentieth informational supplement. 2016; M100-S20, 30, 1 USA.

15. Bass, L, Liebert, CA, Lee, MD, Summers, AO, White, DG, Thayer, SG, Maurer, JJ. 1999. Incidence and characterization of integrons, genetic elements mediating multiple-drug resistance, in avian *Escherichia coli. Antimicrob Agents Chemother*, 43(12): 2925-2929.

16. Estaji, M, Tabasi, M, Sadeghpour, HF, Khezerloo, JK, Radmanesh, A, Raheb, J, Ghadirzadeh, MR, Tabatabaei, A. 2019. Genotypic identification of *Pseudomonas aeruginosa* strains isolated from patients with urinary tract infection. *Comparative ımmunology microbiology & Infectious Disease;* 65: 1-20.

17. El Zubeir, IEM, Ahmed, MIA. 2007. The hygienic quality of raw milk produced by some dairy farms in Khartoum State, Sudan. *Research Journal of Microbiology*; 2(12): 988-991.

18. El-Diasty, EM, El-Kaseh, RM. 2009. Microbiological monitoring of raw milk and yoghurt samples collected from El-Beida city. *Arab Journal of Biotechnology*; 12(1): 57-64.

19. Mishra, M, Panda, S, Barik, S, Sarkar, S, Singh, DV, Mohapatra, H. 2020. Antibiotic resistance profile, outer membrane proteins, virulence factors and genome sequence analysis reveal clinical isolates of *Enterobacter* are potential pathogens compared to environmental isolates. *Frontiers in Cellular and Infection Microbiology*; 10(54): 54-67.

20. Seedy, FRE, Samy, AA, Khairy, EA, Koraney, AA, Salam, HHS. 2020. Molecular determinants of multiple antibiotic resistant *E. coli* isolated from food of animal origin. *Advances in Animal and Veterinary Sciences*; 8(4): 347-353.

21. Dixit, S, Gupta, S. 2019. Antibiogram of microbes associated with enteric infection targeting incidences of multidrug resistance. *International Knowledge Press*; 12, 41-45.

22. Leverstein, van Hall, MA, Box, ATA, Blok, HEM, Paauw, A Fluit, AC, Verhoef, J. 2001. Evidence of extensive interspecies transfer of integron-mediated antimicrobial resistance genes among multidrug resistant Enterobacteriaceae in a clinical setting. *Journal of Infectious Diseas;* 186(1): 49-56.

23. Thongkao, K, Sudjaroen, Y. 2019. Beta-lactamase and integron-associated antibiotic resistance genes of *Klebsiella pneumoniae* isolated from *Tilapia fishes* (*Oreochromis niloticus*). *Journal of Applied Pharmaceutical Science;* 9(1): 125-130.

24. Özgümüş, OB, Tosun, AF, Kılıç, AO, Ertürk, M. 2006. Carriage of mobilizable plasmid-mediated β-lactamase gene in ampicillin-resistant *Escherichia coli* strains with origin of normal fecal flora. *Turkish Journal of Medical Sciences*; 36(5): 307–314.

25. Pehlivanoğlu F, Turutoğlu H, Öztürk D, Yardımcı H. 2016. Molecular characterization of ESBL-Producing *Escherichia coli* isolated from healthy cattle and sheep. *Acta Veterinaria-Beograd*. 66(4), 520-533.

26. Shahid, M, Singh, A, Sobia, F, Rashid, M, Malik, A, Shukla, I, Khan, HM. 2011. blaCTX-M, blaTEM, and blaSHV in Enterobacteriaceae from North-Indian tertiary hospital: high occurrence of combination genes. *Asian Pacific Journal of Tropical Medicine*; 4(2): 101-105.

Celal Bayar University Journal of Science

Numerical Simulation on Balistic Performance of SiC/Light Metal Laminated Composite Armor against .30 APM2

Saim Kural[1*] iD, Mehmet Ayvaz[2] iD

[1*] Department of Mechanical Engineering, Manisa Celal Bayar University, Manisa 45140, Turkey
[2] Vocational School Of Manisa Technical Sciences, Manisa Celal Bayar University, Manisa 45140, Turkey
*saim.kural@cbu.edu.tr
*Orcid: 0000-0003-1722-6252

Abstract

Ceramic/metal laminated composite armor systems have great importance and potential in defence technology due to their high ballistic performance and lightweight. In this study, it was aimed to determine the ballistic performances, limits, and perforation types of light metals (with densities below 5.0 g/cm^3) used as ductile backing plates in laminated composite armor systems. In the numerical analysis, SiC tiles of 5 and 10 mm thickness were used as the front layer. Al5083-H116, Mg AZ31B, and Ti6Al4V light metal alloys in different thicknesses were used as the backing layer. While using the Johnson and Holmquist (JH-1) material model in SiC ceramic tiles, the Johnson-Cook (JC) material model was applied for ".30 APM2" bullet components and metal layers. The analyzes were performed with Ansys/Autodyn software. As a result of the simulations, among all the laminated armor systems providing full protection against ".30 APM2" ballistic threats with a collision speed of 878 m/s, the lowest areal density was determined as 54.245 kg/m^2 in 10 mm SiC/5 mm Ti6Al4V laminated composite armor.

Keywords: Ballistic Performance; Laminated Composite; Finite Element Analysis; Ti6Al4V; Mg AZ31B.

1. Introduction

Steel and its alloys are widely used as armor material due to their low cost, strength, and hardness that can be improved by heat treatments. However, in addition to performing ballistic protection, armor material should not restrict the mobility of target to move away from repeated ballistic threats. Also, reducing the weight of the armor can help decrease energy.[1]. For the use of low weight materials as armor, ballistic performances of light metals are examined and tried to be developed. For this purpose, the most frequently studied alloys are age-hardenable aluminum alloys.

Another aluminum alloy known to be widely used in armored vehicles is AA5083, whose strength can be increased by deformation hardening [2]. Borvik et al. investigated the ballistic behavior of 15-30 mm thick AA5083 armors with a diameter of 20 mm and a length of 98 mm with a conical tip steel projectile by experimental studies [3]. Ballistic limit speeds of AA5083 armors of 15, 20, 25, and 30 mm thickness were 216.8, 249.0, 256.6, and 309.7 respectively. In the study carried out with the finite element method using

the same parameters in the empirical study of Borvik et al. [3], ballistic limit velocities were calculated by showing a maximum ~5 % deviation to experimental results [4]. In the tests, ballistic limit speeds of AA5083 plates with 20, 2x20, and 3x20 mm layer numbers and thicknesses were obtained as 492, 722, and 912 m/s, respectively, against 7.62 mm APM2 bullets [5]. Magnesium alloys, especially Mg AZ31, whose density is 35 % lower than aluminum, have a high potential for light armor systems [6]. Moreover, in experimental studies, the ballistic limit velocities of Mg AZ31 and AA5083 armor plates with the same field density (~ 135.2 kg/m^2) were determined as 863 and 853 m/s, respectively [7]. Another light metal used as armor material is titanium alloys [8]. By using Ti6Al4V alloy armor, ~30-40% weight reduction is achieved compared to Rolled Homogeneous Armor (RHA) usage [9]. Also, like steel alloys, it is possible to increase the ballistic performances of titanium alloys [10].

In ballistic protection systems, the desired ballistic protection level cannot be achieved against most ballistic threats by using monolithic metallic armor. For this reason, laminated composite armor plates are used.

laminated composite armors are obtained by placing ceramic tiles on the impact surface of the deformable and energy absorber armor materials [11]. Determining the penetration and perforation behavior of laminated composite armors with empirical ballistic tests is very costly. For this reason, mathematical models are widely used in the solution of this ballistic physical problem. In ceramic materials, the fracture conoid formed by the impact of the bullet was first modeled by Florence [12]. Alekseevskii [13] and Tate [14] mathematically modeled penetration of the bullet into the armor plate. Analytical models explaining the ballistic behavior of the backing plate and the deformation occurring in this plate were developed by Woodward [15] and Reijer [16]. The penetration stages of the projectile into ceramic-metal laminated composite armors were modeled by Zaera and Sanchez-Galvez [17] based on the models of Alekseevskii [13], Tate [14], Woodward [15] and Reijer [16]. Chocron and Galvez [18] developed models for composite armors with ceramic/polymer composite layers. Feli et al. [19] developed an analytical model to explain the ballistic behavior of ceramic/metal composite armors, considering the deformation and erosion of the projectile tip.

SiC is widely used in ballistic protection systems. However, there are insufficient models in the literature reporting how ballistic performance of SiC/metal laminated composite armor. The ballistic behavior and performance of either monolithic SiC tiles [20] or SiC/metal composite armors against non-standard projectiles were modeled and investigated [21]. Also, to date, the ballistic performance, especially Ti6Al4V and Mg AZ31B light metal alloys, with ceramic layering, has not been reported. In this study, ballistic behavior and performance of SiC/light metal alloy (AA5083, Ti6Al4V, Mg AZ31B) laminated composite armor plates against standard ".30 APM2" were analyzed and optimum thicknesses of the layers were determined.

2. Numerical Methods and Materials Models

Finite element analyzes (FEA) of impact tests were carried out on a 2D axisymmetric model using ANSYS AutoDYN software. The dimensions of our model can be seen in Figure 1. For model, the armor plates were considered fixed from the right-hand side. In addition, for analysis precision, the regions where high collision energy took place were divided into 5 surfaces to create different sized mesh. Mesh element sizes and mesh structures can be seen in Figure 2. This mesh structure and optimizations were determined by obtaining results consistent with experimental results in Borvik at al.[4]. In armors with various thickness, the number of mesh elements and nodes for each thickness was modeled as different. However, since the size of the mesh element was determined for each field with "behavior: hard", the same size element was used for that area.
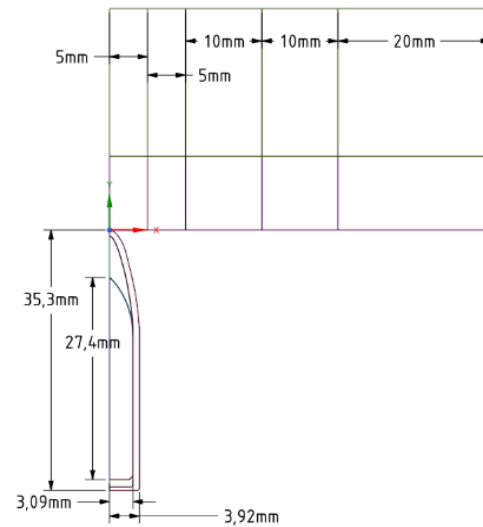
Figure 1. Model dimensions
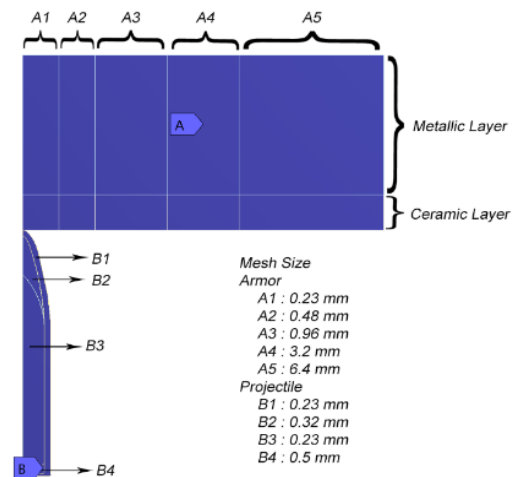
Figure 2. Mesh element sizes and mesh structure

Johnson-Cook strength model was used for Steel 4340 projectile core, and Al 5083-H116 targets in explicit analyses. This model explains the material behavior under penetration conditions, encountered in problems related to high temperature - stress - strain rate and hyper velocity effects [22]. This model is widely used to solve ballistic problems.The Steinberg-Guinan strength model calculates the yield modulus based on effective plastic deformation, pressure, and temperature, which increases with increasing pressure and decreasing with increasing temperature. Table 1 shows the material properties of the projectile and targets for the models used. Material models were used from AutoDYN standard material library. Johnson-Holmquist failure model were used for SiC, Johnson-Cook failure model were used for Steel 4340 and Al5083-H116. For failure models, values in the AutoDYN material library were used.

S. Kural

Table 1. Mechanical properties of comparison model

Material Name	Reference Density (kg/m3)	Equation of State		Strength Model	
		Linear		**Johnson-Cook**	
		Bulk Modulus(MPa)	5.833×10^4	Shear Modulus(MPa)	2.692×10^4
		Reference Temperature(K	293.00	Yield Stress(MPa)	1.67×10^2
		Specific Heat(J/kgK)	910.000122	Hardening Constant(MPa)	5.96×10^2
		Thermal Cond. (J/mKs)	117.00	Hardening Exponent.	0.551
Al5053-H116	2700			Strain Rate Constant.	0.001
				Thermal Softening Exponent.	0.859
				Melting Temperature(K).	893
				Ref. Strain Rate(/s).	1
				Strain Rate Correction.	1st Order
		Linear		**Johnson Cook**	
		Bulk Modulus(MPa)	1.59×10^5	Shear Modulus(MPa)	7.7×10^4
		Reference Temperature(K	300.00	Yield Stress(MPa)	7.92×10^2
		Specific Heat(J/kgK)	477.000092	Hardening Constant(MPa)	5.1×10^2
				Hardening Exponent	0.26
Steel 4340	7830			Strain Rate Constant	0.014
				Thermal Softening Exponent	1.03
				Melting Temperature(K)	1793
				Ref. Strain Rate(s^{-1})	1
				Strain Rate Correction	1st Order
		Shock			
Brass	8450	Gruneisen Coefficient	2.04	None	
		Parameter C1($m\,s^{-1}$)	3.726×10^3		
		Parameter S1	1.434		
		Shock		**The Steinberg-Guinan**	
		Gruneisen Coefficient	2.74	Shear Modulus(MPa)	8.6×10^3
		Parameter C1($m\,s^{-1}$)	2.006×10^3	Yield Stress(MPa)	8.0×10^2
		Parameter S1	1.429	Maximum Yield Stress(MP	1×10^2
				Hardening Constant	110
Lead	11340			Hardening Exponent	0.52
				Derivative dG/dP	1
				Deriv. dG/dT (MPa K^{-1})	−9.976
				Deriv. dY/dP	9.304×10^{-4}
				Melting Temperature (K)	760
		Polynomial		**Johnson-Holmquist**	
		Parameter A1(kPa)	2.2×10^8	Shear Modulus(kPa)	1.935×10^8
SiC	3215	Parameter A2(kPa)	3.61×10^8	Model	JH-1
		Parameter T1(kPa)	2.2×10^8	HEL(kPa)	1.17×10^7
		Ref. Temp. (K)	293	S1(kPa)	7.1×10^6
				P1(kPa)	2.5×10^6
				S2(kPa)	1.22×10^7
				P2(kPa)	1×10^7
				Strain Rate Constant	0.009

Detailed results for comparison, were shown in Table 2. The results in the table clearly show that the FEM analyzes performed is quite compatible with the experimental results. Only one result of FEM analyses (480 m/s striking velocity case), residual velocity was obtained 110.37 m/s, while in the experimental result, the projectile was stopped in response to this speed. This result is expected because the Johnson-Cook strength model is more suitable for high speeds.

Table 2. Comparison of this study with the experimental study of Borvik et al. [5]

Armor			Striking Velocity [m/s]	This Study Residual Velocity [m/s]	Børvik et al.,2010 Residual Velocity [m/s]	% Difference Between Simulation and Experiment
1st Metal Layer Thickness [mm]	2nd Metal Layer Thickness [mm]	3rd Metal Layer Thickness [mm]				
20	0	0	480.0	110.37	0.0000000	N/A
20	0	0	822.4	701.15	694.3000000	0.986605214
20	20	0	669.8	0.00	0.0000000	0
20	20	0	866.3	472.90	486.2000000	-2.735499794
20	20	20	905.6	0.00	0.0000000	0
20	20	20	955.7	254.23	255.4000000	-0.458104933

After correction of model and mesh structure, different armor materials tested against ".30 APM2" ballistic threats with a collision speed of 878 m/s. The ballistic performances, limits, and perforation types of light metals (with densities below 5.0 g/cm3) used as ductile backing plates in laminated composite armor systems. In the numerical analysis, SiC tiles of 5 and 10 mm thickness were used as the front layer. Al5083-H116, Mg AZ31B, and Ti6Al4V light metal alloys in different thicknesses were used as the backing layer. While using the Johnson and Holmquist (JH-1) strength model in SiC ceramic tiles, the Johnson-Cook (JC) strength model was applied for ".30 APM2" bullet core and St 4340, von Mises strength model was applied for Mg AZ31B, and Steinberg Guinan strength model was applied for Ti6Al4V metal layers.

Johnson-Holmquist strength model uses to model brittle materials (glass, ceramics) subjected to large pressures, shear strain, and high strain rates. This model is a combined plasticity and damage model. According to this model, yielding is based on micro-crack growth instead of dislocation movement (metallic plasticity). The von Mises strength model has a fixed value of yield stress just as the original Von-Mises precursors. As a result, the Von-Mises cylinder has a fixed radius. The conditions lying in the cylinder are flexible and the conditions on the surface of the cylinder are plastic.

$$(\sigma_1 - \sigma_2)^2 + (\sigma_2 - \sigma_3)^2 + (\sigma_3 - \sigma_1)^2 = 2Y^2 \quad \textbf{(2.1)}$$

Failure criteria were chosen Hydro (Pmin) for the Mg AZ31 and Ti6AL4V, Johnson Holmquist for SiC, Johnson Cook for Al5083-H116. .

3. Results and Discussion

In Figure 3a, the velocity change of the projectile can be seen for 5mm SiC/0, 10, 15, 20, 25, and 30 mm Al5083-H116 laminated composite armors. With a small loss of velocity, the bullet pierced the 5 mm thick SiC tile at ~ 10 µs. Laminated composites with 10, 15, 20, and 25 mm thick Al5083-H116 backing armors were perforated

by ".30 APM2" at approximately 45, 50, 65, and 80 µs, respectively. The velocity drop of the projectiles in the range of 0-15 µs, were calculated similarly for all laminated composite armors. Penetration stages of the projectile in the 5 mm SiC/30 mm Al5083 laminated composite armor plate is given in Figure 4b. In this figure, deformations occurring in the range of 0-12.005 µs can be seen in the projectile and laminated composite armor. As can be seen from this figure, 0-15 µs was the time interval during which the deformation of the projectile nose and the formation of ceramic fracture conoid was formed. The phenomenon of the ceramic cone is the main reason for the ballistic success of ceramic/metal composite armor plates [23-25].

Fracture conoid spreads ballistic energy over a larger area on the backing plate. As a result, elastic and plastic work increases. Also, with the use of high hardness ceramic front layer, the projectile loses its ballistic efficiency and penetration ability as a result of deformation on the projectile nose. In some cases, the projectile breaks into pieces and kinetic energy decreases as a result of mass loss. As a result, ceramic/metallic laminations both reduce the kinetic energy of the projectile and increase the energy required for perforation. In all analyzes carried out, the formation of the ceramic cone was fully modeled. Thanks to the ceramic cone formation, 5 mm SiC/30 mm Al5083-H116 laminated composite armor stopped ".30 APM2" projectile at ~94 µs.

The backing plate is brittle but high strength or ductile but low strength has negative consequences for ballistic protection. The brittle backing plate breaks into several pieces after a ballistic collision. The low-strength, tough backing plate does not show sufficient ballistic strength and is perforated by the projectile Therefore, toughness and strength must be optimized for full ballistic strength [26]. For this reason, 5 mm SiC/Mg AZ31B armor against ".30 APM2" could provide full ballistic protection almost twice as thick as 5mm SiC/Al5083-H116 laminated composite armor. Figure 4a shows the velocity change of the bullet for 5mm SiC/0-55 mm Mg

S. Kural

(a)

(b)
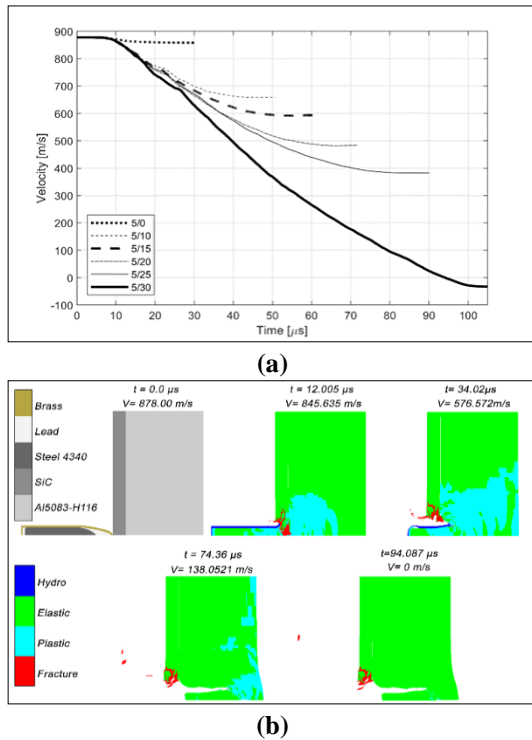
Figure 3. The velocity change of projectile as a function of time for 5 mm SiC/0-30 mm Al5083-H116 laminated composites (a) and penetration process of the projectile in 5 mm SiC/30 mm Al5083 laminated composite armor (b)

(a)

(b)
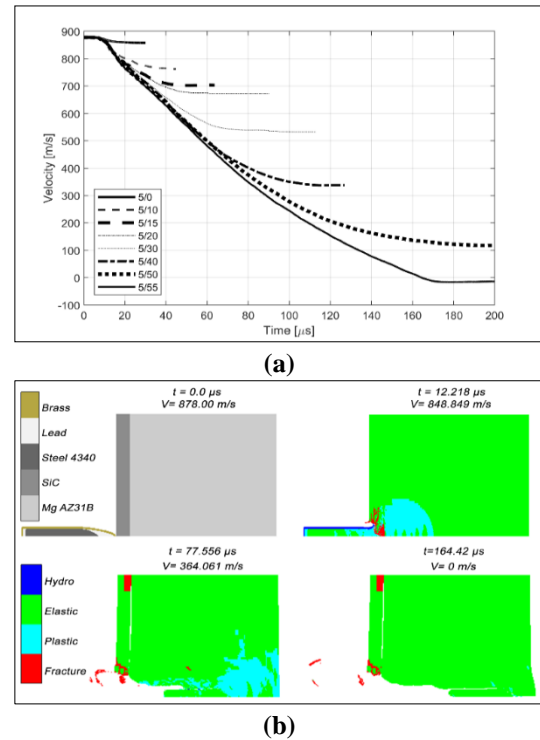
Figure 4. The velocity change of projectile as a function of time for 5 mm SiC/0-55 mm Mg AZ31B laminated composites (a) and penetration process of the projectile in 5 mm SiC/55 mm Mg AZ31B laminated composite armor (b)

AZ31B armor plates. The projectile was stopped at 164.42 µs using a 55 mm Mg AZ31B backing layer. Figure 6b shows the penetration of the projectile in 5 mm SiC/55 mm Mg AZ31B composite armor. In the first 12 µs, similar to the 5 mm SiC/30 mm Al5083-H116 composite armor, the velocity drop of the projectile was very low due to the low energy required for the fracture of the ceramic tile. In Fig. 4b, it is seen that the brass jacket of the projectile was stripped from the steel core.

Figure 5a shows the velocity change of the projectile for 5 mm SiC/0-10 mm Ti6Al4V armor. As shown in the graphic, the projectile was stopped at 61.3 µs by a 5 mm SiC/10mm Ti6Al4V composite armor. This thickness is less than half the limit thickness of the SiC/Al5083-H116 composite armor to protect against ".30 APM2" threat. Using Ti6Al4V, a 75 % thickness reduction was achieved compared to the Mg AZ31B backing layer. The penetration of the projectile in the 5 mm SiC/10 mm Ti6Al4V laminated composite armor plate is given in Fig.5b.

As a result of the bullet hitting the ceramic tile, a ceramic facture conoid was formed. As seen from the light blue colors representing plastic deformation, plastic deformations occurred in the bullet during penetration and the bullet was eroded.

(a)

(b)
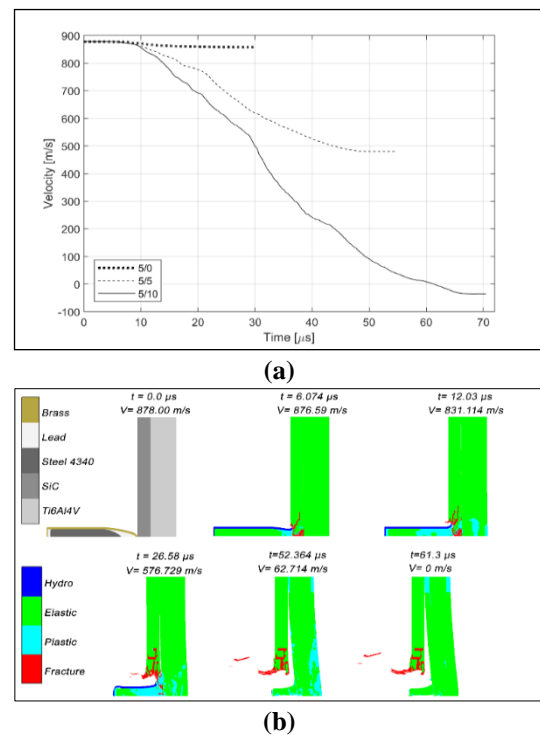
Figure 5. The velocity change of projectile as a function of time for 5 mm SiC/0-10 mm Ti6Al4V laminated composites (a) and penetration process of the projectile in 5 mm SiC/10 mm Ti6Al4V laminated composite armor (b)

Al5083-H116 and Mg AZ31B metallic armor plates were locally formed with plastic deformations, resulting in penetration and perforation in that local area. On the Ti6Al4V armor plate, plastic deformation and deflection occurred in almost the entire cross-sectional length. Thus, plastic work increased, and the kinetic energy of the bullet could be absorbed.

In Figure 6, residual velocities of the projectile are given for laminated composite armor with various thick Mg AZ31B, Al5083-H116 and Ti6Al4V backing layer. The projectile exited the unlayered 5mm SiC ceramic target at a speed of 858.11 m/s. Residual velocities of the projectile were calculated as 480.39 m/s of 5 mm SiC/5 mm Ti6Al4V composite armor target. From 5 mm SiC/10, 15, 20 and 25 mm Al5083-H116 composite targets, residual velocities of projectiles were respectively, 657.54, 591.7, 481. 87 and 382.57 m/s. After perforation of the 20 mm thick Al5083-H116 monolithic armor plate, the residual velocity of the projectile which had an initial velocity of 822.4 m/s was experimentally determined as 694.3 m/s by Borvik et al. [5]. In the same study, for 3x20 mm thick Al5083-H16 armor plates, the ballistic limit velocity of the APM2was reported as 901 m/s (calc) and 912 m/s (exp). In the analyzes, it was observed that 5 mm SiC/30 mm Al5083-H116 armors stopped ".30 APM2" with the first speed of 878 m/s. For 5 mm SiC/10, 15, 20, 30, 40 and 50 mm Mg AZ31B laminated composite targets, the residual velocity of the projectile was calculated as 762.41, 702.17, 672.79, 532.49, 337.91 and 119.19 m/s, respectively. In the previous study, it was determined that the limit speed of the ".30 APM2" bullet for the 86.48 mm thick Mg AZ31B armor plate was 863 m/s [7]. In this study, ".30 APM2" was stopped by a 5 mm SiC/55 mm Mg AZ31B target.

In Figure 7, some perforated laminated composite armor plates are given. The perforation type in 20 mm thick Al5083-H116 and Mg AZ31B backing layers, was ductile hole growth type. This type of puncture is especially seen in materials of medium hardness and thickness [27]. It was also found that the inlet hole was larger than the outlet hole, especially in the 20mm Al5083-H116 backing layer. This phenomenon occurs as a result of striping the brass jacket in a similar way in the literature [28, 29]. Ductile plugging type perforation occurred in a 5 mm SiC/5 mm Ti6Al4V armor plate. In Figure 8, plugging perforation stages and tensile stresses are given. In plugging type puncture, adiabatic shear bands occurring under the high strain rate of the material are effective. Another factor that causes this puncture type is a blunt bullet shape [27]. As a result, the bullet nose became blunt. After dishing, shearing and tensile stress occurred in the local area where the corners of the bullet nose touched the target (Fig. 8). The local area where tensile stress occurred was horizontally and circumferentially cracked. Finally, the target was perforated as a ductile plugging type.
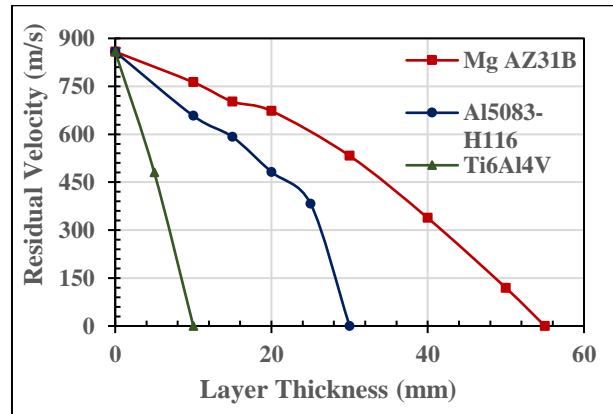
Figure 6. Residual velocity versus backing layer thickness for 5 mm SiC tiles backed with various light metal layers
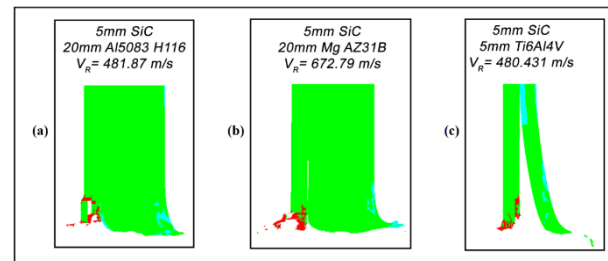
Figure 7. Perforation types of 5 mm SiC/light metal laminated composites: (a) 20 mm Al5083 H116, (b) 20 mm Mg AZ31B and (c) 5 mm Ti6Al4V backing layers
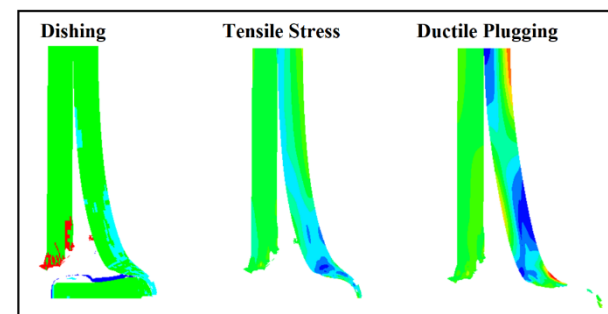
Figure 8. Perforation types of 5 mm SiC/light metal laminated composites: (a) 20 mm Al5083 H116, (b) 20 mm Mg AZ31B and (c) 5 mm Ti6Al4V backing layers

In Ti6Al4V alloy armors, petalling and especially plugging perforation types are determined as common puncture types[10].

In Figure 9a, the velocity change graphs of ".30 APM2" for 10 mm SiC /0-15 mm Al5083-H116 composite armors are given. After losing more than half of its velocity, 30 APM2 perforated composite armor at approximately 70 µs when 10 mm thick Al5083-H116 was used. When the backing layer thickness of Al5083-H116 was increased to 15 mm, the ".30 APM2" projectile was stopped by the composite armor plate at

96.2 μs. In Figure 9b, the penetration stages of the ".30 APM2" projectile in this armor plate can be seen. Compared to 5 mm SiC/Al5083-H116 composite armors, the ceramic fracture conoid formed in 10 mm SiC/15 mm Al5083-H116 composite armor was larger. Besides, as a result of the transfer of momentum from the fracture conoid base to the backing layer and the spread of the collision energy over a wider area, plastic deformation occurred on almost all of the front surface of the Al5083-H116 backing layer.

(a)

(b)
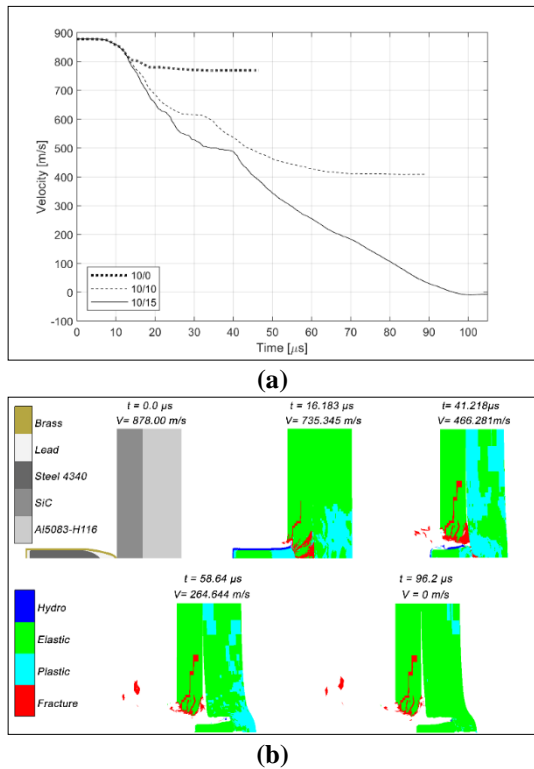
Figure 9. The velocity change of projectile as a function of time for 10 mm SiC/0-20 mm Al5083-H116 laminated composites (a) and penetration process of the projectile in 10 mm SiC/20 mm Al5083 laminated composite armor (b)

In Fig. 10a, the velocity change of the ".30 APM2" can be seen for 10 mm SiC/0-25 mm Mg AZ31B laminated composite armors. Composite armor using 10 mm Mg AZ31B as the backplate could not stop the projectile and the projectile perforated the armor at approximately 50 μs. When the Mg AZ31B backing layer thickness was 20 mm, the projectile was stopped at 176.15 μs. However, as seen in Fig. 10b, composite armor was perforated even though the bullet had stopped. Therefore, the analysis was carried out for 25 mm thick Mg AZ31B. In this analysis, it was calculated that the projectile was safely stopped by composite armor at 90.55 μs. To stop the ".30 APM2" projectile, it was determined that 5 mm SiC tile should be supported with 55 mm thick Mg AZ31B (Fig. 10). it can be seen in Fig 10c that compared to 5 mm SiC/55 mm MgAZ31B composite armor (Fig. 6b), the projectile is more eroded

and deformed by 10 mm SiC/25 mm Mg AZ31B composite armor. As a result, the bullet lost its kinetic energy and perforation ability and could not pierce 25 mm thick Mg AZ31B armor.

(a)

(b)

(c)
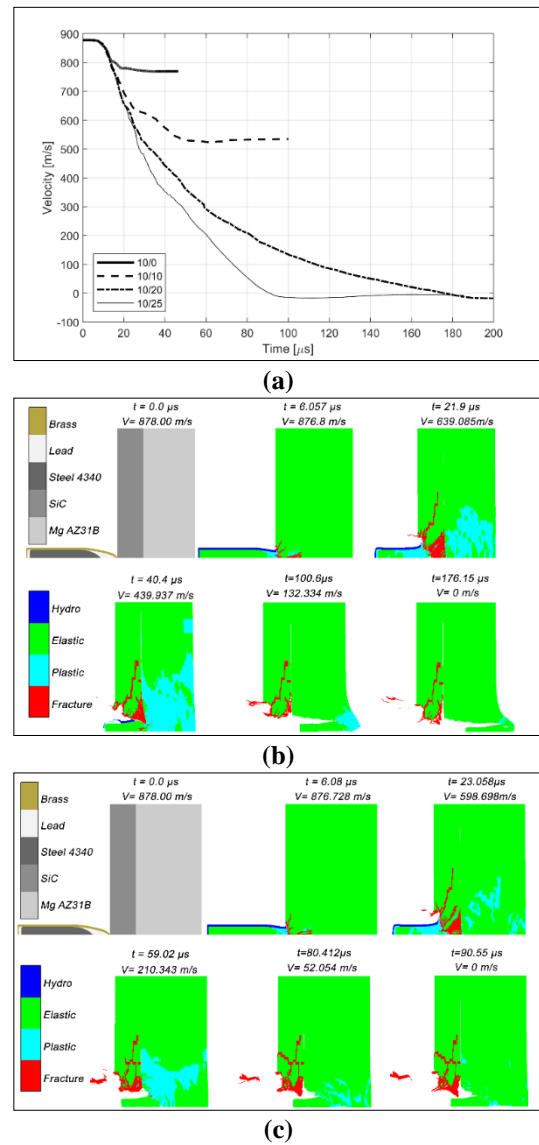
Figure 10. The velocity change of projectile as a function of time for 10 mm SiC/0-25 mm Mg AZ31B laminated composites (a), penetration process of the projectile in 10 mm SiC/20 mm Mg AZ31B (b) and 10 mm SiC/25 mm Mg AZ31B laminated composite armor (c)

In Figure 11a, the time-dependent velocity change of the ".30 APM2" projectile for the 10 mm SiC/10 mm Ti6Al4V composite armor is given. As can be seen in the graphic, the projectile was stopped by composite armor at about 88.18 μs. The projectile was eroded and deformed by the ceramic fracture conoid, which was well supported by the Ti6Al4V backing layer (Fig. 11b). Also, the mushrooming formation can be seen. Mushrooming is due to the difference between

S. Kural

projectile speed and penetration rate. Also, the mushrooming formation in the bullet can be seen. Mushrooming occurs when the projectile velocity is faster than the penetration velocity [15, 17, 19].
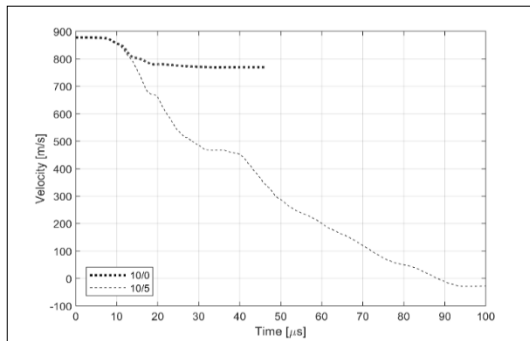
(a)
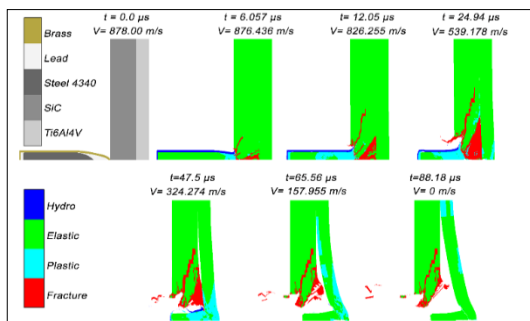
(b)

Figure 11. The velocity change of projectile as a function of time for SiC/Ti6Al4V laminated composites (a) and penetration process of the projectile in 10 mm SiC/5 mm Ti6Al4V laminated composite armor (b)
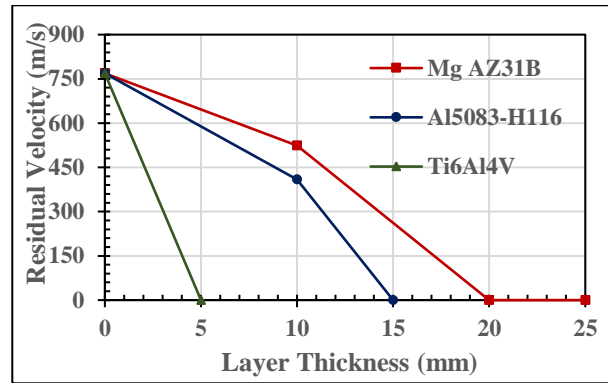
Figure 12. Residual velocity versus backing layer thickness for 10 mm SiC tiles backed with various light metal layers
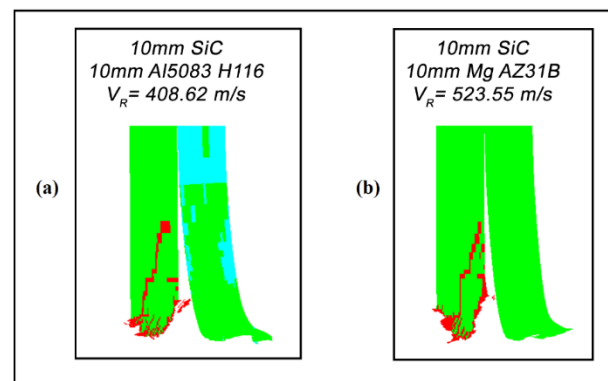
Figure 13. Perforation types of 10 mm SiC/light metal laminated composites: (a) 10 mm Al5083 H116 and (b) 10 mm Mg AZ31B

Table 3. Minimum areal densities for ballistic protection

Laminating Material and Configurations	Areal Density (kg/m²)	Ammunition / Striking Velocity (m/s)	References
6 mm Alumina/12 mm Dual Phase Steel	100	7.62 x51 AP / -	[30]
20 mm Weldox	150	7.62 APM2 / 800	[28]
40 mm Al7075-T651	108	7.62 APM2 / 950	
Al7075-T0	85	7.62 x51 AP / -	[29]
AISI 4140	100		
3x20 mm Al5083-H116	162	7.62 APM2 / 914.5	[5]
50.93 mm Al5083-H113		.30 APM2 / 853	
76.48 mm Mg AZ31B	135.2	.30 APM2 / 863	[7]
17.22 mm Steel (RHA)		.30 APM2 / 914	
10 mm SiC/5 mm Ti6Al4V	54.245		
5 mm SiC/10 mm Ti6Al4V	60.265		
10 mm SiC/15 mm Al5083-H116	72.65	.30 APM2 / 878	Present Study
10 mm Si/25 mm MgAZ31B	76.65		
5 mm SiC/30 mm Al5083-H116	97.075		
5 mm SiC 55 mm MgAZ31B	113.975		

The residual velocities of ".30 APM2" projectiles for different backing layer material and thickness are given in Figure 12. The projectile perforated the composite armor using the 10 mm Al5083-H116 backing layer at 408.62 m/s. During penetration, as a result of the projectile blunting, a dishing form was formed in the rear surface of the 10 mm Al5083-H116 layer. In the later stages of penetration, a hole was formed in the middle of this dishing and composite armor was perforated (Fig. 13a). In composite armor where a 10 mm Mg AZ31B backing layer was used, the residual velocity of the projectile was calculated as 523.55 m/s. Ductile hole growth type puncture occurred in the armor plate of Mg AZ31B (Fig 13b).

In Table 3, the areal densities of the armors providing ballistic protection are given. In this study, the lowest areal density values were obtained in laminated composites using the Ti6Al4V backing layer. Using layered SiC/Ti6Al4V armor, weight was reduced by 55-60% compared to monolithic RHA armor. By layering Mg AZ31B with a 10 mm SiC tile, a weight reduction of about 40% was achieved compared to monolithic Mg AZ31B and RHA. Al5083-H116 armor layered with 10mm SiC tile provided ballistic protection 55 % lighter than monolithic Al5083-H116 and 45% lighter than monolithic RHA

4. Conclusion

In this study, the ballistic performance of composite armors obtained by layering Al5083-H116, Mg AZ31B and Ti6Al4V light metals with 5 and 10 mm SiC tiles were investigated as analytically. The results obtained are as follows:

1.   The most important role of the ceramic layer in increasing the ballistic strength of composite armor is fracture conoid failure. This damage and its effect were excellently modeled determined with SPH.
2.   The ceramic fracture conoid should be supported by a backing layer that has a good combination of high strength and toughness to fully demonstrate the effect of ballistic strength. Therefore, the best ballistic performance exhibited SiC/Ti6Al4V composite armor.
3.   By using Al 5083-H116, Mg AZ31B and Ti6Al4V light metal alloy and SiC front layer, the similar ballistic protection was achieved with 45-60% lighter composite armors compared to the monolithic RHA armor
4.   The lowest areal density which ballistic protection was provided was calculated as 54.245 kg/m^2 in 5 mm SiC/10 mm Ti6Al4V composite armor.
5.   SiC/Al5083-H116 and SiC/Mg AZ31B layered composite armors provided the same ballistic protection approximately 50 % thinner than monolithic armors of the same metals.

6.   SiC/Al5083-H116 and SiC/Mg AZ31B layered composite armor plates provided the same ballistic protection approximately 50 % thinner than monolithic armors of the same metals.
7.   Perforation types were determined as ductile hole growth in Al5083-H116 and Mg AZ31B, and as ductile plugging in Ti6Al4V.

Author's Contributions

Saim Kural: edited the revisions, performed the analysis and result analysis
Mehmet Ayvaz: Drafted and wrote the manuscript Assisted in result interpretation and helped in manuscript preparation.

Ethics

There are no ethical issues after the publication of this manuscript.

References

1.   P.K. Jena, B. Mishra, K.S. Kumar, T.B. Bhat, An experimental study on the ballistic impact behavior of some metallic armour materials against 7.62 mm deformable projectile, *Materials & Design*. 31 (2010) 3308-3316. https://doi.org/10.1016/j.matdes.2010.02.005

2.   M.K. Forrestal, V.K. Luk, Perforation of aluminum armor plates with conical-nose projectiles. *Mechanics of Materials*. 10(1-2) (1990) 97-105. https://doi.org/10.1016/0167-6636(90)90020-G

3.   T. Borvik, A.H., Clausen, O.S., Hopperstad, Langseth, M., Perforation of AA5083-H116 aluminium plates with conical-nose steel projectiles—experimental study, *International Journal of Impact Engineering*. 30 (2004) 367-384. https://doi.org/10.1016/S0734-743X(03)00072-1

4.   T. Borvik, M.J. Forrestal, O.S. Hopperstad, T.L. Warren, Langseth, M., Perforation of 5083-H116 aluminum plates with conical-nose steel projectiles-calculations, *International Journal of Impact Engineering*. 36 (2009) 426-437. https://doi.org/10.1016/j.ijimpeng.2008.02.004

5.   T. Borvik, M.J. Forrestal, T.L. Warren, Perforation of 5083-H116 aluminum armor plates with ogive-nose rods and 7.62 mm APM2 bullets, *Experimental Mechanics*. 50 (2010) 969-978. https://doi.org/10.1007/s11340-009-9262-5

6.   M.F. Abdullah, S. Abdullah, M.Z. Omar, Z. Sajuri, M. Sohaimi, Failure observation of the AZ31B magnesium alloy and the effect of lead addition content under ballistic impact, *Advances in Mechanical Engineering*. 7(5) (2015) 1-13. https://doi.org/10.1177/1687814015585428

7.   T.L. Jones, R.D. DeLorme, M.S. Burkins, W.A. Gooch, Ballistic performance of magnesium alloy AZ31B. *23rd International symposium on ballistics*. 989-995, 16-20 April 2007, Tarragona, Spain.

8.   J.S. Montgomery, M.G.H. Wells, B. Roopchand, J.W. Ogilvy, Low-cost titanium armors for combat vehicles, *JOM*. 49(5) (1997) 45-47. https://doi.org/10.1007/BF02914684

9.   G. Sukumar, B.B. Singh, A. Bhattacharjee, K. Sivakumar, A.K. Gogia, Effect of heat treatment on mechanical properties and ballistic performance of Ti-4Al-2.3V-1.9Fe alloy, *Materials*

Today. 2 (2015) 1102-1108. https://doi.org/10.1016/j.matpr.2015.07.015

10. B.B. Singh, G. Sukumar, A. Bhattacharjee, K.S. Kumar, T.B. Bhar, A.K. Gogia, Effect of heat treatment on ballistic impact behavior of Ti–6Al–4V against 7.62 mm deformable projectile, *Materials & Design*. 36 (2012) 640-649. https://doi.org/10.1016/j.matdes.2011.11.030

11. L.S. Gallo, M.O.C.V. Boas, A.C.M. Rodrigues, F.C.L. Melo, E.D. Zanotto, Transparent glass–ceramics for ballistic protection: materials and challenges, *Journal of Materials Research and Technology*. 8(3) (2019) 3357–3372. https://doi.org/10.1016/j.jmrt.2019.05.006

12. A.L. Florence, Interaction of projectiles and composite armour, part II. Standard Research Institute, Menlo Park, California, 1969.

13. V.P. Alekseevskii, Penetration of a rod into a target at high velocity. *Combustion, Explosion and Shock Waves*. 2(2) (1966) 63-66. https://doi.org/10.1007/BF00749237

14. Tate, A., A theory for the deceleration of long rods after impact, J*ournal of the Mechanics and Physics of Solids*. 15(6) (1967) 387–399. https://doi.org/10.1016/0022-5096(67)90010-5

15. R.L. Woodward, A simple one-dimensional approach to modelling ceramic composite armour defeat, *International Journal of Impact Engineering*. 9(4) (1990) 455-474. https://doi.org/10.1016/0734-743X(90)90035-T

16. P.C. Den Reijer, Impact on ceramic faced armours. PhD thesis, Delft University of Technology, 1991.

17. R. Zaera, V. Sanchez-Galvez, Analytical modeling of normal and oblique ballistic impact on ceramic/metal lightweight armours, *International Journal of Impact Engineering*. 21(3) (1998) 133–148. https://doi.org/10.1016/S0734-743X(97)00035-3

18. I.S. Chocron Benloulo, V. Sanchez-Galvez, A new analytical model to simulate impact onto ceramic/composite armors, *International Journal of Impact Engineering*. 21(6) (1998) 461–471. https://doi.org/10.1016/S0734-743X(98)00006-2

19. S. Feli, M.E.A Aaleagha, Z. Ahmadi, A new analytical model of normal penetration of projectiles into the light-weight ceramic–metal targets, *International Journal of Impact Engineering*. 37(5) (2010) 561–567. https://doi.org/10.1016/j.ijimpeng.2009.10.006

20. E. Medvedovski, Ballistic performance of armour ceramics: Influence of design and structure. Part 2, *Ceramics International*. 36 (2010) 2117-2127. https://doi.org/10.1016/j.ceramint.2010.05.022

21. M.R.I. Islam, J.Q. Zheng, R.C. Batra, Ballistic performance of ceramic and ceramic-metal composite plates with JH1, JH2 and JHB material models, *International Journal of Impact Engineering*. 137 (2020) e103469. https://doi.org/10.1016/j.ijimpeng.2019.103469

22. G. R. Johnson, W. H. Cook, A constitutive model and data for metals subjected to large strains, high strain rates and high temperatures, Proceedings of the *7th International Symposium on Ballistics*,1983.

23. M. Übeyli, R.O. Yildirim, B. Ögel, Investigation on the ballistic behavior of Al2O3/Al2024 laminated composites, *Journal of Materials Processing Technology*. 196 (2008) 356-364. https://doi.org/10.1016/j.jmatprotec.2007.05.050

24. C.C. Holland, E.A. Gamble, F.W. Zok, V.S. Deshpande, R.M. McMeeking, Effect of design on the performance of steel-alumina bilayers and trilayers, *Mechanics of Materials*. 91(1) (2015) 241-251. https://doi.org/10.1016/j.mechmat.2015.05.002

25. B. Wang, G. Lu, On the optimisation of two-component plates against ballistic impact, J. *Journal of Materials Processing Technology*. 57 (1996) 141-145. https://doi.org/10.1016/0924-0136(95)02050-0

26. T. Demir, M. Übeyli, R.O. Yildirim, M.S. Karakas, Response of Alumina/4340 Steel Laminated Composites against the Impact of 7.62 mm Armor Piercing Projectiles, *Science and Engineering of Composite Materials*. 16(2) (2009) 89-98. https://doi.org/10.1515/SECM.2009.16.2.89

27. M.E. Backman, W. Goldsmith, The mechanics of penetration of projectiles into targets. *International Journal of Engineering Science*. 16(1) (1978) 1-99. https://doi.org/10.1016/0020-7225(78)90002-2

28. E.A., Flores-Johnson, M., Saleh, L., Edwards, Ballistic performance of multi-layered metallic plates impacted by a 7.62-mm APM2 projectile, *International Journal of Impact Engineering*. 38 (2011) 1022-1032. https://doi.org/10.1016/j.ijimpeng.2011.08.005

29. T. Demir, M. Übeyli, R.O. Yıldırım, Investigation on the ballistic impact behavior of various alloys against 7.62 mm armor piercing projectile, *Materials & Design*. 29 (2008) 2009-2016. http://doi.org/10.1016/j.matdes.2008.04.010

30. M. Übeyli, H. Deniz, T. Demir, B. Ögel, B. Gürel, Ö. Keleş, Ballistic impact performance of an armor material consisting of alumina and dual phase steel layers, *Materials & Design*. 32(3) (2011) 165-1570. https://doi.org/10.1016/j.matdes.2010.09.025

Celal Bayar University Journal of Science

Investigation of Burr Formation and Tool Wear During the Drilling of Commercial Purity Copper Material

Hüseyin Gökçe[1]*

[1]* Çankırı Karatekin University, Engineering Faculty, Mechanical Engineering; Çankırı, Turkey
* huseyingokce@karatekin.edu.tr
Orcid: 0000-0002-2113-1611

Abstract

Copper is one of the materials that are sought and requested in many sectors due to its high electrical and thermal conductivity values. Its high ductility makes it difficult to drill commercial purity copper and has a negative effect on hole quality. In this study, commercial purity copper material was subjected to drilling tests with HSS drills without using coolant. Surface roughness, deviation from diameter and deviation from cylindrical values were measured in varying drilling conditions and also modeled by regression analysis. Quantitative effects of the results were determined by analysis of variance. Also, wears occurring in the drill bits, burr formations at the entrance and exiting of the hole were examined. As a result of the regression analysis, it was observed that the feed rate on the surface roughness value, the coating status for the deviation from cylindrical and diameter had a significant effect on the results ($P<0.05$). It was observed that burrs formation in the hole entrances was insignificantly small, but the burrs formation increased at high feed rate values at the end of the holes, and decreased at high cutting speeds. It has been determined that the workpiece material tends to stick to the drill bits at increasing values of the feed rate and removal of the chips becomes difficult.

Keywords: Burr formation, copper, drilling, regression analysis, tool wear

1. Introduction

Although copper has been used in many fields due to its softness and easy workability in the past, it has found newly apply areas with its newly known properties. It is used extensively in the field of electricity and electronics, thanks to its ability to conduction the highest heat and electricity, especially after silver and gold [1-4]. Although pure copper has high electrical and thermal conductivity, its mechanical properties such as tensile stress, creep and hardness are low [3, 5]. Copper and alloys have been used as bearing materials for a long time due to their properties such as good corrosion resistance, high thermal and electrical conductivity, self-lubrication (by powder metallurgy method) and good wear resistance [6, 7].

Despite the developments in the production methods, the traditional machining methods (turning, milling, drilling etc.) are still up to date. Drilling is still a widely used method with its simple structure and low production costs [8].

Although there are many studies on forming copper materials by machining, studies on drilling are rarely found in the literature. Lin and Ting investigated tool wear with the help of signals based on cutting forces that occurred during the drilling of copper alloy material with HSS drill bits. They stated that the feed rate, depth of cut and tool wear are effective on the cutting forces, and tool wear increases with increasing feed force and moment [9]. Yang et al. they have made drilling tests with two different drill geometries on printed circuit boards. They examined cutting force, torque and chip morphology at different cutting parameters. They expressed that the cutting force increases with increasing feed rate and decreases with increasing cutting speed. They expressed that the drill geometry was significantly effective on thrust force and chip evacuation [10]. Vergara et al. copper and brass materials have been subjected to a series of experiments by friction drilling method. They examined the hole qualities in terms of sheet thickness, spindle speed, feed amount, tool geometry. They explained that high spindle speeds and low feed rates are more effective than other parameters to produce sufficient quality holes

[11]. Tang et al. compared the results with experimental studies by analyzing the drilling of electronic circuit boards with high copper content in terms of cutting force, cutting torque and tool temperature with the help of finite elements. They expressed that the results they obtained from analysis and experimental studies were quite close and consistent [12]. Moriwaki et al. in the turning process of copper material with diamond cutting tools, they studied the deformations that occurred on the cutting tool and workpiece by using experimental and finite element method. They stated that the experimental and simulation results were consistent and that the temperature effect should not be neglected in micro machining with diamond cutting tools [13]. Zhang and zhang investigated the factors affecting surface quality in turning of high conductivity copper material that has undergone various heat treatment processes. They measured the lowest surface roughness values from the samples subjected to recrystallization annealing. In addition, they explained that the homogeneity of the crystalline structure and the order of processing affected the roughness of the finished surface and residual surface stresse [14]. Breton et al. tried to explain the relationship between cutting conditions and surface integrity and related physical-chemical properties in machining. They examined the effects of pure copper material on the electrochemical behavior and corrosion resistance at the end of the super finishing by experimental and finite element method. They presented a model including thermal-mechanical, microstructure, recrystallization approaches to calculate the residual stress, temperature and burr formation areas in the processed material. They compared the experimental and simulation results and stated that the results are compatible with each other [15]. Mahajan et al. have been made a series of turning experiments with high-conductivity copper material with diamond cutting tools. They tried to determine the quantitative effect of four machining parameters on the surface roughness of copper: cutting speed, amount of feed, depth of cut and tool nose radius. From experimental studies, they stated that the tool nose radius is a very dominant parameter among other parameters considered, as well as higher cutting depth, higher cutting speed and higher feed rate can be used as the larger tool nose radius is used [16]. Tanaka et al. examined the chips formed during the turning of the copper material with the diamond cutting tools and the wear mechanisms that occur in the cutting tool exposed to thermal loads. They expressed that the micro cracks formed in the cutting tool formed rapidly by the reaction of the cutting tool material and copper [17]. Shimada et al. have simulated the cutting tool wear mechanisms, thermodynamic loads and wear process when turning copper with diamond cutting tool in oxygen atmosphere. As a result of the study, they stated that turning in the oxygen atmosphere significantly reduced cutting tool wear and increased production efficiency [18]. Rahman et al. studied milling mechanism and factors affecting the micro-end mill

cutting tool during the milling of the pure copper workpiece. In their experiments used different cutting speeds, cutting depths and feed rates, they used cutting tools with two different helix angles. They stated that the chips formed at the end of the work was very similar to the chips formed (spiral and broken) during the traditional milling. They stated that tool wear increases with machining time and has a significant effect on cutting forces [19].

Although copper is one of the materials with the highest heat conductivity coefficient, its ductile ductility makes drilling difficult. According to the literature research conducted, the deviation of the holes formed by the drilling of copper materials from the dimensional and geometric tolerances and the interaction of the burr formation with the drilling parameters and drill bit angle are rarely studied. In this study, commercial grade copper material with HSS cutting tools has been subjected to drilling tests at 4 different cutting speeds, 4 different feed rates, 4 different drill bit angles and 2 different coating conditions. The holes formed as a result of the experiment were examined in terms of surface roughness, deviation from the diameter, deviation from cylindrical and burr formation. Also, wears occurring in drill bits were investigated.

2. Materials and Methods
2.1. Material and Machining Experiments

Some properties of commercial purity copper material used in the experiments are given in Table 1. The test part prepared with Ø60 mm diameter and 15 mm thickness is connected to the table of Arion IMM-600 CNC vertical center table with a 4-jaw chuck. Average surface roughness values (Ra) were obtained using Mitutoyo SJ-410 profilometer.

Table 1. Some properties of commercial purity copper [20].

Property	Unit	Copper
Density (at 20ºC)	g/cm^3	7.764
Melting point	ºC	1083.2-
Vickers hardness	HV	50
Yield stress	MPa	33.3
Tensile stress	MPa	210
Elastic modulus	GPa	110
Poisson's ratio	-	0.343
Heat transmission	[W/(mK)]	385

Generally high precision is required for the parts used in defence and aerospace industries. Therefore, geometric and dimensional tolerances of the holes on these parts are of quite importance. Deviation from diameter is the difference between the nominal diameter and measured diameter of the drilled hole while, cylindricity is defined as the combination of parallelism, circularity and straightness of a cylinder surface. The deviation from cylindricity is the variation between measured

cylindrical surface and its ideal cylindrical surface [21]. In each measurement, the probe touched four points along the periphery. The measurements were taken 3 mm below and above the top and bottom surfaces of the workpiece, respectively. Deviation from the diameter and the cylindrical measurements has made with Hexagon Global Advantage CMM device. For observation of tool wear and burr formation, a microscope which has LED lighting, a resolution of 5 megapixels with a resolution of 2592x1944, a brightness reduction feature, and a digital 240 magnification feature were used. In Figure 1, the design of the experimental setup established is tried to be shown.
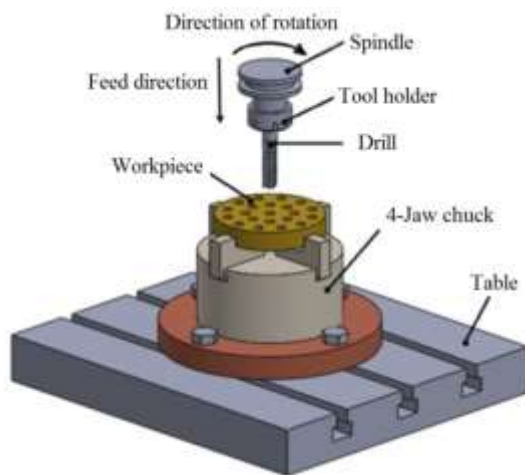
Figure 1. Experimental setup.

Drill bits (drill bit angle: 90º, 105º, 118 ° and 140º) are connected to the tool holder with a Ø5-6 mm collet. Uncoated and coated (CVD - AlTiN - coating thickness: 5 µm) HSS drill bit is shown in Figure 2.

Figure 2. HSS drill bit.

15 mm length hole drilling was applied to the test material by using different cutting conditions with HSS drill bits. The results were examined in terms of surface roughness (Ra), deviation from diameter (DD), deviation from cylindrical (CD), cutting tool wear and burr formation. Experiments are designed with the help of L16 orthogonal array, and the variables and levels used in the experiments are given in Table 2. Variables and levels for the relevant material were determined taking into account cutting tool catalogs and literature recommendations. Preliminary experiments have been carried out at the highest levels of cutting parameters recommended in the catalogs and literature. Statistical calculations such as regression analysis and ANOVA were made by Minitab 17 software.

Table 2. Variables used in the experiments and their levels

Control factors	Cutting speed (Vc)	Feed rate (f)	Drill bit angle (β)	Coating condition (CC)
Unit	m/min	mm/rev	°	-
Code	A	B	C	D
Levels	10	0.025	90	Uncoated
	20	0.050	105	
	30	0.075	118	Coated
	40	0.100	140	

2.2. Regression Analysis

Regression analysis is a model that includes dependent variables (quality characteristic) and independent variables (control factors), and it is enabled the dependent variables to be expressed with independent variables [22]. The coefficient of determination (R^2) obtained as a result of the equation gives the rate of expression of independent variables with dependent variables. The closer the R^2 value to 1, the more accurate results will can be obtained from the regression model.

Regression analysis is a well-known and widely used statistical tool by scientists. Karaca examined the effect of drilling parameters such as cutting speed, feed rate and drill bit angle on the deformation factor formed in the drilling process in glass fiber reinforced plastic composites. It has tried to determine the most appropriate drilling parameters using multiple regression analysis [23]. In the drilling process of fiber-reinforced polymer matrix composite materials, Bayraktar and Turgut investigated the surface damage at the entry and exit of the hole, taking into account factors such as cutting tool, cutting parameters and cutting tool geometry. The data they obtained were tried to be interpreted using methods such as Taguchi, variance analysis, artificial neural networks and regression analysis. They has emphasized that high cutting speed and low feed rates should be used as a result of the studies [24]. Meral et al., have modeled the progression forces and surface roughnesses obtained in the drilling

of AISI 1050 material depending on experimental parameters, (such as drill geometry drill diameter, feed amount and cutting speed) with linear regression, quadratic regression and exponential regression methods [25].

3. Results and Discussion

It used 4 different cutting speeds, 4 different feed rates, 4 different drill bit angles and 2 different coating conditions were used in the hole drilling experiments performed on commercially pure copper material. Experimental results are interpreted in terms of average surface roughness, deviation from diameter and deviation from cylindrical values (Table 3).

It obtained as a result of drilling the commercial purity copper material with the determined control factors is the average of the surface roughness 3.202 μm, the average of deviation from the diameter is 0.033 mm and the average of deviation from the cylindrical value is 0.039 mm. When Table 3 is examined, it is seen that the highest values of the variables are 4.178 μm for surface roughness, 0.053 mm for diameter deviation value, 0.060 mm for deviation from cylindrical value. Also, the lowest values are 2.490 μm for surface roughness, 0.015 mm for deviation from the diameter and 0.020 mm for deviation from the cylindrical value. These values are within acceptable limits for rough surface

holes at N9-N10 surface tolerances. These differences between the results are an indication that the variables used in the drilling experiments have a significant effect on the drilling performance. The measured average surface roughness is relatively high. The reason for this is that copper used as test material is thought to be of high purity and parallel to its ductility.

When the obtained results are examined in terms of cutting parameters (cutting speed and feed rate); the highest values for surface roughness, deviation from diameter and deviation from cylindrical are measured at a cutting speed of 40 m/min at a feed rate of 0.100 mm/rev. The lowest measurements were obtained at 0.025 mm/rev feed rate at 10 m/min cutting speed for surface roughness value, and at 0.025 mm/rev feed rate at 20 m/min cutting speed at the lowest deviation from diameter and cylindrical values. According to these results, it can be said that surface roughness, deviation from diameter and cylindrical values are affected by the change in cutting parameters. High surface roughness values are frequently observed especially at low cutting speeds in the processing of commercial purity materials such as aluminum, copper and nickel [26-29]. In almost all machining processes, it is expected that surface roughness values will decrease especially with increasing cutting speed [27-32].

Table 3. Ra, DD and CD which measured in experiments

Test no	Code	Vc (m/min)	Code	f (mm/rev)	Code	β (°)	Code	Coating condition	Ra (μm)	DD (mm)	CD (mm)
1	A1	10	B1	0.025	C1	90	D1	Uncoated	2.490[*]	0.035	0.041
2	A1	10	B2	0.050	C2	105	D1	Uncoated	2.959	0.051	0.058
3	A1	10	B3	0.075	C3	118	D2	Coated	3.103	0.018	0.023
4	A1	10	B4	0.100	C4	140	D2	Coated	3.436	0.027	0.032
5	A2	20	B1	0.025	C2	105	D2	Coated	2.714	0.015[*]	0.020[*]
6	A2	20	B2	0.050	C1	90	D2	Coated	2.513	0.023	0.028
7	A2	20	B3	0.075	C4	140	D1	Uncoated	4.099	0.042	0.048
8	A2	20	B4	0.100	C3	118	D1	Uncoated	3.978	0.051	0.057
9	A3	30	B1	0.025	C3	118	D1	Uncoated	2.582	0.019	0.025
10	A3	30	B2	0.050	C4	140	D1	Uncoated	2.784	0.024	0.030
11	A3	30	B3	0.075	C1	90	D2	Coated	3.394	0.035	0.041
12	A3	30	B4	0.100	C2	105	D2	Coated	3.728	0.049	0.056
13	A4	40	B1	0.025	C4	140	D2	Coated	2.637	0.019	0.024
14	A4	40	B2	0.050	C3	118	D2	Coated	3.031	0.026	0.031
15	A4	40	B3	0.075	C2	105	D1	Uncoated	3.603	0.037	0.043
16	A4	40	B4	0.100	C1	90	D1	Uncoated	4.178[**]	0.053[**]	0.060[**]
								Avarage	3.202	0.033	0.039

* minimal value, ** maximum value

3.1 Regression Analysis and Interaction of Control Factors

The regression equations required to calculate the variable values, (Ra, DD and CD) are given in Equation 3.1, Equation 3.2 and Equation 3.3, respectively. In

equality; A is cutting speed, B is feed rate, C is drill bit angle and D is coating condition (Table 2 and Table 3).
It is desirable that the variables subject to experiments are at the lowest possible levels in drilling experiments. Therefore, while the increasing values of the variables in the negative factor state in the regression equations

obtained will have positive results, the decreasing values will have a negative effect.

$$Ra=2.22+0.0892A+0.440B+0.0207C-0.264D \quad (3.1)$$
$$DD=0.0424+0.00020A+0.00699B-0.00353C-0.0125D \quad (3.2)$$
$$CD=0.0488+0.00021A+0.00734B-0.00370C-0.0132D \quad (3.3)$$

Table 4 gives the table of coefficients found after obtaining the regression equation. In this table; Coef: coefficients of values, SE Coef: standard error in coefficients, T: the result of test statistics, and P: whether regression analysis is significant indicates. The P values less than 0.05 is a proof that the control factor is statistically significant.

According to the regression equation (Equation 3.1) obtained for the average surface roughness, the highest coefficient belongs to the feed rate, followed by the coating condition, cutting speed and drill bit angle, respectively. When the P values in Table 4 are examined, it can be seen that the feed rate on the surface roughness is statistically significant. According to the regression equation (Equation 3.2) obtained for

deviation from diameter, the highest coefficient belongs to the coating condition, followed by the feed rate, drill bit angle and cutting speed, respectively. When the P values in Table 4 are analyzed, it is seen that the feed rate and the coating condition on the deviation from diameter is statistically significant. According to the regression equation (Equation 3.3) obtained for deviation from cylindrical, the highest coefficient belongs to the coating state, followed by the feed rate, the drill bit angle and the cutting speed, respectively. When the P values in Table 4 are analyzed, it is seen that the feed rate and the coating condition are statistically significant on the deviation from cylindrical. When the determination coefficients (R^2) in Table 4 are examined, the test results of the regression equations obtained; we can explain it as 85.0% for surface roughness and 71.9% for deviation from diameter and cylindrical. In other words, a relative relationship can be mentioned between the variables.
Variance analyses of the multiple linear regression equation that we obtained in Table 5 are given. According to this table, P values are less than 0.05 and therefore we can say that we have statistically significant regression equations.

Table 4. Coefficients table of regression equations

	Term	Constant	Cutting speed	Feed rate	Drill bit angle	Coating condition	R-Sq (R^2)	R-Sq (adj) (R^2 adj)
Ra	Coef	2.2234	0.08922	0.44005	0.02074	-0.2645	85.0%	79.5%
	SE Coef	0.3292	0.05890	0.05890	0.05890	0.1317		
	T	6.75	1.51	7.47	0.35	-2.01		
	P	0.000	0.158	0.000	0.731	0.070		
DD	Coef	0.04236	0.000204	0.006987	-0.003527	-0.012547	71.9%	61.7%
	SE Coef	0.01015	0.001815	0.001815	0.001815	0.004059		
	T	4.17	0.11	3.85	-1.94	-3.09		
	P	0.002	0.912	0.003	0.078	0.010		
CD	Coef	0.4882	0.000215	0.007336	-0.003703	-0.013175	71.9%	61.7%
	SE Coef	0.01065	0.001906	0.001906	0.001906	0.004262		
	T	4.58	0.11	3.85	-1.94	-3.09		
	P	0.001	0.912	0.003	0.078	0.010		

Table 5. Variance analysis of regression equations

	Source	DF	SS	MS	F ratio	P value
Ra	Regression	4	6.2187	1.5547	19.71	0.000
	Error	11	0.8676	0.0789		
	Total	15	7.0863			
DD	Regression	4	0.00224534	0.00056134	7.04	0.005
	Error	11	0.00087714	0.00007974		
	Total	15	0.00312248			
CD	Regression	4	0.00170900	0.00042725	19.35	0.000
	Error	11	0.00024294	0.00002209		
	Total	15	0.00195194			

3.2 Tool Wear and Deviation from Tolerances

When Figure 3 is examined, it is seen that the surface roughness values measured as a result of drilling of commercial grade copper material are affected by the changes in the feed rate. The increase in the feed rate has a negative effect on the surface roughness. The increase in cutting speed does not affect the surface roughness much. In addition, when the drill bits pictures in Figure 4 are examined, it is seen that the workpiece material tends to stick on the cutting tool, especially at low cutting speed and high feed rates. It is thought that the high surface roughness is due to the effect of adhesion on the cutting tool.
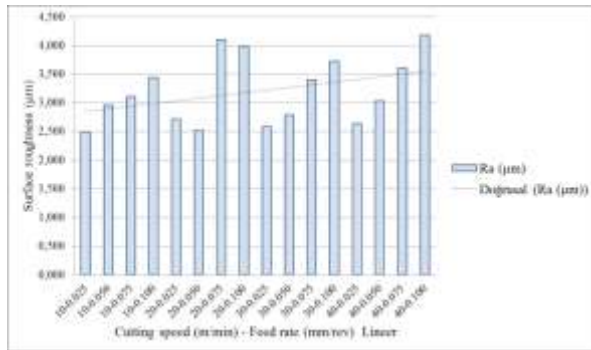
Figure 3. Average surface roughness values

10 m/min, 0.025 mm/rev
90°, uncoated

10 m/min, 0.050 mm/rev
105°, uncoated

10 m/min, 0.075 mm/rev
118°, coated

10 m/min, 0.100 mm/rev
140°, coated

20 m/min, 0.025 mm/rev
105°, coated

20 m/min, 0.050 mm/rev
90°, coated

20 m/min, 0.075 mm/rev
140°, uncoated

20 m/min, 0.100 mm/rev
118°, uncoated

30 m/min, 0.025 mm/rev
118°, uncoated

30 m/min, 0.050 mm/rev
140°, uncoated

30 m/min, 0.075 mm/rev
90°, coated

30 m/min, 0.100 mm/rev
105°, coated

40 m/min, 0.025 mm/rev
140°, coated

40 m/min, 0.050 mm/rev
118°, coated

40 m/min, 0.075 mm/rev
105°, uncoated

40 m/min, 0.100 mm/rev
90°, uncoated

Figure 4. Used drill bit in experiments

According to the regression analysis, it was stated that the surface roughness value was most affected by the coating condition. In Figure 4, it is seen that in uncoated cutting tools, adhesion is more effective than coated tools. Almost all uncoated cutting tools have adhesion marks on the chisel edge.

When looking at the graphs in Figure 5, it can be said that changes in cutting speed and feed rates have a similar effect on deviation from diameter and deviation from cylindrical. In particular, deviation values were significantly affected due to the increase in the amount of progress, and deviation amounts increased. It can be said that work pieces sticking to chisel edge are effective on deviation values from diameter and cylindrical.

3.3 Burr Formation

Residual workpiece materials (burrs) remaining on the machined material after machining significantly affect workpiece quality and machining efficiency. These burrs should be removed with a second process and this process will be a negative effect increasing costs. For this reason, burr formation should be either prevented completely or kept as low as possible. In Figure 6, images of the entrance and exiting parts of the holes formed as a result of the experiment are given. It is seen that the burrs formed in the entrance part of the holes are quite less than the burrs formed in the exiting part.

Figure 5. Deviation values from diameter and cylindrical

Figure 6. Top and bottom views of holes (entrance and exiting of the holes)

When Figure 6 is examined, it is seen that the burrs formed at the entrance are affected by the changes in cutting speed and feed rate. Despite the increased cutting speeds, the entrance parts of the holes are smoother with low feed rate. Also, a clear circularity is observed in the holes obtained with coated drill bits at 30 and 40 m/min cutting speeds.

Very high burr formation is observed at the exiting parts of the drilled holes. This is thought to be due to the high elasticity value of copper. It is seen that the burring formed in the exiting part decreases relatively with increasing cutting speed and decreasing the feed rate. In addition, it is observed that burr formation decreases in coated drill bits compared to uncoated drill bits. The reason for this can be explained by the fact that the coating has a significant effect on the cutting tool, making the chip more comfortable and easily removing the chip. In Figure 6, top is entrance of the holes and bottom is exiting of the holes.

4. Conclusion

In this study, the surface roughness, deviation from diameter and deviation from cylindrical obtained by drilling commercial purity copper material with HSS cutting tools using 4 different variables (cutting speed, feed rate, drill bit angle and coating condition) were investigated. Also, tool wear and burr formation occurring as results of the experiment were evaluated according to variable drilling parameters. As results of the study, the following results were obtained.

- As a result of the regression analysis, it was observed that the feed rate was effective on the surface roughness and the deviation from the cylindrical, and also the coating condition was significantly influenced on the results for the deviation from the diameter.

- It has been observed that the surface quality increases with increasing cutting speeds and low feed rates.

- It has been found that the holes obtained with coated drill bits have lower surface roughness values and deviations of the geometric have lower values.

- The burr formations at the entrance of the holes are very small, but coated drill bits at higher machining speeds gave better results.

- It was observed that burr formation, increased at high feed rate values at the exiting of the holes and decreased at high cutting speeds.

- Intense burr formation was observed at the exiting of the holes and in cases where the burr thickness was high (at high feed values), the quality of the hole was negatively affected.

- In almost all experiments, the adhesion of the workpiece material to the drill bit chisel angle has been observed. Increasing the cutting speed has decreased the sticking significantly.

- In the increasing values of the feed rate, the adhesion of the workpiece material on the drill bit has increased, and it has adversely affected the workpiece quality.

Author Contributions

Hüseyin GÖKÇE: Drafted and wrote the manuscript, performed the experiment and result analysis.

Ethics

There are no ethical issues after the publication of this manuscript.

References

1. Yazan, HA, Akar, AU, Özmerih, L. In: Bakır ve bakır ürünleri kullanım alanları. MTA Enstitüsü Yayınları, Ankara, pp 43-47.

2. Xiong, X, Sheng, HC, Chen, J, Yao, PP. 2007. Effects of sintering pressure and temperature on microstructure andtribological characteristic of Cu-based aircraft brake material. *Trans. Nonferrous Met. Soc. of China*; 17: 669-675.

3. Ulutaş, A, Turhan, H, Çinici, H. 2016. Toz metalurjisi yöntemi ile üretilen ferrobor takviyeli bakır kompozitinin mekanik özelliklerinin belirlenmesi. *BAUN Fen Bil. Enst. Dergisi*; 18(1): 10-20.

4. Tylecote, RF. In: Kupfer in natur, technik, kunst und wirtschaft. Norddeutsche Affinerie Private Sendung, Hamburg, 1966, pp 28.

5. Tjong, SC, Lau, KC. 2000. Tribological behaviour of SiC particle-reinforced copper matrix composites. *Materials Letters*; 43: 274-280.

6. Schmidt, RF, Schmidt, DG. In: Selection and Application of Copper Alloy Castings, ASM Handbook II. 1993, pp 346-355.

7. Ünlü, BS, Köksal, NS, Atik E. 2003. Bakır esaslı bronz ve pirinç yatakların tribolojik özelliklerinin karşılaştırılması. *DEÜ Mühendislik Fakültesi Fen ve Mühendislik Dergisi*; 5(2): 103-108.

8. Kurt, M, Kaynak, Y, Bakır, B, Köklü, U, Atakök, G, Kutlu, L. In: Experimental investigation and Taguchi optimization for the effect of cutting parameters on the drilling of Al 2024-t4 alloy with diamond like carbon (DLC) coated drills, 5. Uluslararası İleri Teknolojiler Sempozyumu (IATS'09), Karabük, 2009.

9. Lin, SC, Ting, CJ. 1995. Tool wear monitoring in drilling using force signals. *Wear*; 180(1-2): 53-60.

10. Yang, LP, Huang, LX, Wang, CY, Zheng, LJ, Ma, P, Song, YX. 2011. Drilling force and chip morphology in drilling of PCB supported hole. *Advanced Materials Research*; 188:429-434.

11. Vergara, J, Damm, S, Villanueva, J, Godoy, JM, Tikal, F. 2001. Bush making by thermal flow drilling in copper and brass. *The International Journal for Manufacturing Science & Production*; 4(2): 103-111.

12. Tang, HQ, Wen, J, Wang, CY, Wu, LS, Song, YX. 2011. Simulation of drilling on the copper of PCB with Ultra-high-speed. *Advanced Materials Research*; 188: 739-742.

13. Moriwaki, T, Akira, H, Okuda, K. 1990. Effect of cutting heat on machining accuracy in ultra-precision diamond turning. *CIRP Annals*; 39(1): 81-84.

14. Zhang, H, Zhang, X. 1994. Factors affecting surface quality in diamond turning of oxygen-free high-conductance copper. *Applied Optics*; 33(10): 2039-2042.

15. Breton, SB, Gravier, J, Vignal, V. 2011. Impact of superfinish Tturning on surface integrity of pure copper. *Procedia Engineering*; 19: 28-33.

16. Mahajan, KA, Sasalah, M, Gawande, SH. 2010. Experimental investigations of surface roughness on OFHC copper by diamond turning machine. *International Journal of Engineering Science and Technology*; 2(10): 5215-5220.

17. Tanaka, H, Shimada, S, Higuchi, M, Yamaguchi, T, Kaneeda, T, Obata, K. 2005. Mechanism of cutting edge chipping and its suppression in diamond turning of copper. *CIRP Annals*; 54(1): 51-54.

18. Shimada, S, Inamura, T, Higuchi, M, Tanaka, H, Ikawa, N. 2000. Suppression of tool wear in diamond turning of copper under reduced oxygen atmosphere. *CIRP Annals*; 49(1): 21-24.

19. Rahman, M, Kumar, AS, Prakash, JRS. 2001. Micro milling of pure copper. *Journal of Materials Processing Technology*; 116(1): 39-43.

20. Matweb. (accessed at;15.05.2020) http://www.matweb.com/search/DataSheet.aspx?MatGUID=9aeb e83845c04c1db5126fada6f76f7e/

21. Gökçe, H, Yavuz, M, Çiftçi, İ. 2020. An investigation into the performance of hss drills when drilling commercially pure molybdenum. *Sigma J Eng & Nat Sci*; 38(1): 61-70.

22. Başar, G, Kahraman, F. Delik işleme prosesinde kesme parametrelerinin Taguchi metodu ve regresyon analizi kullanılarak modellenmesi ve optimizasyonu. In: 2nd International Mediterranean Science and Engineering Congress (IMSEC 2017), 2017, pp 688-695.

23. Karaca, F. 2016. Cam elyaf takviyeli plastik kompozitlerde delme parametrelerinin deformasyon faktörüne etkisinin araştırılması. *Science and Eng. J of Fırat Univ*; 28(2): 23-27.

24. Bayraktar, Ş, Turgut, Y. Elyaf takviyeli polimer kompozit malzemelerin delinmesi üzerine bir araştırma, In: 3. Ulusal Talaşlı İmalat Sempozyumu, Ankara, 2012.

25. Meral, G, Dilipak, H, Sarıkaya, M. 2011. AISI 1050 malzemenin delinmesinde ilerleme kuvvetleri ve yüzey pürüzlülüğünün regresyon analiziyle modellenmesi. *TÜBAV Bilim Dergisi*; 4(1): 31-41.

26. Kimmelmann, M, Duntschew, J, Schluchter, I, Möhring, HC. 2019. Analysis of burr formation mechanisms when drilling CFRP-aluminium stacks using acoustic emission. *Procedia Manufacturing*; 40: 64-69.

27. Dheeraj, N, Sanjay, S, Bhargav, KK, Jagadesh, T. Investigation into solid lubricant filled textured tools on hole geometry and surface integrity during drilling of aluminium alloy, In: Materials Today: Proceedings, 10th International Conference of Materials Processing and Characterization, 2020.

28. Korkmaz, ME, Çakıroğlu, R, Yaşar, N, Özmen, R, Günay, M. 2019. Al2014 Alüminyum alaşımının delinmesinde itme kuvvetinin sonlu elemanlar yöntemi ile analizi. *El-Cezerî Journal of Science and Engineering*; 6(1): 193-199.

29. Çiftçi, İ, Gökçe, H. 2019. Ti6Al4V Titanyum alaşımının delinmesinde delme yönteminin aşınmaya etkisinin incelenmesi. *Journal of Polytechnic*; 22(3): 627-631.

30. Şahin, İ. 2013. Alüminyum matrisli kompozit malzemelerin matkap ile delinmesi konusunda yapılan çalışmaların incelenmesi. *Mühendis ve Makina*; 55(649): 9-16.

31. Elitaş, M, Çiftçi, İ. 2017. Sertleştirilmiş AISI 52100 malzemenin aşındırıcı diskle kesilmesinin araştırılması. *TÜBAV Bilim Dergisi*; 10(2): 1-10.

32. Yavuz, M, Gökçe, H, Çiftçi, İ, Gökçe, H, Yavaş, Ç, Şeker, U. 2020. Investigation of the effects of drill geometry on drilling performance and hole quality. *The International Journal of Advanced Manufacturing Technology*; 106(9): 4623-4633.

Noise Exposure Estimation of Surface-Mine- Heavy Equipment Operators Using Artificial Neural Networks

Ayla Tekin[1*] iD

[1] Department of Machinery and Metal Technology, Soma Vocational School, Manisa Celal Bayar University, Manisa 45500, Turkey
*ayla.tekin@cbu.edu.tr
*Orcid: 0000-0002-2547-0872

Abstract

Ever inreasing demand to raw mineral production stimulates intense use of mining machinery and subsequently exposes mining machinery operators to high levels of continuous noise. Long-term exposure to high levels of continuous noise can cause Occupational Hearing Loss (OHL) on operators. In order to certify a good working environment, it is important to estimate real noise levels of opencast mining machines.

The aim of this study was to assess exposure levels to continuous noise using the test records of continouos noise emitted from mining machinery and recommend some actions to reduce it. Artificial neural networks (ANN) tool developed by MATLAB software has been used for these estimates.

During the study, consistent personal noise exposure levels emitting from 60 different opencast mining machinery was recorded. The lowest, highest, average and equivalent noise levels of the machines were recorded and possible exposure noise-levels ($L_{EX,8H}$) on operators were calculated.

Later, data obtained from tests were used to train the ANN multilayered model by forward-feed-fault-back circulation algorithm. During modeling of ANN; vehicle types, recording times, ambient temperature and pressure and relative humudity were determined as input parameters. By the help of the model, equivalent and momentary noise levels prior to maximum level were estimated. Following training and testing of the model, the obtained noise levels were examined by statistical analysis commonly used in ANN models. It was noticed that the designed model provided very close results to the actual test results and can be applied successfully.

Keywords: Noise exposure levels, mining industry, opencast mine vehicle operators, artificial neural networks, opencast mining

1.Introduction

Today, the rapidly developing technology brings serious changes in the mining sector as it is in every industrial field. In the opencast mining sector, excessive noise pollution is inevitable due to the use of heavy machinery. Numerous researches and studies have been carried out in the past regarding the noise levels of underground and surface mine machines [1-3], and reported that mine operators may experience hearing loss if they are constantly exposed to high levels of noise [4-8].

The noise-induced hearing loss is one of the most common occupational diseases in both developing and developed countries [9]. Joy and Middendorf [10] reported the coal mines patterns and trends in noise exposure in data collected by the Mine Safety and Health Administration (MSHA) inspectors in the United States from 1987 to 2004. The MSHA issued a new regulation about occupational noise exposure which is altered the regulatory requirements and enforcement policies during this time. The data were examined to identify the potential impacts of these changes. After the announcement of the new noise rule, this reduction in each group speeded-up dramatically. For instance, the overall annual noise median considering for surface coal mining dose declined 67 percent at the same time underground coal mining declined 24 percent too. It's proved that it has been hard to controlling noise exposure, accordingly noise-induced hearing loss (NIHL) still remains one of the leading risks in the mining industry [11]. Edwards et al. [12] presented a study in which he evaluated noise exposure levels in South African mining industries. In their study, the main issue addressed in

the large-scale mining sector (underground gold, underground platinum, underground coal, and opencast coal mines) and small- to medium-scale sector mines (large underground diamond mines, small and large opencast diamond, ready-mix concrete, sand, and aggregate), of course, has been noise exposure. It was seen that on average, initial year 66.7 percent of the employees sampled, and following year 78.4 percent were exposed to noise levels of above the 85 dBA legislated occupational exposure level. Cinar and Sensogut measured the noise levels of various machines in four different mining sites in Turkey [13]. They rated the degree of discomfort of the employees from 0 to 5 according to depending on the severity of the noise they were exposed, and evaluated whether or not ear protection would be necessary. They also stated that machines should be maintained properly and personal protectors should be used.

Since the estimation of noise levels of the machine operators was influenced by many parameters and the large number of data to be used and the long time spent during works, led the researchers to develop different methods. Operators using heavy machinery in mines may be exposed to high levels of noise in working environment. İt has been an important issue for many researchers to predict noise levels accurately by analyzing the measurement data using appropriate models in order to protect the health of its employees and to ensure occupational safety. Artificial neural networks are one of the methods used for this purpose. ANN techniques are effective in complex and nonlinear models. On the other hand, ANN is preferred because of its speed, simplicity and success in learning from examples and not needing much data compared to traditional methods. Today in many areas of mining engineering, such as blasting wave propagation velocity, soil type estimation, [14-16], noise measurements estimation [17-18], long-term mining [19], methane ventilation estimation, soil collapse estimation [20], slope stability [21] the estimation of fuel consumption [22], to predict vibrational health risk[23] ANN has been successfully implemented by many researchers, designers, etc.. One of the undesirable effects caused by blasting operations in open-pit mines is the serious weakening of residential structures and livingquality in the surrounding area. To control and mitigate this situation, in the study used artificial neural networks to estimate the air blast overpressure (AOp) applied in the open-pit coal mine[24]. Blasting is one of the cheapest and most effective methods of breaking rock mass in open pit mines. However, side effects such as ground vibration (PPV), excessive air pressure, fly rock, fracture, dust and toxic are not trivial. Nguyen et al. [25] applied in their study, a series of artificial neural network models to predict PPV caused by the explosion in an open pit coal mine in Vietnam.

At present, widespread capacity of labor force and very large areas opened for mining boomed the use of excavating machinery in Turkey. In this study, noise readings of hauling and excavating machine of three opencast lignite mines at the western region of Turkey were assessed and the necessary measures suggested to ease the effect of continuous machine-noise on operators have been highlighted. In line with the study, heavy mining machinery regularly in operation within normal working hours was determined and, personal noise exposure measurements of 60 machine operators were recorded regularly in accordance with international standards. Then the equivalent noise levels of all machines were calculated. Furthermore, the noise exposure levels ($L_{EX,8H}$) of the operators using the machines were determined and the results were evaluated according to the noise regulation of the Ministry of Labor and Social Security. The results obtained during the study were presented and critical values for further works to reduce the noise exposures of machine operators down to below the legal exposure limits were recommended.

Then, the noise exposures levels of heavy machinery operators in open pit mines were trained through artificial neural networks using forward-feed-fault-back circulation algorithm, and the network that best predicts experimental results was formed. The results obtained from ANN were compared with the real-time recorded noise data showed that the model has a high sensitivity and the model can perform real time recalculations with high precision.

2. Noise Control Methodology
2.1.   Regulations

Several rules have been introduced in many countries as acts, regulations, standards and directives regarding control of occupational noise effects. The common purpose of rules under different names is to limit the impact of noise and protect environment and the people living in from the negative effects of it. Turkish Standards Institute published TS 2607 ISO 1999 (2005) standart for determination of occupational noise exposure caused by machinery and equipment and estimation of noise-induced hearing impairment in order to be assessed whether employees' noise levels are within the legal limits. These are daily and weekly noise impact levels. The daily noise impact level (LEX, 8h) is defined as the time-weighted average of all noise impact levels, including instantaneous pulsed noise, during an eight-hour working day. The weekly noise impact is the time-weighted average of five over eight hours of daily, noise-affected levels measured during a week. The minimum exposure action values in this

regulation are 80 dBA and 135 dBC; the highest exposure action values are 85 dBA and 137 dBC while the exposure limit values are 87 dBA and 140 dBC, correspondingly. In addition, determination of daily and weekly noise impact levels, measuring principles and evaluating the noise experienced in the working environment are given in TS EN ISO 9612 (2009) titled as "Determination of Acoustic-Professional Noise Exposure-Engineering Method".

2.2. Noise Measurements

In the mining sector, there are many noise sources which cover all the stages of mining work. The noise that occurs in each of these stages is different. The noise exposure measurements in this study are performed in accordance with TS EN ISO 9612-2009 "Determination of Acoustic-Occupational Noise Exposure-Engineering Method" and TS 2607 ISO 1999 "Acoustic - Determination of Exposed Noise at Work and Estimation of Hearing Loss Caused by this Noise" standards. Noise measurements were obtained from three separate coalmine site operating in the western part of Turkey.The measurements were taken in the following workplaces of machineries namely: earthmoving truck, hydraulic excavator, crawler dozer, grader and hydraulic hammer-drill (Table 2.1).

Personal exposure measurements were made on a nominal day, including operator periods and break times. Before the measurements were started, the information about the duration of the work, sources of exposure, process steps affecting the work, exposure time, work station status, number of employees and rest periods were recorded. Operators work on average 8 hours per day, 5 days per week and 210 days per year on average.

The measurements were carried out using a high precision noise level meter suitable for all noise measurements mentioned in the "Regulation on Assessment and Management of Environmental Noise" of the Ministry of Environment and Urbanization (SVANTEK). The noise meter measures the results of SPL, Leq, SEL, Ln (L1-L99) and so on. When operators are assumed to carry out their work for one full shift, the equivalent noise level of 8 hours according to TS EN ISO 9612 (2009) is determined as $L_{EX,\ 8h}$, Equation (2.1 and 2.2). Assuming that operators continue their work in one full shift, equivalent noise level for 8 hours exposure period is determined by $L_{EX,8h}$ corresponding to TS EN ISO 9612 (2009) standart.

Table 2.1 Machines and their specifications working at opencast mining sites.

Machine Types	Machine Models	Average Power	Capacity	Numbers of Machines	Field of Usage
Truck	KOMATSU 630 ES	1600 HP	170 ton	2	Earthmoving Truck used in ore or overburden transport
	KOMATSU HD 785	875 HP	85 ton	5	
	KOMATSU HD 465	702 HP	50 ton	15	
Electric Excavator	MARION 191M	1250kW	17yd^3	6	Excavator and loader used in ore or overburden excavation and loading
Hydraulic Excavator	KOMATSU PC1100	623 HP	6,5 yd^3	5	
	HITACHI EX 1200	655 HP	5m^3	1	
Loader	CAT 992	690HP	12,5 yd^3	5	
Dozer	KOMATSU D155	320HP	-	3	Crawler dozer and paydozer powerful tracked machines that is used for ground leveling, to move material and short distance excavation or support operations in open-pit mining) use a variety of front mounted blades. Large dozers often do pioneering work, such as moving dirt in preparation
	KOMATSU D275	446HP	-	5	
	KOMATSU D355	410HP	-	2	
Paydozer	KOMATSU WD600	448HP	-	1	
Grader	KOMATSU GD 705R	180HP		2	Grader is a construction machine with a long blade used to prepare the base course to create a wide flat surface upon which to place the road surface.
	KOMATSU GD 825A	280HP	-	3	
Hydraulic breaker and drill	ING. RAND	455HP	9,5inch	3	Hydraulic breakers and drills are used in blasting hole drilling operations in open mining operations
	REEDRILL	400HP	9,9inch	2	

Conceptual constant sound level (dB) containing the same amount of energy for the same duration as the acoustic energy of the A-weighted wavy sound measured over a specified period of time

$$L_{Aeq} = 10log \left[\left(\frac{1}{n} \sum_{i=1}^{n} 10^{L_i/10} \right) \right] \quad \textbf{(2.1)}$$

$$L_{Ex,8h} = L_{Aeq} + 10log \left[\frac{T_e}{T_o} \right] \quad \textbf{(2.2)}$$

Where:

L_{Aeq} : A-weighted equivalent continuous sound level (dB), equivalent to the total sound energy measured over a stated period of time and is also known as the time-average sound level

$L_{EX,8h}$: the time-average, A-weighted noise level for a nominal 8-hour working day, also known as $L_{EP,d}$ (dB)

T_e: Total continuous sound exposure time for the working day (7½ hours)
T_o: Maximum continuous sound exposure duration (8 hours)
n : Number of measurements
L_i : Sound measurement values (dBA)

Table 2.2 shows the LAeq, LEX, 8H values measured according to equations 1.1 and 1.2 in the operator cabin of 2018 for a total of 60 work machines operating in three separate opencast mine operations. Figure 2.1 shows the range and average noise level of the noise measurements made for construction machinery. In approximately 27% of these measurements, values equal to or greater than the 87 dBA exposure limit value specified in Noise Regulation were determined. The average noise levels for these groups ranged from 81.24 to 91.08 dBA. The lowest noise level was measured during the operation of the excavator operator at 74.5 dBA and the maximum noise level at the operation of the dozer operator at 98 dBA. In Figure 2.1, it can be seen that the noise exposure of the dozer machine operator which is one of the five different machines, is above the exposure limit value of 87dB (A), and the noise explosure level of two machines (grader and hydraulic hammer) operators are 85dB (A) which is the highest exposure action value. Mining is a characteristic constantly changing process. Factors such as driver's influence, uneven and rough terrain, intensity of work, exposure time, vehicle tire pressure affect the noise levels. In addition, noise exposures vary according to the types of machines used. Operation of the machine with diesel or electricity changes the noise values considerably.

Table 2.2 Noise levels of all measuring machines (dBA).

Work machine	Number	L_{Aeq} (Average)	L_{Aeq} (min)	L_{Aeq} (max)	L_{EX-8h} (Average)	L_{EX-8h} (min)	L_{EX-8h} (max)
Truck	22	84,75	77,8	**94,9**	84,46	77,52	**94,62**
Excavator	17	81,24	74,5	**90,6**	80,96	74,22	**90,32**
Grader	5	86,56	82,2	**95**	86,28	81,92	**94,72**
Dozer	11	**91,08**	82,4	**98**	**90,8**	82,12	**97,72**
Drill	5	85,46	81,5	**89,9**	85,18	81,22	**89,62**

Indicated in bold are noise levels above the 87 dB(A) limit
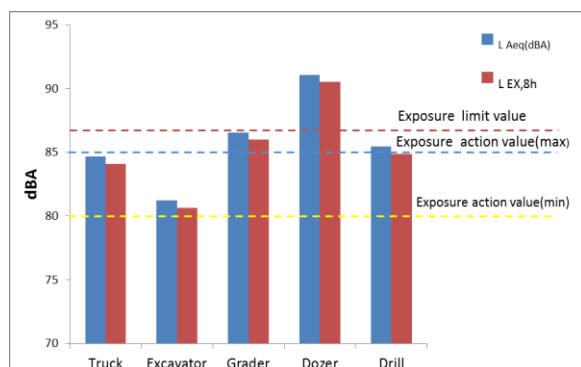
Figure 2.1. Noise levels of different machines during production.

3. Artificial Neural Network

Artificial Neural Network (ANN) is a kind of intelligent computing system that simulates biological neural network. It has features such as self-learning, self-organizing, non-linear dynamic process and high fault tolerance a large number of inputs and outputs are required for the ANN to train and reach the target outputs. These data sets are called "training" and "test". After the learning process, "test" is performed to see how the designed network is using the "test" data. In the learning process, the system, which regulates the weights of ANN in the network to produce the desired outputs, is called the learning algorithm. The training process continues until the targeted output value is achieved. The error

resulting from the difference between the desired output and the resulting output value in the network is minimized by changing weights.

There are many ANN architectures in the literature. In this study, a backward-spread forward-feed multi-layer learning mechanism suitable for engineering applications was used for prediction. In the ANN model, the noise measurements test data of heavy machinery operators in surface coal mining were usedMATLAB program was used in the design and training of ANN model for estimation of risk levels of noise exposures in mining enterprises. Not all data are used in the education of ANN models, preferably 70 to 90% of the data allocated for training and 30 to 10% of the test data. In this study, 48 of the 60 data obtained from the measurement results were randomly used for training and 12 of them were used for testing and verification process, and our database was divided into 80% training and 20% test data. Training and test data were determined for the analysis of the random network to represent each set of inputs. Within the scope of the study, vehicle type, measurement times, ambient temperature, pressure and relative humidity were determined as input parameters for the applied neural network, equivalent noise level and maximum value of instantaneous noise pressure were determined as output parameters. Different normalization techniques have been tried for these parameters and it has been found that using the equation (3.1), normalizing technique between 0.1 and 0.9 gives more realistic results.

$$x_N = 0,8 \left(\frac{x_i - x_{min}}{x_{max} - x_{min}} \right) + 0,1 \qquad \textbf{(3.1)}$$

In this equation parameters refers to;

x_N : The normalized data
x_i : The actual value in a parameter
x_{min} : The minimum value in a parameter
x_{max} : The maximum value in a parameter

The data used for testing for the stable structure of ANN's were not used during the training phase of the network.

4. Results and Discussion
4.1. The noise level to which operators using construction machinery are exposed

In this study, it is aimed to determine the noise level exposed to the operators using the construction machinery in the open mine operations and daily personal noise measurements from 60 different construction operators are carried out in accordance with the standards. Noise may be generated during operations such as loading-unloading, digging

drilling while many mining machines are operating at the same time. This affects all operators operating at the same time. According to the noise measurement results in different units of the enterprise, there are some workplaces with noise levels between 74.5-98 dB. Approximately 85% of the noise measurements were 80 dBA and 27% were higher than 87 dBA. Between the all machines, crawler dozer operators are exposed to noise above the exposure action value. In the study, the average equivalent noise level (L_{Aeq}) was calculated as 91.08 dBA. The equivalent noise level of 8 hours (L_{EX-8h}) is 90.8 dBA. Tracked dozers are the highest noise level vehicles among the sampled work machines and the measurement results are very close to the exposure limit value of 87 dBA. The noise level of earthmoving truck, hydraulic excavator, grader and hydraulic hammer-drills is equal to or higher than the limit of 80.0 dBA, which is the limit of precaution.

4.2. Artificial Neural Networks Results

In this study, it is aimed to obtain a reliable noise risk level estimation with ANN in open pit mine operation conditions. Nowadays, ANN is more economical and faster than experimental studies and can be used successfully in many engineering applications. An artificial neural network model was developed to predict noise measurements of heavy machinery operators. The input data for ANN are normalized to be between 0.1 and 0.9 . Many different models established on MATLAB have been tried and the most successful model has reached 5000 acceptable iterations and the network has been completed. The average error rate of the training phase was found to be 1.74% for the equivalent noise level and 1.24% for the maximum value of the instantaneous noise pressure.
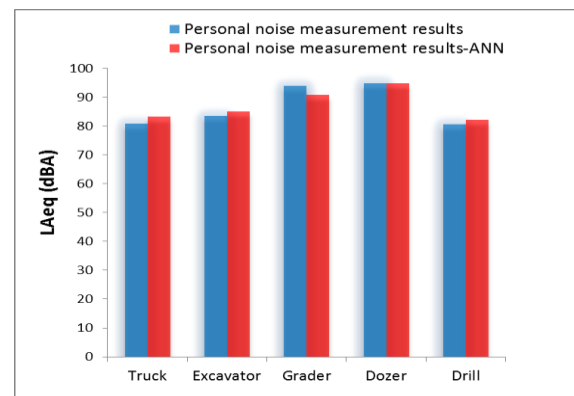
Figure 4.1. Comparison of equivalent noise level measurement results and ANN results for all mining machines during the training phase.
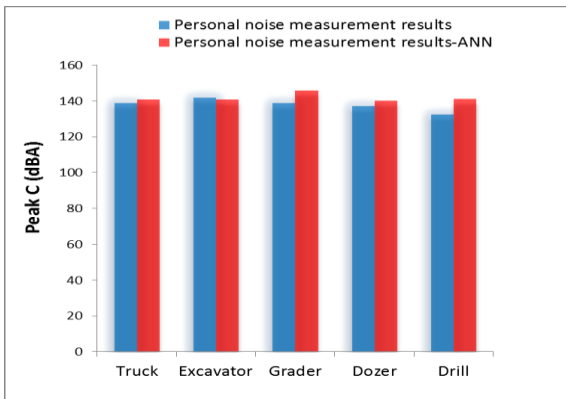
Figure 4.2. Comparison of the maximum value of the instantaneous noise pressure and the ANN results in the training phase for all mining machines.

When the graphs given in Figures 4.1 and 4.2 are taken into consideration, it is clear that the experimental results and the values obtained from ANN are very close.
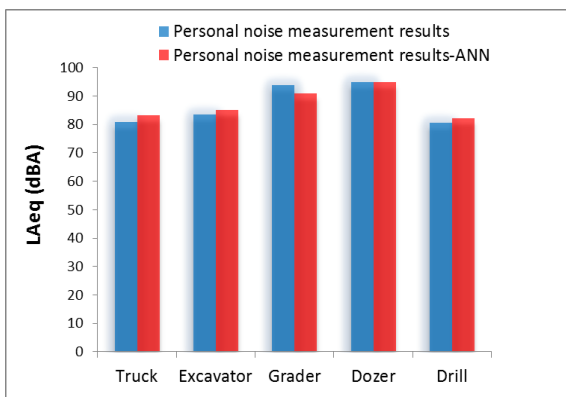
Figure 4.3. Comparison of the equivalent noise level measurement results and the ANN results in the test phase for all mining machines.
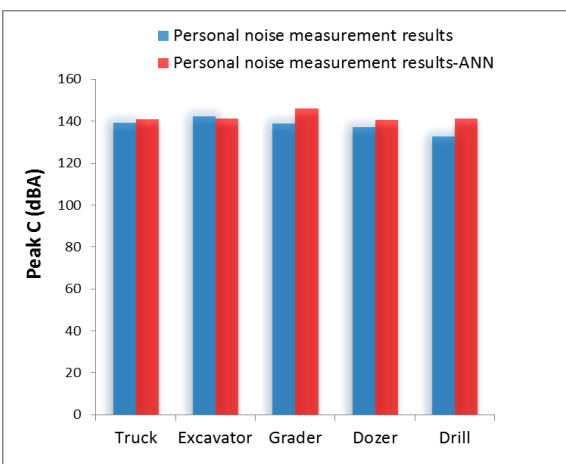
Figure 4.4. Comparison of the maximum value of the instantaneous noise pressure and the ANN results in the test phase for all mining machines.

After reaching the required error limit in ANN training, the test procedure of ANN was started. In order to test the performance of the network, 12 values that were not used in the training set were presented to the network and the results were compared with the experimental results. The relationship between actual test data and calculated values using ANN method is shown in Figure 4.3-4.4.

When the results obtained from the test set were compared with the experimental results, it was found that the network found sufficient accuracy and the error rate in the test phase was 2.82% for the equivalent noise level and 2.66% for the maximum value of the instantaneous noise pressure. In Figure 4.5, Scatter diagrams are drawn between equivalent noise measurement values and calculated values using ANN method. The correlation coefficient was found to be 0.9914 (Figure 4.5-a) for the equivalent noise level (L_{Aeq}) in drilling machines and the maximum value of instant noise pressure in the grader (Peak) was 0.9924 (Figure 4.5-b). The results of the study show that ANN method can be used very successfully in estimating equivalent noise measurement values.
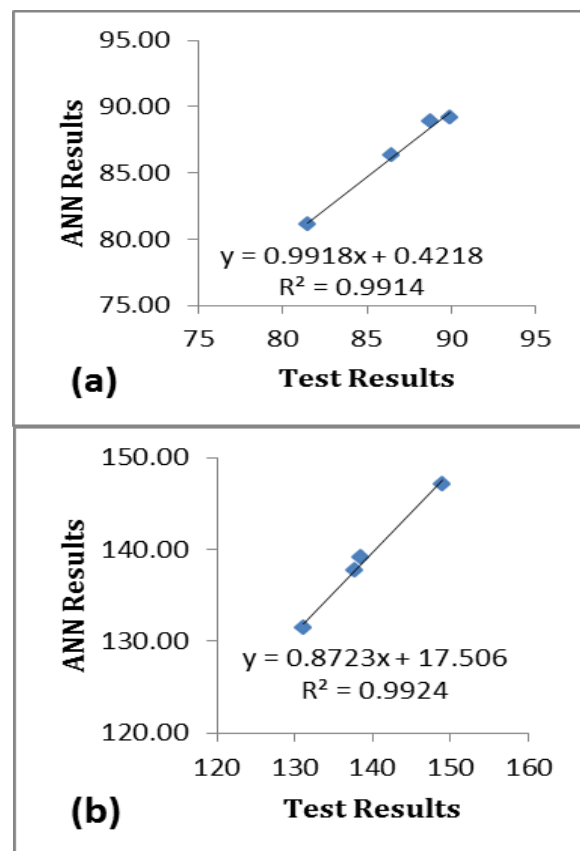
Figure 4.5. Scatter diagrams of equivalent noise measurement values (R^2: coefficient of determination).

5. Results

Preventive engineering measures should be taken in the workplaces in order to reduce the noise exposure of operators using heavy machinery and to minimize the risks that may occur as a result of these exposures. Assessing the noise levels of mining sites will help to control the risk of noise-related hearing loss among workers. Measures that can be taken to reduce the exposure are as follows;

- Many parts of the machine will loosen over time due to uneven and rough roads. If these loosening parts are not installed properly, it will cause noise and operators will be adversely affected. Periodic maintenance of machinery and special parts and regular lubrication of moving parts will reduce noise levels.

- Every personnel who will work in places with a noise level of 80 dB (A) and more, before starting work; training should be given, emphasizing the benefits and importance of personal protective equipment, including possible effects of noise on hearing, the purpose of ear protectors and their proper and regular usage, identification of the appropriate type of protection and their maintenance and cleaning. Posters regarding noise hazards and the importance of using personal protective equipment should be posted where workers can see them. Also, employers should provide employees with healthy and appropriate conditions of working. On the other hand, the workers should all the time to consider the effects of noise and consequential damages, and use personal protective equipment.

- It is necessary to keep the doors and windows of the machine closed to prevent noise in the cabin. Noise formation can be controlled by using insulation material in the cabin.

In addition, ANN-based mathematical model developed to estimate the data obtained from noise measurements of heavy machinery operators in opencast mine. The values obtained after training and testing of ANN were examined and the following basic results were obtained:

- The results of the study showed that the results obtained during the ANN training and the testing phase give close values to the actual results and show that it is possible to estimate the noise measurements of the machine operators in a healthy way.

- Designed with five inputs and two outputs, the network structure provides high accuracy estimates.

- Due to the low error rate of the training phase, the value selected for the test phase in the ANN was very close to the actual test result.

- In the estimation of the equivalent noise level and the maximum value of the instantaneous noise pressure in the construction machinery operators, it has been concluded that the mathematical model can be formed with ANN.

- With this study, it is seen that the risk level can be estimated in mining enterprises by ANN without the need for classical methods that cause time and cost loss.

Author Contributions

Ayla Tekin: wrote the manuscript.

Ethics

There are no ethical issues after the publication of this manuscript.

References

1. Utley, W. A. 1980. Noise from opencast coal mining sites. *Applied Acoustics*; vol. 13, no. 2, pp. 85–102.

2. Ghose, M.K. 1990. Noise pollution evaluation and its abatement measures in coal mining area. *Minetech*; vol. 11, no. 3, pp. 55–57.

3. Vardhan, H., Rao, Y. and Karmakar, N. 2004. Noise analysis of heavy earth moving machinery deployed in opencast mines and development of suitable maintenance guidelines for its attenuation - part 1. *Noise and Vibration Worldwide*; vol. 35, no. 8, pp. 11–24.

4. Sharma, O., Mohanan, V. and Singh, M. 1998. Noise emission levels in coal industry. *Applied Acoustics, Elsevier*; vol. 54, no. 1, pp. 1–7.

5. Barrientos, M.C., Lendrum, D.C. and Steenland, K. 2004. Occupational Noise; Assessing the Burden of Disease from Work-Related Hearing Impairment at National and Local Levels. *World Health Organization Protection of the Human Environment. Environmental Burden of Disease Series;* No. 9. Geneva.

6. Donoghue AM. 2004. Occupational health hazards in mining: an overview. *Occupational Medicine*; 54: 283 - 289.

7. Ramlu, M.A. 2005. Occupational noise exposure and hearing damage. *Mining Engineer's Journal*; vol. 6, no. 7, pp. 9–20.

8. Onder, S., Onder, M. 2018. Statistical investigation of the noise levels in coal mining industry. *J. of Eng. & Arc. Fac. of Eskisehir Osmangazi Un.*; 26 (1), 30-35.

9. Daniel, E. 2007. Noise and hearing loss: A review, *Journal of School Health;* **77**, 5, 225-231.

10. Joy, G. J., Middendorf, P. J. 2007. Noise exposure and hearing conservation in us coal mines-a surveillance report. *Journal of Occupational and Environmental Hygiene*; vol. 4, no. 1, pp. 26–35,

11. Dekker JJ, Edwards AL, Franz RM, *et al*. 2011. Meeting the milestones: are South African small- to medium-scale mines up to the task. *The Journal of The Southern African Institute of Mining and Metallurgy*; 111: 309-313.

12. Edwards, A.L., Dekker, J.J., Franz, R.M., Dyk, T. V. and Banyini, A. 2011. Profiles of noise exposure levels in South African Mining. *The Journal of The Southern African Institute of Mining and Metallurgy*; vol. 111, pp. 315–322.

13. Çınar, İ., Şensöğüt, C. 2013. Evaluation of noise measurements performed in mining sites for environmental aspects. *International Journal of Environmental Research*; 7(2), 383-386.

14. Álvarez-Vigil, A.E., Gonzalez-Nicieza, C., Gayarre, F.L., Álvarez-Fernández, M.I. 2012. Predicting blasting propagation velocity and vibration frequency using artificial neural networks. *International Journal of Rock Mechanics and Mining Sciences*; 55, 108-116.

15. Görgülü, K., Arpaz, E. Demirci, A., Koçaslan, A., Dilmaç, M.K., Yüksek, A.G. 2013. Investigation of blast-induced ground vibrations in the Tülü boron open pit mine. *Bulletin of Engineering Geology and the Environment*; 72, 555-564.

16. Simangunsong, G.M., Wahyudi, S. 2015. Effect of bedding plane on prediction blast-induced ground vibration in open pit coal mines. *International Journal of Rock Mechanics and Mining Sciences*, 79, 1-8.

17. Nanda SK, Tripathy DP. 2011. Application of functional link artificial neural network for prediction of machinery noise in opencast mines. *Advances in Fuzzy Systems*, 4, 1-11.

18. Huang X. 2012. Study on ANN noise adaptability in application of industry process characteristics mining. *Advanced Materials Research*; 462:635-640.

19. Karacan, C.Ö. 2008. Modeling and prediction of ventilation methane emissions of US longwall mines using supervised artificial neural networks. *International Journal of Coal Geology*; 73, 371-387.

20. Zhao, K., Chen, S. 2011. Study on artificial neural network method for ground subsidence prediction of metal mine. *Procedia Earth and Planetary Science*; 2, 177-182.

21. Naghadehi, M.Z., Jimenez, R., KhaloKakaie, R., Jalali, S.M.E. 2013. A new open-pit mine slope instability index defined using the improved rock engineering systems approach. *International Journal of Rock Mechanics and Mining Sciences*; 61, 1-14.

22. Siami-Irdemoosa, E., Dindarloo, S.R. 2015. Prediction of fuel consumption of mining dump trucks: A neural networks approach. *Applied Energy*; 151, 77-84.

23. Rahimdel MJ., Mirzaei M., Sattarvand J., Ghodrati B., Mirzaei Nasirabad H. 2017. Artificial neural network to predict the health risk caused by whole body vibration of mining trucks. *Journal of Theor Appl Vibr Acous*; 3(1), 1–14.

24. Nguyen H, Bui X-N, Bui H-B, Mai N-L. 2020. A comparative study of artificial neural networks in predicting blast-induced air-blast overpressure at Deo Nai open-pit coal mine, Vietnam. *Neural Comput Appl*; 32:3939–3955.

25. Nguyen, H., Bui, X.-N., Tran, Q.-H., Le, T.-Q., Do, N.-H., & Hoa, L. T. T. 2019. Evaluating and predicting blast-induced ground vibration in open-cast mine using ANN: a case study in Vietnam. *SN Applied Sciences*; 1(1), 125.

Celal Bayar University Journal of Science

Investigation of the cold forging operation steps' effect on forming properties

Alper Baygut[1]* , Osman Çulha[2]

[1] BOLT R&D (BOLT Fasteners), Bursa, Turkey
[2] Manisa Celal Bayar University, Faculty of Engineering, Material and Metallurgical Engineering.,
Manisa, Turkey
*alper.baygut@bolt.com.tr
*Orcid No: 0000-0003-4775-1066

Abstract

Cold forming is a manufacturing process that plastically deforms metal using dies. It allows for high speed production, little to no material waste compared to conventional machining, and creates a stronger end product due to work hardening of the material. Cold working in forging process refers to the process of strengthening steel alloy by changing its shape without the use of heat. Subjecting the alloy to this mechanical stress causes a permanent change to the metal's crystalline structure, causing an increase in strength. At this time applied deformation rate, velocity and die design of product effect the mechanical features, flow-orientation properties of sample and load requirements for forging process of rivets. In this study, it is aimed to investigate the operation steps effect on formability characteristics of rivet produced by cold forming with the support of finite element method. Effective plastic strain, yield stress and forging force variations depending on die design were obtained by simufact.forming simulation software. Simulations made with different die designs and physical production results of these dies were compared. The effects of the number of forming operations and die cavity on the process were determined by performing material flow, hardness and structural analysis.

1. Introduction

A method of forming a solid body into a different shape without changing the mass and volume of it is called plastic forming method. Ferrous materials such as carbon and alloy steels (including stainless and heat resistant steels), aluminum, zinc, copper and their alloys can be processed by plastic forming methods. The most important application areas of the parts produced by these methods can be listed as follows: i) Numerous parts produced for various industries such as automotive, machine tools (car body, crankshafts), ii) Hand tools such as pliers, hammers, screwdrivers and medical tools, iii) Fasteners such as screws, nuts, bolts, rivets and iv) Fasteners used in construction industry, eg using at doors and windows [1].

It is important to know the plastic deformation ability of material, the pressure, strength and power levels required for the process so that the solid metal can be shaped without breakage and separation. For the success of the method, selection of material properties, die design and process parameters are very important [2].

"Cold forging" or "cold forming" is a plastic forming method which is shaped by pressing the workpiece into a die set. The cold forging uses the plastic properties of the metal to shape the metal at room temperature. The production of a part by cold forming instead of machining provides advantages such as material gain, increased mechanical properties due to cold forming, controlled material flow [3].

While designing this process, it is the design advantages gained by using simulation and artificial neural networks model by analyzing multistep cold forming processes based on predetermined process status parameters and tool geometry [4,5]. Finite element methods (FEM) provided a new perspective on metal forming applications in the 1970s and early 1980s. One of these methods, the computer program Battelle Columbus Laboratories, was developed in the US [6]. The first study that led to this development was supported by the US Air Force and was derived from pioneering studies of rigid-plastic FEM conducted by Kobayashi et al [7]. Kim Hyunkee and Taylan Altan in

their study in 1996, contains information about the cold forged parts in the literature and about the forging industry [5]. K.Wagner, A.Putz and U.Engel in their study in 2006, finite element analysis method was used to determine the regions where the deformations of the dies were most concentrated. In order to increase the die life, three different die surface treatment methods were evaluated [8]. In 1992, M.Geiger, M. Hansel and T.Rebhan, the finite element method was used to determine the fatigue resistance of an extrusion die used in the cold forging process [9]. In addition to die analysis with simulation programs, Conor MacCormack and John Monaghan, in 2002, the accuracy of the design of the products can be simulated in 2D and 3D [10]. During the development of metal forming methods and the parameters to be examined during production, the production methods are compared and the processes that have been studied up to date have been evaluated [11]. Analytical results herein demonstrate that the stress and strain inside the rivet can be elucidated using metal forming software. Together with experimental results, they demonstrate that a concentration of stress, strain, flow, yield stress variate the parameter in the forming process. Planning for proper die design and production, increasing the quality of products, and reducing the number of defective products promote industrial competitiveness. Applying the FEM to analyze metal processing presents the advantages of (1) being able to acquire detailed data (e.g. velocity field, geometric shape, effective strain, effective stress, temperature change or contact pressure, and displacement distribution) after object deformation and (2) requiring little programming content and input data when analyzing several relevant problems in rapid solution environments. The % cold forming amount and the number of cold forging operations affect the mechanical properties and forming capability of the material.Forming processes were analyzed considering two different die designs and number of operations by FEM [11-17].

However, with increasing global competition, conventional cold forging processes are facing challenges. This is due largely to the demand from customers who require components with high-precision and a stable quality, using high strength-to-weight ratio materials. On the other hand, industry also needs to reduce cost and improve efficiency against other competitors. As one of the efforts to meet these requirements, cold forging is being researched as a new option from which rivet components can be obtained in a minimum number of forging steps. In this paper, the finite element method was used to analyze the influence of die shapes with different operation number and machine on the extrusion forging deformation. Experiments using two sets of dies with different shapes were performed, and the results were compared with the predictions of the finite element method for the same deformation mode. Thus, the results of the deformation

analysis in this study were extended to the design of decreasing operation number or step and in the planning of a forming process. This would be beneficial for the forging industry [15-22].

2. Materials and Methods

The raw material selection of the product is made using EN 10263-4, which is the raw material standard which contains plastic formable, malleable and heat-treated steel. The standard and actual chemical composition of the 20MnB4 raw material to be used is given in Table 1.

Table 1. Comparison of raw material chemical composition according to EN 10263-4.

Elements	Standard variation ranges	Chemical Analysis
C	018-0,23	0,20
Si (max)	0,30	0,09
Mn	0,90-1,20	0,97
P (max)	0,025	0,006
S (max)	0,025	0,008
Cr (max)	0,30	0,2
Cu (max)	0,25	0,04
B (max)	0,0008- 0,005	0,0035

2.1. Die Design Study

Two different processes were designed to examine the effect of the number of deformation steps on cold forming properties. In the first design, which has been designed by considering the cold forging capability and the transitions between the operations, special rivet products are designed as three stations such as; extrusion, forming and heading, in multi-station machines. The product dimensions foreseen by the design are as in Figure 1.
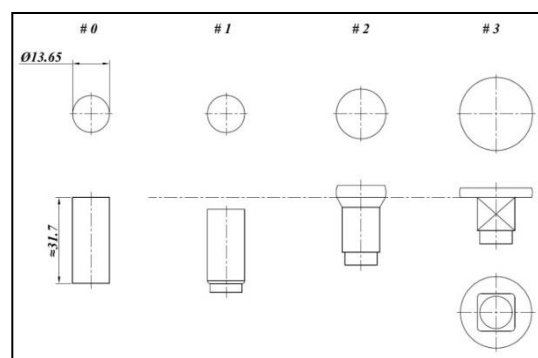
Figure 1. First design: 3 operation.

The existing design, illustrated in Fig.1, was revised. In this revision, it is planned to remove the head preparation performed in the second operation step. As a result of the decrease in the number of stations, the multi-station press machine, where the production of special rivets was made, was replaced and the two die

four blow rivet machine was used. In this way, it is aimed to increase the production cycle of the product. The operation card formed after the revised design is as shown in Figure 2.
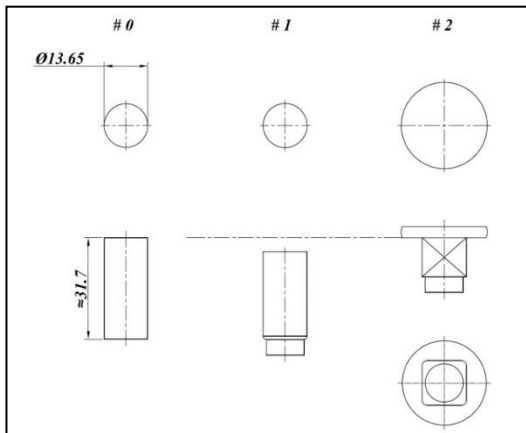
Figure 2. Two operation product design.

2.2. Simulation Study

Numerical simulation using the upper-bound or finite element method is often used in the approach to such research. The different properties and geometry of work piece, the condition and the factor of friction, and the geometry profile of the die were the main objectives of analysis. The deformation behaviour, the flow modes, the deformation load and the filling of the die cavity of the deformed shape were the features of interest in this study. 3D solid models of the dies used in three and two station systems were prepared for simulation solution. Machine parameters, material data, friction model and ambient temperatures defined in the simulation program. Additionally, two different machine features for the production of the part are shown in Figure 3.
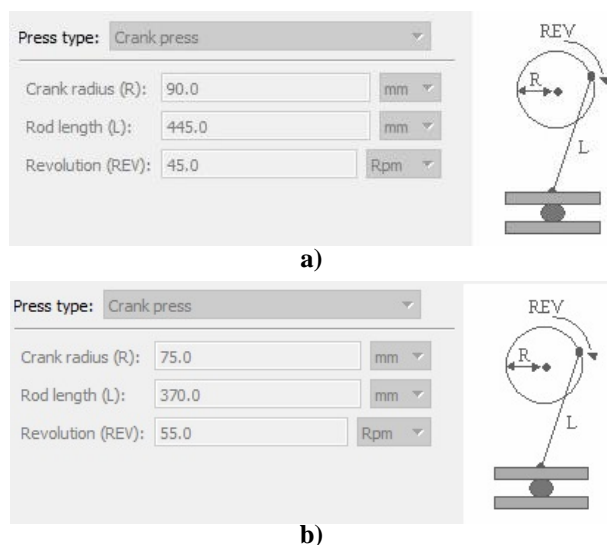
Figure 3. a. Multi station cold forming machine parameters for three station production design and b. Two die four blow cold forming machine parameters.

Due to the lack of raw material data of 20MnB4 in the simulation program, 19MnB4 material which is equivalent to this material has been selected. The material data of 19MnB4 is shown in Figure 4.
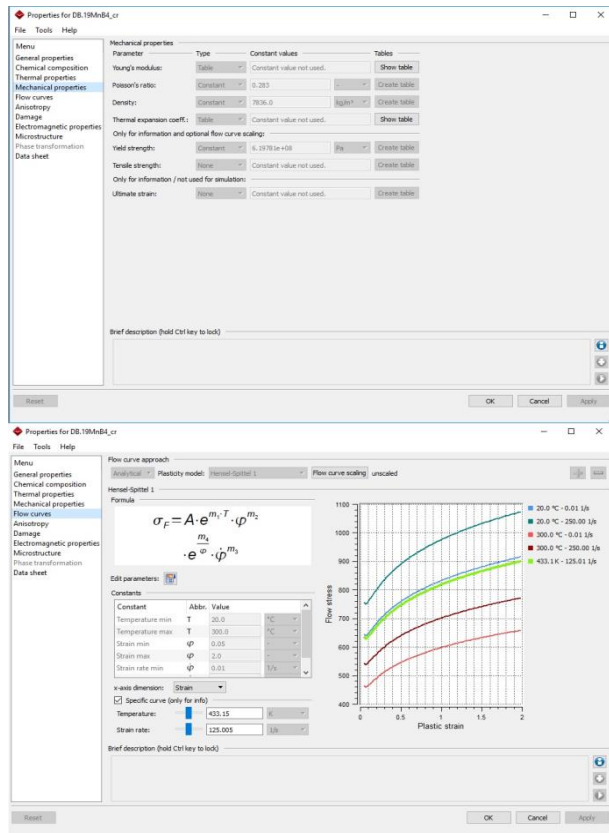
Figure 4. 19MnB4 material data.

The key item of every forming process is the workpiece. Its inherent properties (mechanical, thermal) are defined by the associated material data. Especially the mechanical material properties can be quite complex and are a source of nonlinearity which results in significant computational efforts. As seen in figure 4, in pre-processing stage of analysis analytical flow curve approach with Hensel-spittel plasticity model was used in numerical solution of two and three station production design. The Coulomb model, which is most suitable for the cold forging process, has been chosen as the friction model. The temperature values at which the cold forging process was carried out were taken at ambient temperature 20 ºC. At the end of the pre-processing of design; application module and process type, positions and geometries, desired material, press (machine), friction properties, heat properties and workpiece mesh were chosen.

3. Results and Discussion
3.1. Simulation Results

In both cases, plastic deformation, stress, yield stress, force values obtained as a result of simulation are as shown in the figures below. The value of effective

A. Baygut

plastic strain is the integral of stepwise increments of plastic deformation for a period of analysis time t. According to the numerical solution of two ad three station analysis, effective plastic strain distribution is illustrated in Fig. 5 and 6. Effective plastic strain and stress occurs near cold extrusion and reduction of area in die.
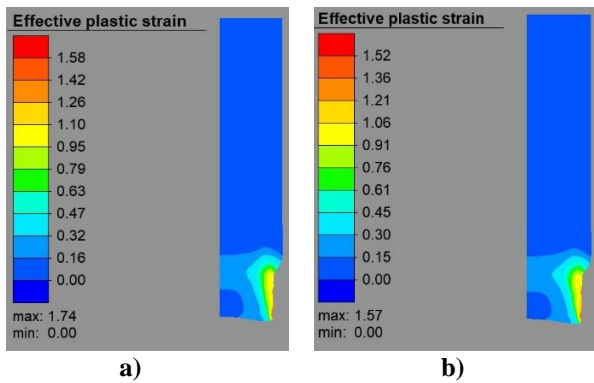
Figure 5. a. and b. Effective plastic strain distributions of the first operating step of the three-station design and the two-station design, respectively.
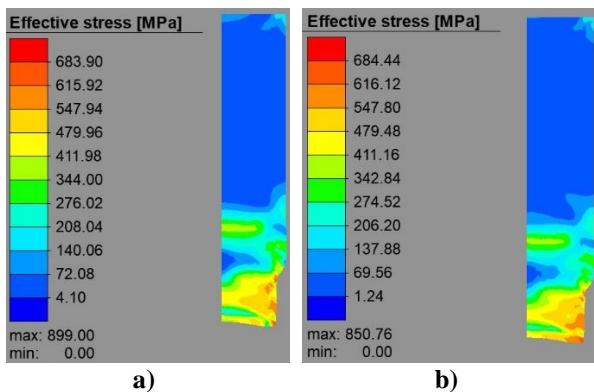
Figure 6. a. and b. Effective stress distributions of the first operating step of the three-station design and the two-station design, respectively.

The change in yield strength depending on the deformation rate is shown in Figure 7. The yield strength of the material increased from 638.99 to near 890 MPa, where deformation occurred.

The change in effective plastic strain and yield strength in the final operations of two and three station die designs is shown in Figure 8 and 9. Cold working generally results in a higher yield strength as a result of the increased number of dislocations and the Hall–Petch effect of the sub-grains, and a decrease in ductility, as microstructural explanation. Fig. 5 and Fig. 6 shows cold work effect on work piece.
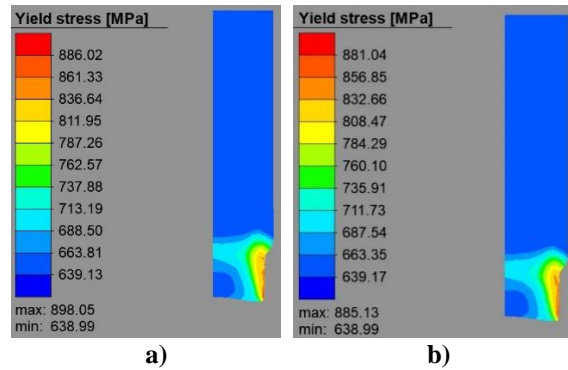
Figure 7. a. and b. Yield stress variations depending on plastic deformation of sample in first operating step of the three-station design and the two-station design, respectively.

As stated at the beginning of the study, the second operation of the three-station design has been removed. Therefore, the excessive yield strength and hardness increase or material flow-orientation that may occur in the material have been investigated. Since the total deformation did not change, a very high change in yield strength was not observed. In this context, the biggest difference detected was revealed in the deformation load as illustrated Table 2.
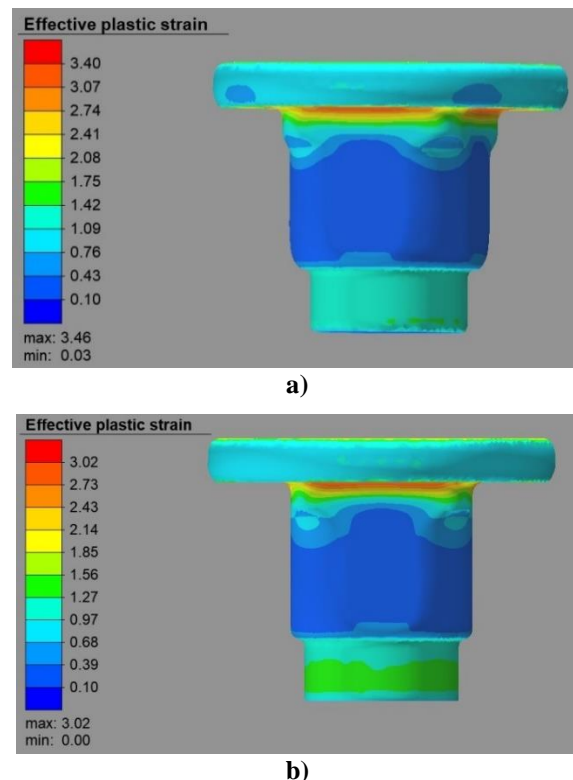
Figure 8. a. and b. Effective plastic strain distributions of the last operating step of the three-station design and the two-station design, respectively.

a)

b)
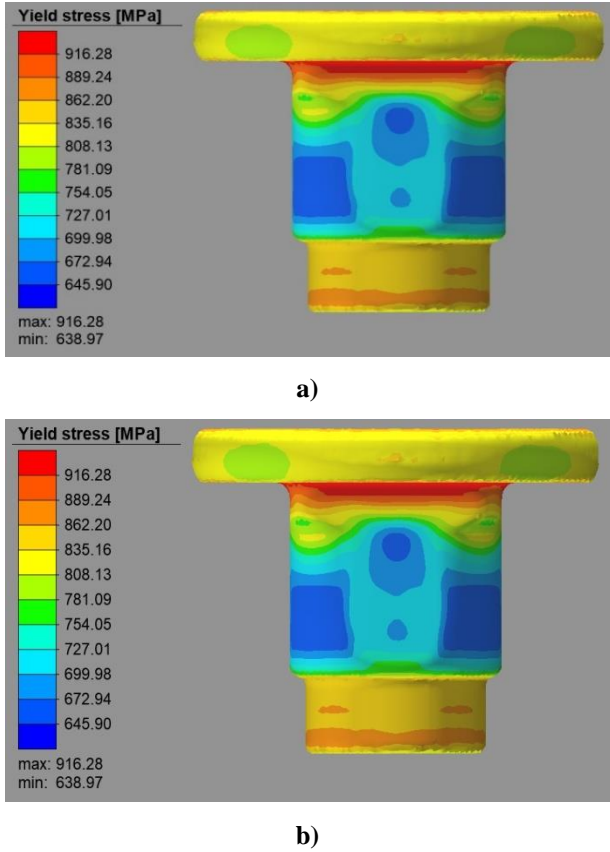
Figure 9. a. and b. Yield stress variations depending on plastic deformation of sample in last operating step of the three-station design and two-station design, respectively.

Table 2. Total deformation load of the three-station design and two-station design.

	Three operation design force (ton)	Two operation design force (ton)
First Operation	10.19	10.24
Second Operation	13.72	-
Last Operation	65.9	63.74
Total	89.81	73.98

a)
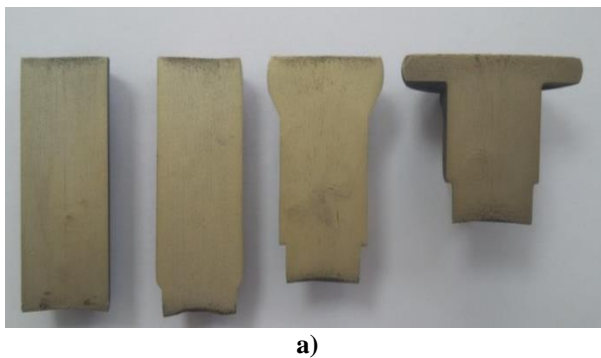
3.2. Physical Production Results of Different Design

After numerical analysis of the three-station and two-station design of sample were finished, physical rivets were produced as in Figure 10. It has been determined that absence of the second operation step in three operation step design does not affect the final product in dimensions.

a)

b)

Figure 10. Prototype production of a) three-station and b) two-station design of sample.

3.3. Macro Etching Examination

In order to reveal plastic deformation grain structure in the material, macro etching process was applied to the produced rivets. This procedure was applied to each operation sample of the part produced in three operation steps and the part produced in two operation steps. Macro etching results are shown in Figure 11. When the material flow lines are examined, no discontinuity is observed. Material flow was stable and regular. As a result of the removal of the second operation, no negativity was observed in the rivet section, which is the final product, due to the high shaping and plastic behaviour of the raw material.

b)
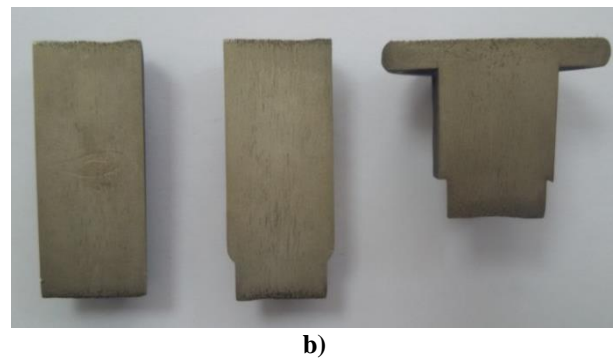
Figure 11. Flow lines of rivets: a) three-station and b) two station design.

3.4. Metallographic Review

Metallographic analysis was performed to examine the microstructural properties of the material. By focusing on the critical cross-sectional change regions of the special rivet, high surface area images have been obtained. The microstructure of the same samples produced by three and two stations design are illustrated in Figure 12.a and b, respectively. The microstructures are oriented without breaking, in the direction of the forging. As a result of plastic forming microstructures of two and three station samples show similar characteristics.

a)

b)
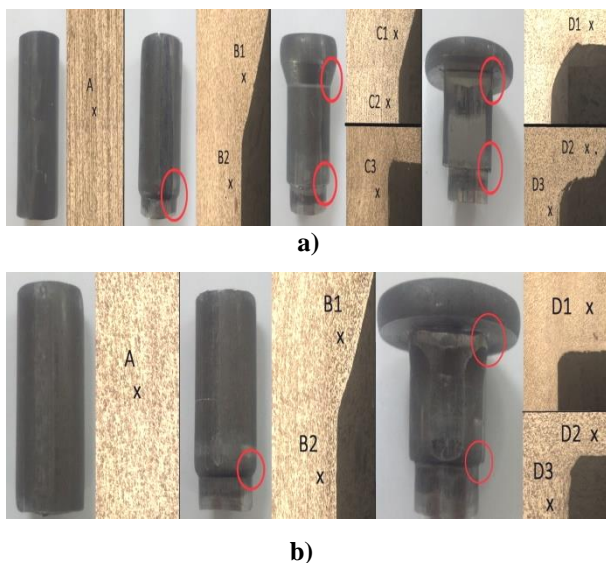
Figure 12. The microstructure (100X) of the same samples produced by a) three and b) two stations forging design**.**

3.5. Micro Hardness Review

Hardness measurements were taken from regions where the cross-section changes during plastic deformation. The hardness changes taken from the places expressed in the microstructure images; figure 12 and b., are shown in Table 3.

Table 3. Hardness measurement of rivets.

Measurement Point	Hardness of three operation design (HV1)	Hardness of two operation design (HV1)
A	196 ±2	202 ± 2
B1	197 ± 1	207 ± 3
B2	200 ± 1	222 ± 2
C1	261 ± 2	-
C2	193 ± 2	-
C3	202 ± 2	-
D1	288 ± 1	282 ± 2
D2	217 ± 2	208 ± 1
D3	216 ± 3	214 ± 2

Table 3 shows the hardness measurements taken from peer stations. Despite the decrease in the number of stations, the hardness in the same area is at the same level. As known, Hardness as a measure of material's resistance to permanent deformation, and thus to wear, is an important quality parameter for the finished product. It is also a measure of forgeability of a material undergoing a cold forming process. Generally, cold formed parts are forged in a number of stages and in each stage the material undergoes additional permanent deformation. The material, during the processing, sometimes becomes so hard that further forming becomes impossible without fracturing the part. When the steel quality used in this study is examined, the amount of hardening by deformation is lower than other grades. However, the change in hardness is noticeable in areas where deformation occurs intensely and material flow is accelerated.

4. Conclusion

Special form rivets were produced in a multi-stage cold forging machine in three operation steps. In the part design, the head preparation process in the second operation was removed and the design was revised. In the new design production, the number of pieces produced per minute increased by approximately 20 %. 13.72 tons needed in the second operation in the three-operation design was eliminated. This resulted in an increase in energy efficiency.

It was investigated whether the decreasing in the operation step caused differences in the microstructure on the part. In this context, microstructure tests, macro etching process and surface hardness screening were performed.

In the microstructure and macro etching test, grain structure of the parts belonging to both designs were examined. As a result of the examination, it was determined that the grain structures were similar.

In the hardness screening test, measurements were made on the same points of the same operation step. As shown in Table 3, the elimination of the head preparation operation was evaluated to be the difference less than 10% in the hardness of the piece.

Acknowledgement

Author Contributions

Alper Baygut: Drafted and wrote the manuscript, performed the experiment and result analysis.

Osman Çulha: Drafted and wrote the manuscript.

Ethics

There are no ethical issues after the publication of this manuscript.

References

1. Çapan,L. 1996. Plastik Şekil Verme. TMMOB Makine Mühendisliği El Kitabı; 2, 170: 32-61.

2. Aran A., Demirkol M. İTÜ Makine Mühendisliği İmal Usulleri Ders Notları, İstanbul, 1995.

3. Çapan,L. 1988, Dövme Teknolojisi. 2, Seç Kitap , İstanbul, 1988; 69-114.

4. Hsu Q-C., Lee R-S. 1997, Cold forging process design based on the induction of analytical knowledge. Journal of Materials Processing Technology; 69: 1–3: 264-272.

5. Kim H., Altan T. 1996. Cold forging of steel -practical examples of computerized part and process design. Journal of Materials Processing Technology; 59: 1-2: 15: 122-131.

6. Knoerr M., Lee J., Altan T. 1992. Application of the 2D finite element method to simulation of various forming processes. Journal of Materials Processing Technology; 33: 31–55.

7. Kobayashi S., Oh S., Altan T. 1989. Metal Forming and the Finite Element Method. Journal of Materials Shaping Technology; 8: 65 – 66.

8. Wagner K., Putz A. and Engel U. 2006. Improvement of Tool Life in Cold Forging by Locally Optimized Surfaces. Journal of Materials Processing Technology; 177: 1-3: 206-209.

9. Geiger M., Hansel M., Rebhan T. 1992. Improving the fatigue resistance of cold forging tools by FE simulation and computer aided die shape optimization. Proceedings of the Institution of Mechanical Engineers Part B Journal of Engineering Manufacture; 206: 143-150.

10. MacCormack C., Monaghan J. 2002. 2D and 3D finite element analysis of three stage forging sequence. Journal of Materials Processing Technology; 127: 48-56.

11. Groche P., Fritsche D., Tekkaya E.A., Allwood J.M., Hirt G., Neugebauer R. 2007. Incremental Bulk Metal Forming. CIRP Annals - Manufacturing Technology; 56: 2: 635-656.

12. Yavuzbarut T. 2018. 8.8 Kalite sinifındaki bağlanti elemanlarinin mikro alaşimli çelikler kullanilarak işil işlemsiz üretilmesi. İzmir Katip Çelebi Üniversitesi Fen Bilimleri Enstitüsü; 22-24.

13. Altan T., Ngaile G., Shen G. Cold and Hot Forging Fundamentals and Applicatons. ASM International. Unıted States of America, 2005, pp 67-81

14. J.M. Monaghan, Stress analysis of a cold forging process applied to a countersunk headed fastener, Journal of Materials Processing Technology, 39 (1993) 191-211.

15. Senyong Chen , Yi Qin , J.G. Chen , Chee-Mun Choy, A forging method for reducing process steps in the forming of automotive fasteners, International Journal of Mechanical Sciences, 10.1016/j.ijmecsci.2017.12.045.

16. D. Petrescu, et al., Simulation of the fastener manufacturing process, Journal of Materials Processing Technology, 125-126, 2002, 361-368.

17. Z. Li, D. Wub, Study of the high strength and low yield ratio cold forging steel, Materials Science and Engineering A 452–453 (2007) 142–148.

18. P. Hartley, I. Pillinger, Numerical simulation of the forging process, Comput. Methods Appl. Mech. Engrg. 195 (2006) 6676–6690.

19. A. Gontarz, Z. Pater, W. Weroñski, Head forging aspects of new forming process of screw spike, Journal of Materials Processing Technology 153–154 (2004) 736–740.

20. Chun-Yin Wu, Yuan-Chuan Hsu, The influence of die shape on the flow deformation of extrusion forging, Journal of Materials Processing Technology 124 (2002) 67–76.

21. L. Brayden and J. Monaghan, An analysis of closed-die extrusion/forging, Journal of Materials Processing Technology, 26 (1991) 141-157.

22. Z. Gronostajski, et al., Recent development trends in metal forming, archives of civil and mechanical engineering 19 (2019) 898 – 941.